MNRAS **451,** 539–580 (2015) doi:10.1093/mnras/stv961

The power spectrum and bispectrum of SDSS DR11 BOSS galaxies – I. Bias and gravity

Héctor Gil-Marín,[1⋆] Jorge Noreña,[2,3⋆] Licia Verde,[4,2,5⋆] Will J. Percival,[1] Christian Wagner,[6] Marc Manera[7] and Donald P. Schneider[8,9]

[1]*Institute of Cosmology & Gravitation, University of Portsmouth, Dennis Sciama Building, Portsmouth PO1 3FX, UK*
[2]*Institut de Ciències del Cosmos, Universitat de Barcelona, IEEC-UB, Martí i Franquès 1, E-08028 Barcelona, Spain*
[3]*Department of Theoretical Physics and Center for Astroparticle Physics (CAP), 24 quai E. Ansermet, CH-1211 Geneva 4, Switzerland*
[4]*ICREA (Institució Catalana de Recerca i Estudis Avançats), Passeig Lluís Companys, 23 E-08010 Barcelona, Spain*
[5]*Institute of Theoretical Astrophysics, University of Oslo, Oslo 0316, Norway*
[6]*Max-Planck-Institut für Astrophysik, Karl-Schwarzschild Str. 1, D-85741 Garching, Germany*
[7]*University College London, Gower Street, London WC1E 6BT, UK*
[8]*Department of Astronomy and Astrophysics, The Pennsylvania State University, University Park, PA 16802, USA*
[9]*Institute for Gravitation and the Cosmos, The Pennsylvania State University, University Park, PA 16802, USA*

Accepted 2015 April 29. Received 2015 April 14; in original form 2014 July 21

ABSTRACT

We analyse the anisotropic clustering of the Baryon Oscillation Spectroscopic Survey CMASS Data Release 11 sample, which consists of 690 827 galaxies in the redshift range $0.43 < z < 0.70$ and has a sky coverage of 8498 deg^2 corresponding to an effective volume of $\sim$6 Gpc^3. We fit the Fourier space statistics, the power spectrum and bispectrum monopoles to measure the linear and quadratic bias parameters, b_1 and b_2, for a non-linear non-local bias model, the growth of structure parameter f and the amplitude of dark matter density fluctuations parametrized by σ_8. We obtain $b_1(z_{\rm eff})^{1.40}\sigma_8(z_{\rm eff}) = 1.672 \pm 0.060$ and $b_2^{0.30}(z_{\rm eff})\sigma_8(z_{\rm eff}) = 0.579 \pm 0.082$ at the effective redshift of the survey, $z_{\rm eff} = 0.57$. The main cosmological result is the constraint on the combination $f^{0.43}(z_{\rm eff})\sigma_8(z_{\rm eff}) = 0.582 \pm 0.084$, which is complementary to $f\sigma_8$ constraints obtained from two-point redshift-space distortion analyses. A less conservative analysis yields $f^{0.43}(z_{\rm eff})\sigma_8(z_{\rm eff}) = 0.584 \pm 0.051$. We ensure that our result is robust by performing detailed systematic tests using a large suite of survey galaxy mock catalogues and N-body simulations. The constraints on $f^{0.43}\sigma_8$ are useful for setting additional constraints on neutrino mass, gravity, curvature as well as the number of neutrino species from galaxy surveys analyses (as presented in a companion paper).

Key words: galaxies: haloes – cosmological parameters – cosmology: theory – large-scale structure of Universe.

1 INTRODUCTION

The small inflationary primordial density fluctuations are believed to be close to those of a Gaussian random field, thus their statistical properties are fully described by the power spectrum. Gravitational instability amplifies the initial perturbations but the growth eventually becomes non-linear. In this case the three-point correlation function and its counterpart in Fourier space, the bispectrum, are intrinsically second-order quantities, and the lowest-order statistics sensitive to non-linearities. These three-point statistics cannot only be used to test the gravitational instability paradigm but also to probe galaxy biasing and thus break the degeneracy between linear bias and the matter density parameter present in power spectrum measurements. Pioneering work on measuring the three-point statistics in a cosmological context are Peebles & Groth (1975), Groth & Peebles (1977) and Fry & Seldner (1982). The interpretation of these measurements had to wait for the development of non-linear cosmological perturbation theory, which showed how non-Gaussianity, and in particular the bispectrum, is generated by gravity and how (galaxy) biasing affects the bispectrum (Fry 1994). This advance started with the pioneering work of Goroff et al. (1986) and Fry (1984), and most of the theory was developed by the early 2000s (e.g. see Bernardeau et al. 2002 for a review). Before

⋆ E-mail: hector.gil@port.ac.uk (HG-M); Jorge.Norena@unige.ch (JN); liciaverde@icc.ub.edu (LV)

the bispectrum could be used to probe galaxy bias from galaxy redshift surveys, a full treatment of the redshift-space bispectrum for galaxies had to be developed (Matarrese, Verde & Heavens 1997; Heavens, Matarrese & Verde 1998; Scoccimarro et al. 1998; Verde et al. 1998; Scoccimarro, Couchman & Frieman 1999; Scoccimarro 2000). Starting around the year 2000, the golden era of cosmology started producing galaxies redshift surveys covering unprecedented volumes. Despite the number of power spectra analyses performed, the bispectrum work, especially with the goal of extracting cosmological information, from it, has been much less extensive (Feldman et al. 2001; Scoccimarro et al. 2001; Verde et al. 2002; Jing & Börner 2004; Wang et al. 2004; Gaztañaga & Scoccimarro 2005; Marín 2011; Marín et al. 2013). To date, bispectra analyses were performed out with the aim of constraining the bias parameters adopting a simple quadratic, local bias prescription. To extract the cosmological information, these constraints had to be combined with e.g. the measurement of $\beta = f/b$ – where f is the linear growth rate and b the linear galaxy bias – from redshift-space distortions of the power spectrum.

In this paper, we consider the galaxy bispectrum and power spectrum monopole of the CMASS galaxy sample of Sloan Digital Sky Survey III (SDSSIII) Baryon Oscillation Spectroscopic Survey (BOSS) Data Release 11 (DR11). By using jointly the power spectrum and bispectrum, we can constrain not only the bias parameters, but also the gravitational growth of clustering and in particular the combination $f^{0.43}\sigma_8$, where σ_8 denotes the linear rms of the dark matter density perturbations on scales of 8 h^{-1} Mpc. This quantity is particularly interesting as it may be used to probe directly the nature of gravity. In fact in general relativity (GR), the linear growth rate of perturbations is uniquely given by the expansion history. Therefore for a specified expansion history [such as the one measured by baryon acoustic oscillations (BAO) or by supernovae data], GR predicts the redshift evolution of σ_8 and f. Most of the tests of gravity on cosmological scales rely on the measurement of the anisotropic power spectrum in redshift space to constrain the combination $f\sigma_8$. In this paper, we offer a different constraint that arises from the combination of two- and three-point statistics. The fact that the f–σ_8 combinations of these two approaches differ offers the possibility of measuring both quantities from a combined analysis. We also present constraints on the relation between the clustering of mass and that of galaxies in the form of the combinations $b_1^{1.40}\sigma_8$ and $b_2^{0.30}\sigma_8$, where b_1 and b_2 are two bias parameters for an Eulerian non-local non-linear bias model, which we assume local in Lagrangian space (McDonald & Roy 2009; Baldauf et al. 2012; Chan, Scoccimarro & Sheth 2012; Saito et al. 2014). These constraints make possible the use of both shape and amplitude of the measured galaxy power spectrum in the mildly non-linear regime to constrain cosmological parameters. This paper is the first of a series of related works. In Gil-Marín et al. (2014b), we present the adopted model of the redshift-space bispectrum in the mildly non-linear regime. The full analysis of the survey is presented in two companion papers. In this paper, we present the details of the measurement of the power spectrum and bispectrum of the CMASS DR11 galaxy sample and all the systematic tests that evaluate the validity of the measurement. In the companion paper (Gil-Marín et al. 2014a), we focus on the cosmological interpretation of the constraints obtained in combination with other data sets such as cosmic microwave background (CMB) data.

The rest of this paper is organized as follows. In Section 2, we present a description of the CMASS DR11 data and of the resources used for calibrating and testing the theoretical models. In Section 3, we describe our methodology which includes the estimator used to measure the power spectrum and bispectrum from the galaxy catalogue, the modelling of mildly non-linear power spectra and bispectra for biased tracers in redshift space and the statistical method used to extract cosmological information from the measurements. In Section 4, we present the results including the set of best-fitting parameters and their errors, and Section 5 contains all the systematic tests that we have performed. Finally, in Section 6 we summarize the conclusions and anticipate future avenues of research.

2 THE REAL AND SYNTHETIC DATA

Our analysis of the BOSS galaxy sample relies heavily on calibration, testing and performance assessment using simulated and mock data. Here, we describe the real data we use along with their real-world effects, and the synthetic data in the form of mock surveys and N-body simulations.

2.1 The SDSSIII BOSS data

As part of the SDSSIII (Eisenstein et al. 2011), the Baryon Oscillations Spectroscopic Survey (BOSS; Bolton et al. 2012; Dawson et al. 2013; Smee et al. 2013) has measured the spectroscopic redshifts of about 1.2 million galaxies (and over 200 000 quasars). The galaxies are selected from multicolour SDSS imaging (Fukugita et al. 1996; Gunn et al. 1998; Smith et al. 2002; Gunn et al. 2006; Doi et al. 2010) covering a redshift range of $0.15 < z < 0.70$. The survey targeted two samples called LOWZ ($0.15 \leq z \leq 0.43$) and CMASS ($0.43 < z \leq 0.70$). In this work, we use only the CMASS sample. The BOSS survey is optimized for the measurement of the BAO scale from the galaxy power spectrum/correlation function and hence covers a large cosmic volume $V_{\rm eff} \simeq 6$ Gpc^3 with a number density of galaxies $n \sim 3 \times 10^{-4}$ $[h\,{\rm Mpc}^{-1}]^3$ to ensure that shot noise is not dominant at BAO scales (White et al. 2011).

Most of CMASS galaxies are red with a prominent break in their spectral energy distribution at 4000 Å , making the sample highly biased ($b \sim 2$). While this choice boosts the clustering signal at BAO scales, it renders the sample not optimal for bispectrum studies; the clustering boost comes at the expense of making the bias deviate from the simple linear, local, deterministic, Eulerian bias prescription. The bispectrum is much more sensitive than the power spectrum to these effects. The CMASS-DR11 sample covers 8498 deg^2 divided in a northern Galactic cap (NGC) with 6391 deg^2 and a southern Galactic cap (SGC) with 2107 deg^2. Our sample includes 520 806 galaxies in the north and 170 021 galaxies in the south. The effective redshift of the data set has been determined to be $z_{\rm eff} = 0.57$ in previous works (Anderson et al. 2012).

In order to correct several shortcomings of the CMASS data set (Ross et al. 2013; Anderson et al. 2014), three different incompleteness weights have been included; a redshift failure weight, $w_{\rm rf}$, a fibre collision weight, $w_{\rm fc}$ and a systematics weight, $w_{\rm sys}$, which combines a seeing condition weight and a stellar weight. Thus, each galaxy target is counted as

$$w_{\rm c} = (w_{\rm rf} + w_{\rm fc} - 1)w_{\rm sys}. \quad (1)$$

The redshift failure and fibre collision weights account for those galaxies that have been observed, but whose redshift has not been measured. This could be due to several reasons: two galaxies are too close to each other (<62 arcsec) to put two fibre detectors (fibre collision), or because the process of measuring of the redshift has simply failed. In both cases, these galaxies are still included in the catalogue by double counting the nearest galaxy, which is assumed to be statistically indistinguishable from the missing galaxy (see Ross et al. 2013 for details). The systematic weights account for fluctuations in the target density caused by changes in observational efficiency. The CMASS sample presents correlations between the galaxy density and the seeing in the imaging data used for targeting, as well as the proximity to a star. In order to correct for such effects, the systematic weights are designed to correct these variations giving an isotropic weighted field.

An additional weight that ensures the condition of minimum variance can be set (Feldman, Kaiser & Peacock 1994; Beutler et al. 2014),

$$w_{\rm FKP}(\boldsymbol{r}) = \frac{w_{\rm sys}(\boldsymbol{r})}{w_{\rm sys}(\boldsymbol{r}) + w_{\rm c}(\boldsymbol{r})n(\boldsymbol{r})P_0}, \quad (2)$$

where n is the mean number density of galaxies and P_0 is the amplitude of the galaxy power spectrum at the scale where the error is minimized, $k \sim 0.10\,h\,{\rm Mpc}^{-1}$. The effects of the inclusion of the weights in the shot noise term are discussed in Appendix A. Although the weighting scheme could in principle be improved for a population of differently biased tracers (Percival, Verde & Peacock 2004), the homogeneity of the CMASS galaxy population used here does not warrant the extra complication.

2.2 The mock survey catalogues and *N*-body simulations

In order to test the validity of some approximations and the systematic errors of the adopted modelling and approach, we use the following set of simulations.

(i) A set of 50 PTHALOS realizations in periodic boxes. These are halo catalogues created using the second-order Lagrangian Perturbation Theory (2LPT) matter field method by Manera et al. (2013) with flat Λ cold dark matter (CDM) cosmology. The box-size is 2.4 Gpc h^{-1}. The minimum mass of the 2LPT haloes is $m_{\rm p} = 5.0 \times 10^{12}\,{\rm M}_\odot\,h^{-1}$. In order to extract the halo field, a Cloud-in-Cell (hereafter CiC) prescription has also been used with 512^3 grid cells, whose size is $4.69\,{\rm Mpc}\,h^{-1}$. These realizations do not have any observational features such as the survey geometry or galaxy weights.

(ii) A set of 50 PTHALOS realizations with the survey geometry of the NGC CMASS sample from Data Release 10 (DR10; Ahn et al. 2014). Both DR10 and DR11 have a similar radial selection function, but DR11 has a more uniform angular survey mask than DR10. Thus, DR10 should present stronger mask effects than DR11. We therefore use DR10 to test the mask corrections we apply to the DR11 sample. This set has been constructed from the catalogue (i) applying the CMASS NGC DR10 survey mask. These catalogues are embedded in a box of $3500\,{\rm Mpc}\,h^{-1}$.[1] CiC prescription has been applied with 512^3 grid cells, which corresponds to a cell resolution of $6.84\,{\rm Mpc}\,h^{-1}$.

(iii) A set of five realizations of dark matter and 20 realizations of *N*-body haloes based on *N*-body dark matter particles simulations with box size $L_{\rm B} = 1.5\,{\rm Gpc}\,h^{-1}$ with periodic boundary conditions. The original mass of the dark matter particles is $m_{\rm p} = 7.6 \times 10^{10}\,{\rm M}_\odot\,h^{-1}$, and the minimum halo mass has been selected to be $7.8 \times 10^{12}\,{\rm M}_\odot\,h^{-1}$, which corresponds a bias of $b \sim 2$. The halo catalogues are generated by the Friends-of-Friends algorithm (Davis et al. 1985) with a linking length of 0.168 times the mean interparticle spacing. In order to extract the dark matter and halo field, a CiC prescription has also been used with 512^3 grid cells, whose size is $2.93\,{\rm Mpc}\,h^{-1}$. No observational features, such as survey geometry or galaxy weights, are incorporated.

(iv) A set of 600 + 600 realizations of mocks galaxies with the CMASS DR11 NGC and SGC survey geometry, respectively. This is the galaxy catalogue presented in Manera et al. (2013) based on PTHALOS. Galaxies have been added using a halo occupation distribution (HOD) prescription (see Manera et al. 2013 for details). These catalogues contain both survey geometry and galaxy weights.

Realizations (i)–(iv) are based on ΛCDM cosmology with matter density $\Omega_{\rm m} = 0.274$, cosmological constant $\Omega_\Lambda = 0.726$, baryon density $\Omega_{\rm b} = 0.04$, reduced Hubble constant $h = 0.7$, matter density fluctuations characterized by an $\sigma_8 = 0.8$ and power-law primordial power spectrum with spectral slope $n_{\rm s} = 0.95$ (as used in Anderson et al. 2012). All snapshots are at a redshift $z_{\rm sim} = 0.55$, which is very close to the effective redshift of the CMASS data $z_{\rm eff} = 0.57$. Under the assumption that GR is the correct description for gravity, the logarithmic growth factor at this epoch is $f(z_{\rm eff}) = 0.744$ and $\sigma_8(z_{\rm eff}) = 0.6096$.

(v) An additional set of dark matter *N*-body simulations is used in Section 5.1 only. They consist of an *N*-body dark matter particles simulation with flat ΛCDM cosmology slightly different from the (i)–(iv). The box size is $L_{\rm B} = 2.4\,{\rm Gpc}\,h^{-1}$ with periodic boundary conditions and the number of particles is $N_{\rm p} = 768^3$, with 60 independent runs. The cosmology used is the dark energy density, $\Omega_\Lambda = 0.73$, matter density, $\Omega_{\rm m} = 0.27$, Hubble parameter, $h = 0.7$, baryon density, $\Omega_{\rm b}h^2 = 0.023$, spectral index $n_{\rm s} = 0.95$ and the amplitude of the

[1] See fig. 11 of Manera et al. (2013) to see why we need a larger box than in (i).

primordial power spectrum at $z = 0$, $\sigma_8 = 0.7913$. Taking only the gravitational interaction into account, the simulation was performed with GADGET-2 code (Springel 2005). The snapshot used in this paper is at $z = 0$. In order to obtain the dark matter field from particles, we have applied the CiC prescription using 512^3 grid cells. Thus, the size of the grid cells is 4.68 Mpc h^{-1}.

3 METHOD

In this section, we describe the methodology used to extract the measurements of bias parameters and the growth of structure. The performance of our methodology, and the tests performed to quantify any possible systematic errors, are reported in Section 5.

3.1 Definitions

The power spectrum P and bispectrum B are the two- and three-point functions in Fourier space. For a cosmological overdensity field δ, they are defined as

$$\langle \delta_{\boldsymbol{k}} \delta_{\boldsymbol{k}'} \rangle \equiv (2\pi)^3 P(\boldsymbol{k}) \delta^{\rm D}(\boldsymbol{k} + \boldsymbol{k}'), \tag{3}$$

$$\langle \delta_{\boldsymbol{k}_1} \delta_{\boldsymbol{k}_2} \delta_{\boldsymbol{k}_3} \rangle \equiv (2\pi)^3 B(\boldsymbol{k}_1, \boldsymbol{k}_2) \delta^{\rm D}(\boldsymbol{k}_1 + \boldsymbol{k}_2 + \boldsymbol{k}_3), \tag{4}$$

where $\delta^{\rm D}$ is the Dirac delta distribution, $\delta_{\boldsymbol{k}} \equiv \int {\rm d}^3\boldsymbol{x}\, \delta(\boldsymbol{x}) \exp(-i\boldsymbol{k}\cdot\boldsymbol{x})$ is the Fourier transform of the overdensity $\delta(\boldsymbol{x}) \equiv \rho(\boldsymbol{x})/\overline{\rho} - 1$, where ρ is the dark matter density and $\bar{\rho}$ its mean value. Equation (4) shows that bispectrum can be non-zero only if the $\boldsymbol{k}$-vectors close to form a triangle.

In order to compute the galaxy power spectrum and bispectrum, we make use of the Feldman–Kaiser–Peacock estimator (FKP-estimator; Feldman et al. 1994), which has been used in previous analysis of bispectrum of galaxy surveys (Scoccimarro et al. 2001; Verde et al. 2002). The FKP galaxy fluctuation field is defined as

$$F_i(\boldsymbol{r}) \equiv w_{\rm FKP}(\boldsymbol{r}) \lambda_i \left[w_{\rm c}(\boldsymbol{r}) n(\boldsymbol{r}) - \alpha n_{\rm s}(\boldsymbol{r}) \right], \tag{5}$$

where n and $n_{\rm s}$ are, respectively, the observed number density of galaxies and the number density of a random catalogue, which is a synthetic catalogue Poisson sampled with the same mask and selection function as the survey but otherwise no intrinsic (cosmological) correlations; $w_{\rm c}$ and $w_{\rm FKP}$ were defined in equations (1) and (2), respectively; α is the ratio between the weighted number of observed galaxies over the random catalogue galaxies, $\alpha \equiv \sum_i^{N_{\rm gal}} w_{\rm c}/N_{\rm s}$, where $N_{\rm s}$ denotes the number of objects in the synthetic catalogue and $N_{\rm gal}$ the number of galaxies in the (real) catalogue. The pre-factor defined as λ_i is a normalization to be chosen to make the power spectrum (for index $i = 2$) and bispectrum (for index $i = 3$) estimators unbiased with respect to their definitions in equation (3)–(4). It is convenient to define the coefficients,

$$I_i \equiv \int {\rm d}^3\boldsymbol{r}\, w_{\rm FKP}^i(\boldsymbol{r}) \langle n w_{\rm c} \rangle^i(\boldsymbol{r}). \tag{6}$$

These factors play a key role in the normalization as shown below.

3.2 Estimating the power spectrum

The normalization for the power spectrum can be conveniently chosen, $\lambda_2 \equiv I_2^{-1/2}$, to match the theoretical power spectrum when $\bar{n}$ has no dependence on position. Thus, the galaxy power spectrum estimator used in this work is

$$F_2(\boldsymbol{r}) \equiv I_2^{-1/2} w_{\rm FKP}(\boldsymbol{r}) \left[w_{\rm c}(\boldsymbol{r}) n(\boldsymbol{r}) - \alpha n_{\rm s}(\boldsymbol{r}) \right]. \tag{7}$$

From this expression we obtain

$$\langle |F_2(\boldsymbol{k})|^2 \rangle = \int \frac{{\rm d}^3\boldsymbol{k}'}{(2\pi)^3} P_{\rm gal}(\boldsymbol{k}') |W_2(\boldsymbol{k} - \boldsymbol{k}')|^2 + P_{\rm noise}, \tag{8}$$

where $P_{\rm gal}$ is the theoretical prediction for the galaxy (or tracer) power spectrum in the absence of any observational effect, $P_{\rm noise}$ is the shot noise term (see Appendix A for the model used and Section 3.7) and W_2 is the window function, which is defined as

$$W_2(\boldsymbol{k}) \equiv I_2^{-1/2} \int {\rm d}^3\boldsymbol{r}\, w_{\rm FKP}(\boldsymbol{r}) \langle w_{\rm c} n \rangle(\boldsymbol{r}) {\rm e}^{+i\boldsymbol{k}\cdot\boldsymbol{r}}. \tag{9}$$

The random catalogue satisfies the expression $\langle w_{\rm c} n \rangle(\boldsymbol{r}) = \alpha \langle n_{\rm s} \rangle(\boldsymbol{r})$, and it can be therefore used to generate the window function. We do not consider correcting equation (8) by the integral constraint, because its effect is only relevant at larger scales that the ones considered in this paper.

We will designate the left-hand side of equation (8) $P^{\rm meas.}$ when F_2 is extracted from any of the catalogues (real or simulated) of Section 2.2. In Section 3.8, we will provide the details of the computation of F_2.

For any model $P(k)$, the convolution of equation (8) can be performed numerically in Fourier space in a minutes-time-scale on a single processor for a reasonably large number of grid-cells (such as 512^3 or 1024^3) using fftw.[2] An alternative option, which we do not adopt, would be to reduce the integral of equation (8) to a one-dimensional integral (Ross et al. 2013), defining a spherically averaged window function, and making the assumption that the power spectrum input is an isotropic function, although numerical results demonstrate that this is a good approximation. The model for $P_{\rm noise}$ in the presence of completeness weight and other real-world effects is presented in Appendix A. This derivation assumes that the shot noise follows Poisson statistics and the accuracy of the error estimation relies on the mocks having the same statistical properties for the shot noise as the data. For our final analysis of the data, we will treat the shot noise amplitude as a nuisance parameter and marginalize over it. This approach accounts for possible deviations from Poisson statistics as well as limitations of the mocks.

For the BOSS CMASS DR11 survey, $W_2(\boldsymbol{\epsilon})$ is a rapidly decreasing function with a width of $1/L_{\rm svy.}$, where $L_{\rm svy.}$ characterizes the typical size of the survey. Provided that $P_{\rm gal}(\boldsymbol{k})$ is smooth at small scales, the value of the integral in equation (8) tends to $P_{\rm gal}$ for large values of $\boldsymbol{k}$.

One of the FKP-estimator limitations is that the line-of-sight vector cannot be easily included in this formalism. This estimator is consequently only suitable for calculating monopole statistics (both power spectrum and bispectrum). Except for narrow angle surveys (Blake et al. 2013), higher order multipoles, such as the quadrupole or hexadecapole, require a more complex estimator, such as described by Yamamoto et al. (2006), as is implemented in Beutler et al. (2014) for the CMASS DR11 galaxy sample. In what follows, we will denote the monopole (angle average) of the right-hand side of equation (8) $P^{\rm model}(k)$, when $P_{\rm gal}(k)$ is the monopole (angle average) of equation (23) in Section 3.5.

3.3 Estimating the bispectrum

As for the power spectrum, we can define an FKP-style estimator for the bispectrum. In general, for the N-point correlation function, λ_N should be set to $I_N^{1/N}$ to provide an unbiased relation between $\langle F^N\rangle$ and the N-point statistical moment. Therefore, we set the normalization factor to $\lambda_3 \equiv I_3^{-1/3}$ and the galaxy field estimator for the bispectrum is

$$F_3(\boldsymbol{r}) \equiv I_3^{-1/3} w_{\rm FKP}(\boldsymbol{r})\left[w_{\rm c}(\boldsymbol{r})n(\boldsymbol{r}) - \alpha n_{\rm s}(\boldsymbol{r})\right]. \tag{10}$$

With this estimator, we can write

$$\langle F_3(\boldsymbol{k}_1)F_3(\boldsymbol{k}_2)F_3(\boldsymbol{k}_3)\rangle = \int \frac{{\rm d}^3\boldsymbol{k}'}{(2\pi)^3}\frac{{\rm d}^3\boldsymbol{k}''}{(2\pi)^3} B_{\rm gal}(\boldsymbol{k}', \boldsymbol{k}'')W_3(\boldsymbol{k}_1 - \boldsymbol{k}', \boldsymbol{k}_2 - \boldsymbol{k}'') + B_{\rm noise}(\boldsymbol{k}_1, \boldsymbol{k}_2), \tag{11}$$

where we always assume $\boldsymbol{k}_3 \equiv -\boldsymbol{k}_1 - \boldsymbol{k}_2$, that ensures that the three k-vectors form a triangle. As for the power spectrum, the expression for the shot noise, $B_{\rm noise}$, is derived in Appendix A and further discussed in Section 3.7. The window function W_3 can be written in terms of the window function of the power spectrum,

$$W_3(\boldsymbol{k}_A, \boldsymbol{k}_B) \equiv \frac{I_2^{3/2}}{I_3}\left[W_2(\boldsymbol{k}_A)W_2(\boldsymbol{k}_B)W_2^*(\boldsymbol{k}_A + \boldsymbol{k}_B)\right]. \tag{12}$$

Equations (11) and (12) can be derived from the definition of $F(\boldsymbol{r})$ in equation (5). We will designate the left-hand side of equation (11) $B^{\rm meas.}$ when F_3 is extracted from any of the catalogues (real or simulated) of Section 2.2. In Section 3.8, we provide the details about the computation of F_3 from a galaxy distribution.

Performing the double convolution between the window function and the theoretical galaxy bispectrum (equation 11) can be a challenging computation for a suitable number of grids cells (such as 512^3 or 1024^3). In this work, we perform an approximation that we have found to work reasonably well, which introduces biases that are negligible compared to the statistical errors of this survey. It consists of assuming that the input theoretical bispectrum is of the form $B_{\rm gal}(k_1, k_2, k_3) \sim P(k_1)P(k_2)\mathcal{Q}(k_1, k_2, k_3) + {\rm cyc}$, where $\mathcal{Q}$ can be any function of the three k-vectors. Then, ignoring the effect of the window function on $\mathcal{Q}$, the integral of equation (11) is separable. As a consequence, we can simply write

$$\begin{aligned}&\int \frac{{\rm d}^3\boldsymbol{k}'}{(2\pi)^3}\frac{{\rm d}^3\boldsymbol{k}''}{(2\pi)^3} B_{\rm gal}(\boldsymbol{k}', \boldsymbol{k}'')W_3(\boldsymbol{k}_1 - \boldsymbol{k}', \boldsymbol{k}_2 - \boldsymbol{k}'')\\ &= \int \frac{{\rm d}^3\boldsymbol{k}'}{(2\pi)^3}\frac{{\rm d}^3\boldsymbol{k}''}{(2\pi)^3} P(k')P(k'')\mathcal{Q}(k', k'', |\boldsymbol{k}' + \boldsymbol{k}''|)W_3(\boldsymbol{k}_1 - \boldsymbol{k}', \boldsymbol{k}_2 - \boldsymbol{k}'') \simeq [P \otimes W_2](k_1) \times [P \otimes W_2](k_2) \times \mathcal{Q}(k_1, k_2, k_3),\end{aligned} \tag{13}$$

where we have defined,

$$[P \otimes W_2](k_i) \equiv \int \frac{{\rm d}^3\boldsymbol{k}'}{(2\pi)^3} P(\boldsymbol{k}')|W_2(\boldsymbol{k}_i - \boldsymbol{k}')|^2. \tag{14}$$

This approximation works reasonably well for modes that are not too close to the size of the survey i.e. *all* three sides of the k-triangle are sufficiently large. The approximation fails to reproduce accurately the correct bispectrum shape when (at least) one of the k_i is close to the

[2] Fastest Fourier Transform in the West: http://fftw.org

fundamental frequency, $k_{\rm f} = 2\pi/L$, where L is the typical survey size. In particular for the geometry of CMASS DR11, this limitation only applies to triangle configurations where the modulus of one k-vector is much shorter than the other two ($k_3 \ll k1 \sim k2$, the so-called *squeezed* configuration) and the shortest k is $\lesssim 0.03\,h\,{\rm Mpc}^{-1}$. We test the efficiency of this estimator in Section 5.3.

In what follows, we will refer to the right-hand side of equation (11) as $B^{\rm model}$ where we will use the simplification of equation (13) and where we consider the galaxy (or tracer) bispectrum monopole for $P(k)P(k')\mathcal{Q}(k_1, k_2, k_3)$+cyc. when the expression for the redshift-space galaxy bispectrum is that reported in equation (26) in Section 3.6.

3.4 The galaxy bias model

The galaxy bias is defined as the mapping functional between the dark matter and the galaxy density field. When this relation is assumed to be local and deterministic we can generically write

$$\delta_g(\boldsymbol{x}) = \mathcal{B}[\delta(\boldsymbol{x})]\delta(\boldsymbol{x}), \tag{15}$$

where all possible non-linearities of the bias are encoded in the functional $\mathcal{B}$. A simple and widely used model for $\mathcal{B}$ is a simple Taylor expansion in δ (Fry & Gaztañaga 1993), often truncated at the first or second order (for bispectrum analyses of galaxy catalogues using this bias model see Feldman et al. 2001; Scoccimarro et al. 2001; Verde et al. 2002; Gaztañaga & Scoccimarro 2005 and Marín et al. 2013). While this model is still widely used in bispectrum forecasts, here we argue that it is insufficient for the precision and bias properties offered by the CMASS sample.

Recently it has been shown, by both analytical and numerical methods, that the gravitational evolution of the dark matter density field naturally induces non-local bias terms in the halo- (and therefore galaxy-) density field, even when the initial conditions are local (see Catelan et al. 1998 for initial investigations). Some of these non-local bias terms contribute at mildly non-linear scales and therefore they only introduce non-leading order corrections in the shape and amplitude of the power spectrum and bispectrum. However, other terms contribute at large scales, at the same level as the linear, local bias parameter, b_1 (McDonald & Roy 2009; Baldauf et al. 2012; Chan et al. 2012; Saito et al. 2014).

In practice, neglecting the non-local bias terms can produce a misestimation of the other bias parameters, even when working only at large, supposedly linear, scales. Feldman et al. (2001) were the first to apply a local Lagrangian bias to the IRAS PSCz survey catalogue (Infra-Red Astronomical Satellite Point Source Catalog; Saunders et al. 2000) and compare it with an Eulerian local bias model. Their results concluded that for that particular galaxy population the local Eulerian bias described better the data that the local Lagrangian bias with a likelihood ratio of $\mathcal{L}_E/\mathcal{L}_L = 1.6$. However, for N-body haloes, mock haloes and mock galaxies, we have checked that the local Eulerian description of the bias produces inconsistent results. In the Eulerian local bias model, the power spectrum requires a value of b_1 which is significantly higher than the one required by the bispectrum, even at large scales (both in real and in redshift space). In a similar way, the value of b_2 required by the halo–halo power spectrum is smaller than the one required by the power spectrum. These discrepancies are reduced when the Lagrangian local model is assumed (see for example Fig. 15, where the predictions from the power spectrum and bispectrum actually cross in a region). This result suggests that for the N-body and halo and galaxy catalogues used in this paper, the local Lagrangian bias model provides a better description than the local Eulerian bias model. Of course, we do not know whether for the observed CMASS BOSS Luminous Red Galaxies, this behaviour holds. However, for this point (and many others), we are assuming that the observed galaxy field is qualitatively similar to the simulated galaxy field, and therefore, seems us reasonable to assume the local Lagrangian model instead of local Eulerian for the bias model.

Hence, we use the Eulerian non-linear and non-local bias model proposed by McDonald & Roy (2009). The non-local terms are included through a quadratic term in the tidal tensor $s(\boldsymbol{x}) = s_{ij}(\boldsymbol{x})s_{ij}(\boldsymbol{x})$, with $s_{ij}(\boldsymbol{x}) = \partial_i\partial_j\Phi(\boldsymbol{x}) - \delta^{\rm Kr}_{ij}\delta(\boldsymbol{x})$. Here, $\Phi(\boldsymbol{x})$ is the gravitational potential, $\nabla^2\Phi(\boldsymbol{x}) = \delta(\boldsymbol{x})$. With this non-local term, our adopted second-order expression for the relation between δ_g and δ is

$$\delta_g(\boldsymbol{x}) = b_1\delta(\boldsymbol{x}) + \frac{1}{2}b_2[\delta(\boldsymbol{x})^2 - \sigma_2] + \frac{1}{2}b_{s^2}[s(\boldsymbol{x})^2 - \langle s^2\rangle] + \text{higher order terms}, \tag{16}$$

where b_1 is the linear bias term, b_2 is the non-linear bias term and b_{s^2} the non-local bias term. The terms σ_2 and $\langle s^2\rangle$ ensure the condition $\langle\delta_g\rangle = 0$. Most of the third-order terms in δ_g contribute to fourth and higher order corrections in the power spectrum and bispectrum and will not be considered in this paper; however, for the power spectrum, some contributions coming from these terms are not negligible at second order and must be considered (see McDonald & Roy 2009 for a full discussion). We refer to this extra bias term as $b_{3{\rm nl}}$. In Fourier space, equation (16) reads

$$\delta_g(\boldsymbol{k}) = b_1\delta(\boldsymbol{k}) + \frac{1}{2}b_2\int\frac{{\rm d}\boldsymbol{q}}{(2\pi)^3}\,\delta(\boldsymbol{q})\delta(\boldsymbol{k}-\boldsymbol{q}) + \frac{1}{2}b_{s^2}\int\frac{{\rm d}\boldsymbol{q}}{(2\pi)^3}\,\delta(\boldsymbol{q})\delta(\boldsymbol{k}-\boldsymbol{q})S_2(\boldsymbol{q},\boldsymbol{k}-\boldsymbol{q}) + \text{higher order terms}, \tag{17}$$

where we ignore the contributions of σ_2 and $\langle s^2\rangle$ to the $k = 0$ mode, which is not observable. S_2 is related to the $s_{ij}(\boldsymbol{x})$ field as

$$s^2(\boldsymbol{k}) = \int\frac{{\rm d}\,\boldsymbol{k}'}{(2\pi)^3}\,S_2(\boldsymbol{k}', \boldsymbol{k}-\boldsymbol{k}')\delta(\boldsymbol{k}')\delta(\boldsymbol{k}-\boldsymbol{k}'), \tag{18}$$

where $s^2(\boldsymbol{k})$ is just the Fourier transform of $s^2(\boldsymbol{x})$ field. This relation implies that the S_2 kernel is defined as

$$S_2(\boldsymbol{q}_1, \boldsymbol{q}_2) \equiv \frac{(\boldsymbol{q}_1 \cdot \boldsymbol{q}_2)^2}{(q_1 q_2)^2} - \frac{1}{3}. \tag{19}$$

The bias model of equation (17) depends on four different bias parameters, b_1, b_2, b_{s^2} (which appear both in the power spectrum and bispectrum) and also $b_{3\mathrm{nl}}$ that contributes the second order in the power spectrum. In this paper, we assume that, although the galaxy bias is non-local in Eulerian space, it is local in Lagrangian space. Under this assumption, the non-local bias terms can be related at first order to the linear bias term b_1,[3]

$$b_{s^2} = -\frac{4}{7}(b_1 - 1) \quad \text{(Baldauf et al. 2012; Chan et al. 2012)}, \tag{20}$$

$$b_{3\mathrm{nl}} = \frac{32}{315}(b_1 - 1) \quad \text{(Beutler et al. 2014; Saito et al. 2014)}. \tag{21}$$

With these relations, we are able to express the galaxy biasing as a function of only two free parameters, b_1 and b_2. Equation (17) is the starting point for computing the galaxy power spectrum and bispectrum.

The second-order bias parameter, b_2 can be quite sensitive to truncation effects. In this sense, b_2 should be treated as an effective parameter that absorbs part of the higher order contributions that are not considered when we truncate equation (17) at second order. In another work (Gil-Marín et al. 2014b), it has been reported that even for dark matter, b_2 can present non-zero values due to these sort of effects. We therefore treat b_2 as a nuisance parameter, to be marginalized over.

3.5 The power-spectrum model

The real-space galaxy power spectrum $P_{g,\,\delta\delta}(k)$, can be written as a function of the statistical moments of dark matter using equation (17) and perturbation theory as (see McDonald & Roy 2009; Beutler et al. 2014)

$$P_{g,\delta\delta}(k) = b_1\left[b_1 P_{\delta\delta}(k) + 2b_2 P_{b2,\delta}(k) + 2b_{s^2} P_{bs2,\delta}(k) + 2b_{3\mathrm{nl}}\sigma_3^2(k)P^{\mathrm{lin}}(k)\right] + b_2[b_2 P_{b22}(k) + 2b_{s^2} P_{b2s2}(k)] + b_{s^2}^2 P_{bs22}(k), \tag{22}$$

where P^{lin} and $P_{\delta\delta}$ are the linear and non-linear matter power spectrum, respectively. The other terms correspond to one-loop corrections due to higher order bias terms and their explicit form can be found in Appendix B.

The mapping from real space to redshift-space quantities involves the power spectrum of the velocity divergence $\theta(\boldsymbol{k}) = [-i\boldsymbol{k} \cdot \boldsymbol{v}(\boldsymbol{k})]/[af(a)H]$. We assume that there is no velocity bias between the underling dark matter field and the galaxy field at least on the relatively large scales of interest. According to Taruya, Nishimichi & Saito (2010) and (Nishimichi & Taruya 2011, hereafter TNS model), the galaxy power spectrum in redshift space can be approximated as

$$P_g^{(s)}(k,\mu) = D_{\mathrm{FoG}}^P(k,\mu,\sigma_{\mathrm{FoG}}^P[z])\left[P_{g,\delta\delta}(k) + 2f\mu^2 P_{g,\delta\theta}(k) + f^2\mu^4 P_{\theta\theta}(k) + b_1^3 A(k,\mu,f/b_1) + b_1^4 B(k,\mu,f/b_1)\right], \tag{23}$$

where μ denotes the cosine of the angle between the k-vector and the line of sight, f is the linear growth rate $f = \partial \ln\delta/\partial \ln a$, and $P_{g,\,\delta\delta}(k)$ is given by equation (22). The quantities $P_{g,\,\delta\theta}$, and $P_{\theta\theta}$, are the non-linear power spectra for the galaxy density–velocity, and the dark matter velocity–velocity, respectively. The expressions for all these terms are reported in Appendix B; here it will suffice to say that the model for the non-linear matter quantities is obtained using resummed perturbation theory (hereafter RPT) at two-loop as is described in (Gil-Marín et al. 2012b, hereafter 2L-RPT).

The factor D_{FoG}^P is often referred to as the Fingers-of-God (hereafter FoG) factor and accounts for the non-linear damping due to the velocity dispersion of satellite galaxies ($\sigma_{\mathrm{FoG}}^P[z]$) inside the host halo. However, we treat this factor as an effective parameter that enclose our poor understanding of the non-linear redshift-space distortions and to be marginalized over. The expression adopted for D_{FoG}^P is also reported in Appendix B.

The angular dependence of the redshift-space power spectrum is often expanded in Legendre polynomials (see Appendix B for details). Here, we will only consider the monopole, i.e. the angle-averaged power spectrum. For this reason, our analysis is complementary to and independent of that of Beutler et al. (2014), Chuang et al. (2013), Samushia et al. (2014) and Sánchez et al. (2014), who use the quadruple to monopole ratio. However, this does not mean that the results presented here and their results can be combined as if they were independent measurements (the survey is the same); we will explore in future work whether error-bars could be further reduced by combining the two approaches.

3.6 The bispectrum model

The galaxy-bispectrum in real space can be written using to the bias model of equation (17) as

$$B_g(k_1,k_2,k_3) = b_1^3 B(k_1,k_2,k_3) + b_1^2\left[b_2 P(k_1)P(k_2) + b_{s^2} P(k_1)P(k_2)S_2(\boldsymbol{k}_1,\boldsymbol{k}_2) + \mathrm{cyc.}\right], \tag{24}$$

[3] If we incorporate the pre-factor 1/2 in the bias parameter b_{s^2}, then the relation changes to $b_{s^2} = -\frac{2}{7}(b_1 - 1)$.

where P and B are the non-linear matter power spectrum and bispectrum, respectively, and we have neglected terms proportional to b_2^2, $b_{s^2}^2$, which are of higher order. Using the 2L-RPT model for the matter bispectrum proposed by Gil-Marín et al. (2012a), we can express the real space galaxy bispectrum as a function of the non-linear matter power spectrum and the effective kernel, $\mathcal{F}_2^{\rm eff}(\boldsymbol{k}_1, \boldsymbol{k}_2)$ (see Gil-Marín et al. 2012a and Appendix C),

$$B_g(k_1, k_2, k_3) = 2P(k_1)P(k_2)\left[b_1^3\mathcal{F}_2^{\rm eff}(\boldsymbol{k}_1, \boldsymbol{k}_2) + \frac{b_1^2 b_2}{2} + \frac{b_1^2 b_{s^2}}{2}S_2(\boldsymbol{k}_1, \boldsymbol{k}_2)\right] + \text{cyc.}\,. \tag{25}$$

The non-local bias (b_{s2}) contributes to the leading order and introduces a new shape dependence through the kernel S_2 (defined in equation 19), which was not present in the matter bispectrum. In this case, we do not consider the contribution of $b_{3\rm nl}$ because for the bispectrum (in contrast to the power spectrum) it only appears in fourth and higher order corrections in δ_g.

Redshift-space distortions can be included in this model by introducing an effective kernel $Z_2^{\rm eff}(k_1, k_2, \boldsymbol{\Psi})$ (Gil-Marín et al. 2014b and Appendix C), where $\boldsymbol{\Psi}$ denotes the parameters to be fitted, of which the ones of interest are f, b_1, b_2, b_{s^2}. With this the galaxy bispectrum in redshift space as a function of the non-linear real-space matter power spectrum is (Gil-Marín et al. 2014b)

$$B_g^{(s)}(\boldsymbol{k}_1, \boldsymbol{k}_2) = D_{\rm FoG}^B(k_1, k_2, k_3, \sigma_{\rm FoG}^B[z])\left[2P(k_1)\,Z_1(\boldsymbol{k}_1)\,P(k_2)\,Z_1(\boldsymbol{k}_2)\,Z_2^{\rm eff}(\boldsymbol{k}_1, \boldsymbol{k}_2) + \text{cyc.}\right], \tag{26}$$

where Z_1 denotes the redshift-space kernel predicted by standard perturbation theory (SPT) and the $Z_2^{\rm eff}$ kernel is a phenomenological extension of the SPT kernel Z_2 (for a detailed derivation and explicit expressions, see Appendix C). The $D_{\rm FoG}^B$ term is a damping factor that aims to describe the FoG effect due to velocity dispersion inside virialized structures through the one-free parameter, $\sigma_{\rm FoG}^B$, which we will also marginalize over. Here, $\sigma_{\rm FoG}^B$ is a different (nuisance) parameter from $\sigma_{\rm FoG}^P$ in equation (23). In this paper, we will treat $\sigma_{\rm FoG}^P$ and $\sigma_{\rm FoG}^B$ as independent parameters although they may be weakly correlated. The adopted expression for $D_{\rm FoG}^B$ is reported in equation (C15) in Appendix C.

As for the power spectrum, we can expand the redshift-space bispectrum in multipoles (see Appendix C for details); here, we will consider only the monopole (i.e. the μ angle-averaged bispectrum).

Note that we are truncating the bispectrum description at a different order than the power spectrum. The description of the power spectrum is based on a physical, perturbative, model; is very accurate at large scales (few per cent) until it dramatically breaks down, and cannot be applied anymore. On the other hand, the bispectrum description is phenomenological; has an accuracy of 5 per cent at large scales and gradually deviate from the prediction of N-body. Therefore, is natural to expect that these two models present different ranges of validity when they are applied to biased objects. In this paper, we have opted to describe each statistic the best we can, even if this means truncating the power spectrum and bispectrum models at different scales and different orders.

3.7 Shot noise

Discreteness introduces extra spurious power to both the power spectrum and bispectrum. In this paper, we consider that the (additive) shot noise contribution may be modified from that of a pure Poisson sampling. We parametrize this deviation through a free parameter, $A_{\rm noise}$,

$$P_{\rm noise} = (1 - A_{\rm noise})P_{\rm Poisson}, \tag{27}$$

$$B_{\rm noise}(\boldsymbol{k}_1, \boldsymbol{k}_2) = (1 - A_{\rm noise})B_{\rm Poisson}(\boldsymbol{k}_1, \boldsymbol{k}_2), \tag{28}$$

where the terms $P_{\rm Poisson}$ and $B_{\rm Poisson}(\boldsymbol{k}_1, \boldsymbol{k}_2)$ are the Poisson predictions for the shot noise; their expression can be found in Appendix A. For $A_{\rm noise} = 0$ we recover the Poisson prediction, whereas when $A_{\rm noise} > 0$ we obtain a sub-Poisson shot noise term and $A_{\rm noise} < 0$ a super-Poisson noise term. The extreme case of $A_{\rm noise} = 1$ corresponds to a sub-Poissonian noise that is null; $A_{\rm noise} = -1$ correspond to a super-Poissonian noise that doubles the Poisson prediction. We expect that the observed noise is always contained between these two extreme cases, so we constrain the $A_{\rm noise}$ parameter to be, $-1 \leq A_{\rm noise} \leq +1$.

3.8 Measuring power spectrum and bispectrum of CMASS galaxies from the BOSS survey

In order to compute the power spectrum and bispectrum from a set of galaxies, we need to compute the suitably weighted field $F_i(\boldsymbol{x})$ described in Section 3.3. We use a random catalogue of number density of $\bar{n}_{\rm s}(\boldsymbol{r}) = \alpha^{-1}\bar{n}(\boldsymbol{r})$ with $\alpha \simeq 0.002\,55$, and therefore $\alpha^{-1} \simeq 400$. In order to do so, we place the NGC and SGC galaxy samples in boxes which we discretize in grid-cells, using a box with side of $3500\,h^{-1}$ Mpc to fit the NGC galaxies and of $3100\,h^{-1}$ Mpc for the SGC galaxies.

The number of grid cells used for the analysis is 512^3. This corresponds to a grid-cell resolution of $6.84\,h^{-1}$ Mpc for NGC and $6.05\,h^{-1}$ Mpc for SGC. The fundamental wave-lengths are $k_{\rm f} = 1.795 \cdot 10^{-3}\,h\,{\rm Mpc}^{-1}$ and $k_{\rm f} = 2.027 \cdot 10^{-3}\,h\,{\rm Mpc}^{-1}$ for the NGC and SGC boxes, respectively. We have checked that for $k \leq 0.25\,h\,{\rm Mpc}^{-1}$, doubling the number of grid-cells per side, from 512^3 to 1024^3, produces a negligible change in the power spectrum. This result indicates that using 512^3 grid-cells provides sufficient resolution at the scales of interest.

We apply the CiC method to associate galaxies to grid-cells to obtain the quantity $F_i(\boldsymbol{r})$ of equation (5) on the grid.

To obtain $P^{\rm meas.}(\boldsymbol{k}) = \langle |F_2(\boldsymbol{k})|^2 \rangle$, we bin the power spectrum k-modes in 60 bins between the fundamental frequency $k_{\rm f}$ and the maximum frequency for a given grid-size with width $\Delta \log_{10} k = [\log_{10}(k_{\rm M}) - \log_{10}(k_{\rm f})]/60$, where $k_{\rm M} \equiv \sqrt{3} k_{\rm f} N_{\rm grid}/2$ is the maximum frequency and $N_{\rm grid}$ is the number of grid-cells per side, in this case 512.

We use the real part of $\langle F_{\boldsymbol{k}_1} F_{\boldsymbol{k}_2} F_{\boldsymbol{k}_3} \rangle$ as our data for the bispectrum, for triangles in $\boldsymbol{k}$-space (i.e. where $\boldsymbol{k}_1 + \boldsymbol{k}_2 + \boldsymbol{k}_3 = \boldsymbol{0}$). Therefore, we have $B^{\rm meas.}(\boldsymbol{k}_1, \boldsymbol{k}_2, \boldsymbol{k}_3) = {\rm Re}\,[\langle F_3(\boldsymbol{k}_1) F_3(\boldsymbol{k}_2) F_3(\boldsymbol{k}_3) \rangle]$. There is clearly a huge number of possible triangular shapes to investigate; it is not feasible in practice to consider them all. However, is not necessary to consider all possible triplets as their bispectra are highly correlated. As shown in Matarrese et al. (1997), triangles with one k-vector in common are correlated, through cross-terms in the six-point function. In addition, the survey window function induces mode coupling which correlates different triplets further. In particular, in this paper we focus on those triangles with $k_2/k_1 = 1$ and 2, allowing k_3 to vary from $|\boldsymbol{k}_1 - \boldsymbol{k}_2|$ to $|\boldsymbol{k}_1 + \boldsymbol{k}_2|$.

We choose to bin k_1 and k_3 in fundamental k-bins of $\Delta k_1 = \Delta k_3 = k_{\rm f}$. Additionally, k_2 is binned in fundamental k-bins when $k_1 = k_2$. However, for those triangles with $k_2/k_1 = 2$ we bin k_2 in k-bins of $2k_{\rm f}$ in order to cover all the available k-space. Thus, generically we can write $\Delta k_2 = (k_2/k_1)\Delta k_1$. We have checked that changing the bin-size has a negligible impact on the best-fitting parameters as well as on their error. We present results in the plots using the bin size adopted in the analysis.

The measurement of the bispectrum is performed with an approach similar to that described in Appendix A of Gil-Marín et al. (2012a). Given fixed k_1, k_2 and k_3, and a k_i-bin, defined by Δk_1, Δk_2 and Δk_3, we define the region that satisfies, $k_i - \Delta_{k_i}/2 \leq q_i \leq k_i + \Delta_{k_i}/2$. There are a limited number of *fundamental* triangles in this k-space region, with the number depending on

$$V_B(k_1, k_2, k_3) = \int_{\mathcal{R}} {\rm d}\boldsymbol{q}_1\, {\rm d}\boldsymbol{q}_2,\ {\rm d}\boldsymbol{q}_3\, \delta^D(\boldsymbol{q}_1, \boldsymbol{q}_2, \boldsymbol{q}_3) \simeq 8\pi^2 k_1 k_2 k_3 \Delta_{k_1} \Delta_{k_2} \Delta_{k_3}, \tag{29}$$

where the $\simeq$ becomes an equality when $\Delta_{k_i} \ll k_i$. The value of the bispectrum is defined as the mean value of these fundamental triangles. Instead of trying to find these triangles, we cover this $\mathcal{R}$-region with k-triangles randomly orientated in the k-space. The mean value of these random triangles tends to the mean value of the fundamental triangles when the number of random triangles is sufficiently large. We have empirically found that the number of random triangles that we must generate to produce convergence to the mean value of the bispectrum is $\sim 5 V_B(k_1, k_2, k_3)/k_{\rm f}^6$, where $k_{\rm f} \equiv 2\pi/L_{\rm B}$ is the fundamental wavelength, and $L_{\rm B}$ the size of the box. For each choice of k_i, Δk_i , $\{i = 1, 2, 3\}$ provides us an estimate of what we call a single bispectrum *mode*.

When we perform the fitting process to the data set, we need to specify the minimum and maximum scales to consider. The largest scale we use for the fitting process is $0.03\,h\,{\rm Mpc}^{-1}$. This large-scale limit is caused by the survey geometry of the bispectrum (see Section 5.3 for details). The smaller the minimum scale, the more k-modes are used and therefore the smaller the statistical errors. On the other hand, small scales are poorly modelled in comparison to large scales, such that we expect the systematic errors to grow as the minimum scale decreases. Therefore, we empirically find a compromise between these two effects such that the statistical and systematic errors are comparable. To do so, we perform different best-fitting analysis for different minimum scales and find the corresponding maximum k by identifying changes on the best-fitting parameters that are larger than the statistical errors as we increase the minimum scale.

In the following, when we report a $k_{\rm max}$ value, this means that none of the $k_{1,2,3}$ of the bispectrum triangles can exceed this value. In addition, our triangle catalogue is always limited by $k_1 \leq 0.1\,h\,{\rm Mpc}^{-1}$ when $k_2/k_1 = 2$ and $k_1 \leq 0.15\,h\,{\rm Mpc}^{-1}$ when $k_2/k_1 = 1$, because of computational reasons.

The number of modes used is typically $\sim$5000. If we wanted to use the mock catalogues to estimate the full covariance of both quantities (power spectrum and bispectrum), we would need to drastically reduce the number of bins (and modes), so that the total number of (covariance) matrix elements is much smaller than the number of mocks (currently 600 CMASS mocks are available). This could be achieved by increasing the k-bin size, but with the drawback of a significant loss of shape information. For this reason, we will only estimate from the mock catalogues the diagonal elements of the covariance ($\sigma_P^2[k]$, $\sigma_B^2[k_1, k_2, k_3]$), and use these as described in the next section.

3.9 Parameter estimation

Both the power spectrum and bispectrum in redshift space depend on cosmologically interesting parameters, the bias parameters as well as nuisance parameters. The dependence is described in details in the above subsections.

In total, for the full model, we have seven free parameters $\boldsymbol{\Psi} = \{b_1, b_2, f, \sigma_8, A_{\rm noise}, \sigma_{\rm FoG}^P, \sigma_{\rm FoG}^B\}$.

(i) Two parameters constrain the bias b_1 and b_2. Under the assumption of local Lagrangian bias, b_1 determines the value for b_{s^2} and $b_{\rm nl3}$.
(ii) Two FoG, redshift-space distortion, parameters $\sigma_{\rm FoG}^P$ and $\sigma_{\rm FoG}^B$.
(iii) A shot noise amplitude parameter $A_{\rm noise}$.
(iv) The logarithmic growth factor parameter f. This parameter can be predicted for a given cosmological model (in particular if $\Omega_{\rm m}$ is known) if we assume a theory for gravity. However, in this paper we consider this parameter free in order to test possible deviations from GR or, if assuming GR, for not using a prior on $\Omega_{\rm m}$.
(v) The amplitude of the primordial dark matter power spectrum, σ_8.

The other cosmological parameters, including $\Omega_{\rm m}$, the spectral index $n_{\rm s}$, and the Hubble parameter h are assumed fixed to their fiducial values in the fitting process. In most cases, they are set to the best-fitting values obtained by the *Planck* mission based on the CMB analysis (Planck Collaboration XVI 2014) in a flat ΛCDM model. We refer to these set of parameters as Planck13; they are listed in Table 4. In

selected occasions, we will change this set of fiducial parameters to assess how our analysis depends on this assumption. The dependence on $\Omega_{\rm m}$ is largely absorbed by having f as a fitted parameter.

The probability distribution for the bispectrum in the mildly non-linear regime is not known (although some progress are being made see e.g. Matsubara 2007); even if one invokes the central limit theorem and model the distribution of bispectrum modes as a multivariate Gaussian, the evaluation of its covariance would be challenging (see e.g. equations 38– 42 of Matarrese et al. 1997, appendix A of Verde et al. 1998 and discussion above). In addition, we want to analyse jointly the power spectrum and the bispectrum whose joint distribution is not known. Another approach is therefore needed. We opt for the approach proposed in Verde et al. (2002), which consists of introducing a suboptimal but unbiased estimator. Given an underlying cosmological model, $\mathbf{\Omega}$, and a set of free parameters to be fitted, $\mathbf{\Psi}$, the power spectrum and bispectrum can be written as

$$P^{\rm model}(k) = P^{\rm model}(k, \mathbf{\Psi}; \mathbf{\Omega}) \text{ and } \; B^{\rm model}(k_1, k_2, k_3) = B^{\rm model}(k_1, k_2, k_3, \mathbf{\Psi}; \mathbf{\Omega}). \tag{30}$$

We then construct the $\chi^2_{\rm diag.}$-function as

$$\chi^2_{\rm diag.}(\mathbf{\Psi}) = \sum_{k-{\rm bins}} \frac{\left[P^{\rm meas.}_{(i)}(k) - P^{\rm model}(k, \mathbf{\Psi}; \mathbf{\Omega})\right]^2}{\sigma_P(k)^2} + \sum_{\rm triangles} \frac{\left[B^{\rm meas.}_{(i)}(k_1, k_2, k_3) - B^{\rm model}(k_1, k_2, k_3, \mathbf{\Psi}; \mathbf{\Omega})\right]^2}{\sigma_B(k_1, k_2, k_3)^2}, \tag{31}$$

where we have ignored the contribution from off-diagonal terms, and we take into account only the diagonal terms, whose errors are given by σ_P and σ_B, which are obtained directly from the mock catalogues.

We use a Nelder–Mead based method of minimization (Press et al. 1992). We impose some mild priors: $b_1 > 0, f > 0$ and, in some cases, we also require $b_2 > 0$. As will be clear in Section 5.5.3, the $b_2 > 0$ prior has no effect on the results but it makes it easier to find the minimum for some of the mocks realizations.

We obtain a set of parameters that minimizes $\chi^2_{\rm diag.}$ for a given realization, i, namely $\mathbf{\Psi}_{(i)}$. By ignoring the off diagonal terms of the covariance matrix (and the full shape of the likelihood), we do not have a have maximum likelihood estimator which is necessarily minimum variance, optimal or unbiased. However, we will demonstrate with tests on N-body simulations that this approximation does not bias the estimator

Therefore, (a) the particular value of the $\chi^2_{\rm diag.}$ at its minimum is meaningless and should not be used to estimate a goodness of fit and (b) the errors on the parameters cannot be estimated by standard $\chi^2_{\rm diag.}$ differences. The key property of this method is that $\langle \mathbf{\Psi}_{(i)} \rangle$ is an unbiased estimator of the true set $\mathbf{\Psi}_{\rm true}$ and that the dispersion of $\mathbf{\Psi}_{(i)}$ is an unbiased estimator of the error: $\mathbf{\Psi}_{\rm true}$ should belong to the interval $\langle \mathbf{\Psi}_{\rm i} \rangle \pm \sqrt{\langle \mathbf{\Psi}^2_{\rm i} \rangle - \langle \mathbf{\Phi}_{\rm i} \rangle^2}$ with roughly 68 per cent confidence.[4]

We can demonstrate the suboptimality analytically as follows. The Cramer–Rao bound says that the error for any unbiased estimator is always greater or equal to the square root of the inverse of the Fisher information matrix. The maximum likelihood estimator is asymptotically the best unbiased estimator that saturates the Cramer–Rao bound (i.e. you cannot do better than a maximum-likelihood estimator). Using the full covariance would correspond to do a maximum likelihood estimator in the region around the maximum, or otherwise said, using the Laplace approximation. This would be the best unbiased estimator saturating the Cramer–Rao bound. Using only the diagonal elements therefore gives a suboptimal estimator. Always in the limit of the Laplace approximation, this estimator will still be unbiased. In practice, the maximum likelihood estimator might not be strictly unbiased (it is only asymptotically and we have made the Laplace approximation to arrive to the above conclusion). Therefore, we have checked that effectively the estimator is unbiased empirically; applying it to a case where the bias parameters are known, such as CDM simulations. As it was included in the text, this technique was used in Verde et al. (2002), and it has been recently applied successfully in Gil-Marín et al. (2014b).

We will follow this procedure, using the 600 mock galaxy surveys from Manera et al. (2013), we estimate the errors from the CMASS DR11 data set in Section 4. Since the realizations are independent, the dispersion on each parameter provides the associated error for a single realization. This is true for the NGC and SGC alone, but not for the combined sample NGC+SGC. Both NGC and SGC catalogues were created from the same set of 600 boxes of size 2400 h^{-1} Mpc, just sampling a subsection of galaxies of these boxes to match the geometry of the survey. For the DR11 BOSS CMASS galaxy sample, it was not possible to sample NGC and SGC from the same box without overlap, as in for previous releases such as DR9 (Ahn et al. 2012). In particular, for DR11 the full southern area is contained in the NGC (see section 6.1 of Percival et al. 2014 for more details). Thus, to compute the errors of the combined NGC+SGC sample one must use different boxes for the northern and southern components. We estimate the errors simply sampling the NGC from one subset of 300 realizations and combine them with the samples of the SGC from the other subset. In the same manner, we can make another estimation sampling the NGC and SGC from the other subset of 300, respectively. We simply combine both predictions taking their mean value. Although we know that the error-bars must somewhat depend on the assumed cosmology (and bias) in the mocks, in this work we consider this dependence negligible.

Note that since we are using 300 realizations to estimate the errors on a larger amount of k-bins (around 5000), the errors obtained may present inaccuracies respect to their expected value. A check on the performance of this approximation, accuracy of the estimated errors and effects on the recovered parameters, is presented in the appendix A of Gil-Marín et al. (2012a) for dark matter in real space. There, using

[4] The estimate of the confidence can only be approximate for three reasons (a) the error distribution is estimated from a finite number of realizations (b) the realizations might not have the same statistical properties of the real Universe and the errors might slightly depend on that (c) the distribution could be non-Gaussian.

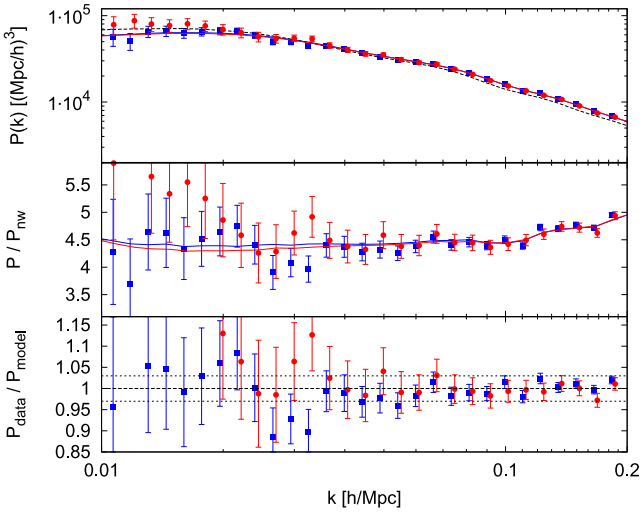

Figure 1. Power spectrum data for the NGC (blue squares) and the SGC (red circles) versions and the best-fitting model prediction (red and blue lines) according to NGC+SGC Planck13 (Table 1). Blue lines take into account the NGC mask and red lines the SGC mask. The top panel shows the power spectrum, middle panel the power spectrum normalized by a non-wiggle linear power spectrum for clarity, and the bottom panel the relative deviation of the data from the model. The black dotted lines in the bottom panel mark the 3 per cent deviation respect to the model. In the top panel, the average mocks power spectrum is indicated by the black dashed line. The model and the data show an excellent agreement within 3 per cent accuracy for the entire k-range displayed.

40 realizations, the errors are estimated from the dispersion among realizations and compared with the (Gaussian) analytic predictions. The result is that the errors estimated from the 40 realizations agree to a ∼30 per cent accuracy with the analytic predictions up to $k \sim 0.2\,h\,\mathrm{Mpc}^{-1}$. However, we want to stress that the methodology considered here is not very sensitive to the accuracy of how the errors are estimated. If the errors were overestimated by a constant factor, the best-fitting values of $\mathbf{\Psi}_{(i)}$ would be unaffected, and the variance among $\mathbf{\Psi}_{(i)}$ will be unchanged, as it is estimated *à la* Monte Carlo. If the errors were misestimated by shape-dependent factors, the estimator would be less-optimal, but still unbiased. Therefore, the validity of the methodology does not rely on the accuracy of the error-estimation, only its optimality.

4 RESULTS

We begin by presenting the measured power spectrum and bispectrum and later discuss the best-fitting model and the constraints on the parameters of interest.

The top panel of Fig. 1 presents the power spectrum monopole of CMASS DR11 data measurements for NGC (blue squares) and SGC (red circles) galaxy samples. The model prediction using the best-fitting parameters corresponding to NGC + SGC is also shown and the best-fitting parameters values are reported in Table 1. The blue solid line includes the NGC mask effect and red solid line the SGC mask. We also show for reference the averaged value of the 600 realizations of the NGC galaxy sample mocks (black dashed line).

In the middle panel, we display the power spectrum normalized by a linear power spectrum where the baryon acoustic oscillations have been smoothed (the red and blue lines are as in the top panel).

The error-bars correspond to the diagonal elements of the covariance and are estimated from the scatter of the mocks. The errors in the plots are therefore correlated, so a 'χ^2-by-eye' estimate would be highly misleading.

In the lower panel, we present the fractional differences between the data and the best-fitting model. The model is able to reproduce all the data points up to $k \simeq 0.20\,h\,\mathrm{Mpc}^{-1}$, within 3 per cent accuracy (indicated by the black dotted horizontal lines). The SGC sample presents an excess of power at large scales compared to the NGC sample. This feature has been also observed in different analyses of the same galaxy sample (Beutler et al. 2014; Anderson et al. 2014). It is likely that this excess of power arises from targeting systematics in the SGC galaxy catalogue. More details about this feature will be reported in the next and final Data Release of the CMASS catalogue.

Table 1. Best-fitting parameters for the combination of NGC and SGC assuming an underlying 'Planck13' Planck cosmology (see the text for details). The maximum k-vector used in the analysis is also indicated. For the $\sigma_8(z_{\rm eff})$ measurement, the parenthesis indicate the ratio to the fiducial Planck13 value. The units for $\sigma_{\rm FoG}$ are Mpch^{-1}.

$k_{\rm max} = 0.17\,h\,\mathrm{Mpc}^{-1}$	b_1	b_2	$f(z_{\rm eff})$	$\sigma_8(z_{\rm eff})$ $(/\sigma_8^{\rm Planck13})$	$\sigma^P_{\rm FoG}$	$\sigma^B_{\rm FoG}$	$A_{\rm noise}$
NGC	2.214	1.274	0.991	0.544 (0.857)	5.748	17.881	−0.319
SGC	1.838	0.677	0.517	0.694 (1.094)	4.636	8.873	0.102
NGC + SGC	2.086	0.902	0.763	0.597 (0.941)	5.843	15.397	−0.214

Table 2. Best-fitting parameters for NGC, SGC and combination (NGC+SGC) for Planck13 cosmology. The maximum scale is set to $k_{\rm max} = 0.17\,h^{-1}$ Mpc. The units for $\sigma_{\rm FoG}$ are Mpc h^{-1}.

$k_{\rm max} = 0.17\,h\,{\rm Mpc}^{-1}$	${b_1}^{1.40}\sigma_8(z_{\rm eff})$	${b_2}^{0.30}\sigma_8(z_{\rm eff})$	$A_{\rm noise}$	$\sigma^B_{\rm FoG}$	$\sigma^P_{\rm FoG}$	$f^{0.43}(z_{\rm eff})\sigma_8(z_{\rm eff})$
NGC	1.655 ± 0.071	0.585 ± 0.094	-0.32 ± 0.27	17 ± 13	5.7 ± 1.9	$0.541 \pm 0.092 + 0.05$
SGC	1.63 ± 0.10	0.62 ± 0.15	0.10 ± 0.32	8 ± 19	4.6 ± 3.0	$0.52 \pm 0.12 + 0.05$
NGC + SGC	1.672 ± 0.060	0.579 ± 0.082	-0.21 ± 0.24	15 ± 12	5.8 ± 1.8	$0.532 \pm 0.080 + 0.05$

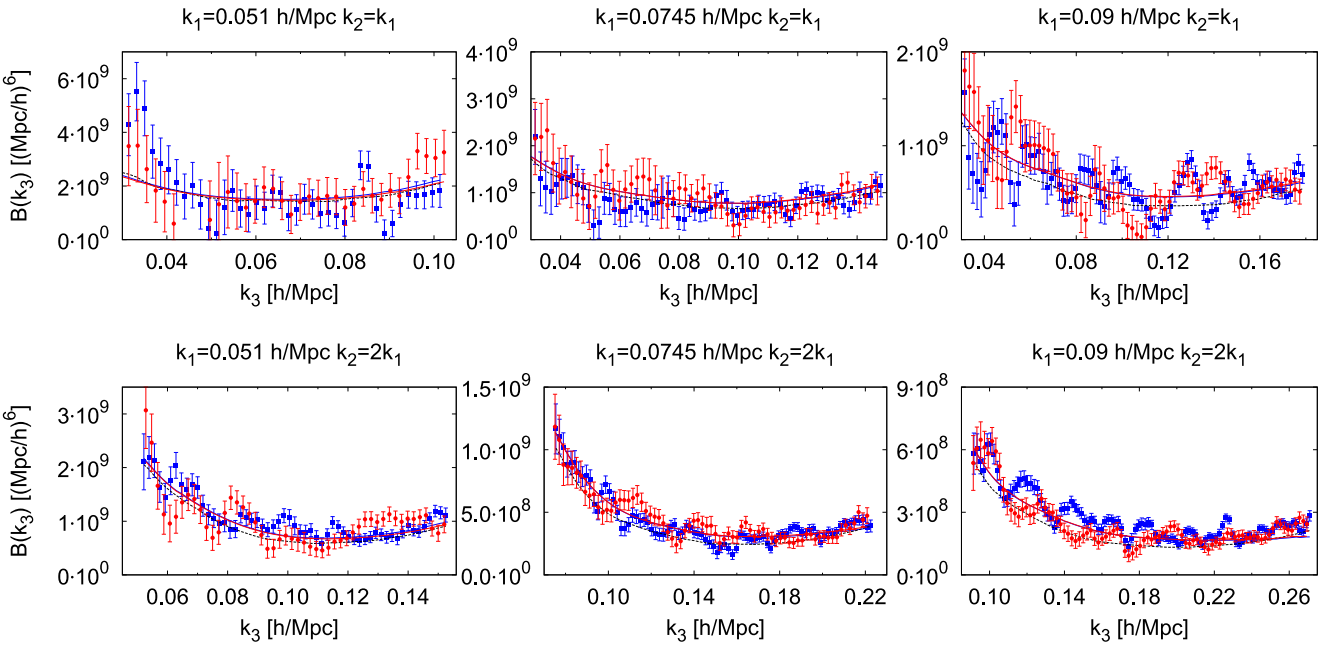

Figure 2. Bispectrum data for NGC (blue squares) and SGC (red circles) with the best-fitting models (red and blue lines) listed in Table 1 as a function of k_3 for given k_1 and k_2. Blue lines take into account the effects of the NGC mask, and red lines for SGC mask. For reference the (mean) bispectrum of the mock galaxy catalogues are shown by the black dashed lines. Different panels show different scales and shapes. The first row corresponds to triangles with $k_1 = k_2$ whereas the second row to $k_1 = 2k_2$. Left-hand column plots correspond to $k_1 = 0.051\,h\,{\rm Mpc}^{-1}$, middle column to $k_1 = 0.0745\,h\,{\rm Mpc}^{-1}$ and the right-hand column to $k_1 = 0.09\,h\,{\rm Mpc}^{-1}$. The model is able to describe the observed bispectrum for $k_3 \lesssim 0.20\,h\,{\rm Mpc}^{-1}$.

The differences between the parameters corresponding to NGC, SGC and NGC+SGC observed in Table 1 are due to degeneracies introduced among the parameters. These degeneracies are fully described in Section 4.1. We do not display errors on these parameters because we do not consider to estimate them using the mocks, since their distribution is highly non-Gaussian. It is only when we use a suitable parameter combination (in Table 2) that the distribution looks more Gaussian and it makes sense to associate an error-bar to them.

The six panels of Fig. 2 show the measured CMASS DR11 bispectrum for different scales and shapes for the NGC (blue) and SGC (red) galaxy samples. The best-fitting model to the NGC+SGC of Table 1 (also used in Fig. 1), is indicated with the same colour notation. The average of the 600 NGC galaxy mocks is shown by the black dashed line. It is not surprising that the mocks are a worse fit to the bispectrum than the analytic prescription for the best-fitting parameters; in fact the mocks have a slightly different cosmology and bias parameters compared to the best fit to the data.

Errors and data points are highly correlated, especially those for modes with triangles that share two sides. Consequently, the oscillations observed in the different bispectra panels are entirely due to the sample variance effect; in fact there is no correspondence for the location of these features between NGC and SGC.

Historically, the bispectrum has been plotted as the hierarchical amplitude $Q(\theta)$ given a ratio k_1/k_2 (see e.g. Fry 1994) defined as

$$Q(\theta_{12}|k_1/k_2) = \frac{B(k_1,k_2,k_3)}{P(k_1)P(k_2)+P(k_2)P(k_3)+P(k_1)P(k_3)}, \tag{32}$$

where θ_{12} is the angle between the two k-vectors $\boldsymbol{k}_1$ and $\boldsymbol{k}_2$. In tree-level perturbation theory and for a power-law power spectrum this quantity is independent of overall scale k and of time.[5] In practice, this is not the case (the power spectrum is not a power law and the leading order description in perturbation theory must be enhanced even to work at scales $k \lesssim 0.2$). For ease of comparison with previous literature present a figure of $Q(\theta)$ in Fig. 3. This figure does not have any information not contained in Fig. 2.

[5] We are working with monopole quantities, so the bispectra and power spectra in equation (32) are the corresponding monopoles B^0 and P^0.

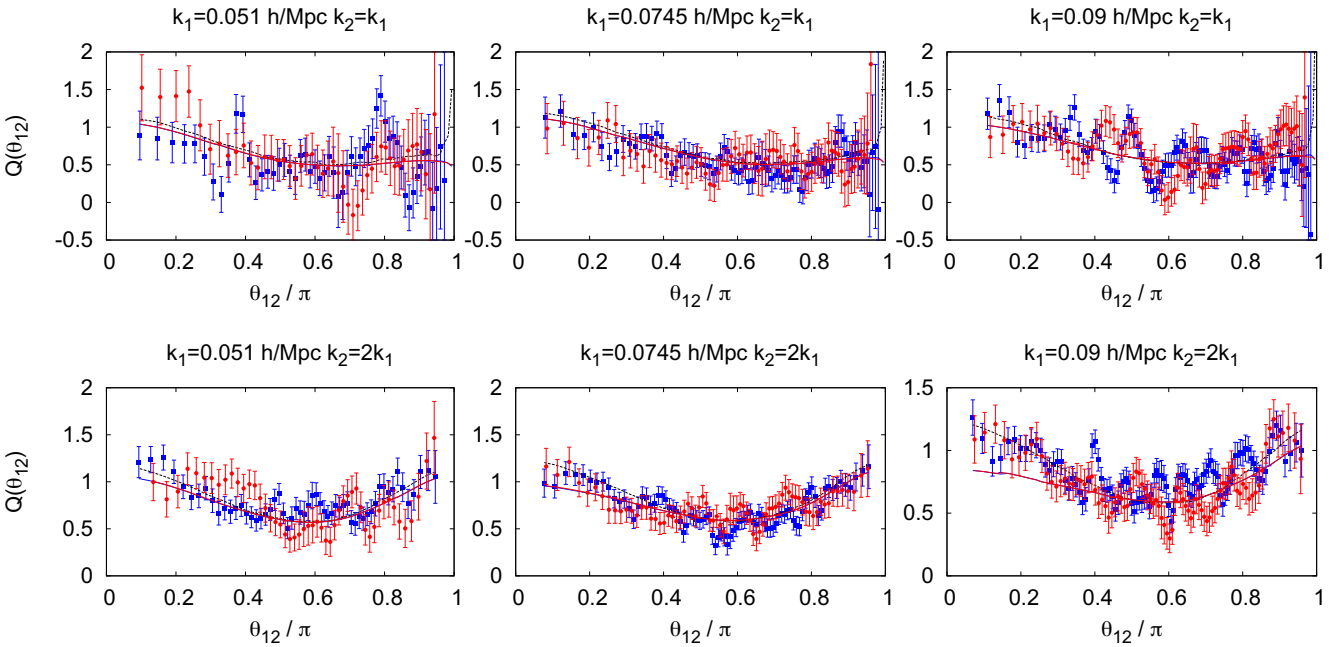

Figure 3. Reduced bispectrum for DR11 CMASS data (symbols with errors) and the corresponding model (red and blue lines) for different scales and shapes. Same notation to that in Fig. 2. The model is able to describe the characteristic 'U-shape' for scales where $k_i \lesssim 0.20\,h\,\mathrm{Mpc}^{-1}$.

Gravitational instability predicts a characteristic 'U-shape' for $Q(\theta)$ when $k_i/k_j = 2$, but non-linear evolution and non-linear bias erase this dependence on configuration. Figs 2 and 3 possess the characteristic shape at high statistical significance. It is also interesting that for large k (in particular large k_1 and $k_2/k_1 = 2$ and θ_{12} small, therefore k_3 nearing $k_1 + k_2$), we see the breakdown of our prescription. The theoretical predictions that produce the blue and red lines, the power spectra in the denominator of $Q(\theta_{12})$ are computed using 2L-RPT and the prescription of Section 3.5. The average of the mocks is a closer match (despite the different cosmology) because non-linearities are better captured.

4.1 Bias and growth factor measurements

Despite the model depending on four cosmological parameters, the data can only constrain three (cosmologically interesting) quantities; there are large degeneracies among these parameters, in particular involving σ_8. Under the reasonable assumption that the distribution of the best-fitting parameters from each of the 600 mocks is a good approximation to the likelihood surface, there are non-linear degeneracies in the parameters space of b_1, b_2, f and σ_8 as shown in the left-hand panel of Fig. 4 (and also in Fig. 17). These non-linear degeneracies can be reduced (i.e. the parameter degeneracies can be made as similar as possible to a multivariate Gaussian distribution) by a simple re-parametrization. In particular, we will use $\log_{10}b_1$, $\log_{10}b_2$, $\log_{10}f$, $\log_{10}\sigma_8$, which, when computing marginalized confidence intervals on the parameters, is equivalent to assuming uniform priors on these parameters. Conveniently, this coincides with Jeffrey's non-informative prior. We can adopt this procedure because b_1, σ_8 and f are positive definite quantities and b_2 is positive for CMASS galaxies and for the mocks. This issue is explored in detail in Section 5.5.3. Because of these degeneracies, we combine the four cosmological parameters into three new variables: $b_1^{1.40}\sigma_8$, $b_2^{0.30}\sigma_8$ and $f^{0.43}\sigma_8$ (indicated by the dashed green lines in Fig. 4). This combination is formed *after* the fitting process and therefore the (multidimensional) best-fitting values for b_1, b_2, f and σ_8 are not affected by the definition of the new variables. In the new variables, the parameter distribution is more Gaussian and the errors can be easily estimated from the mocks.

In the left-hand panel of Fig. 4, we show the distribution of CMASS DR11 NGC best fits from the galaxy mocks (blue points) for $\log_{10}b_1$, $\log_{10}b_2$, $\log_{10}f$ and $\log\sigma_8$. The red crosses indicate the best-fitting values obtained from the CMASS DR11 NGC+SGC data set. The orange contours enclose 68 per cent of marginalized posterior when we consider the distribution of mocks as a sample of the posterior distribution of the parameters. The best-fitting parameters have been displaced in log -space by a constant offset in order to match the centre of the 68 per cent contour and the measured data points. This allows use of the mocks to see the likely degeneracies around the data best-fitting values. Black and red dashed lines show the fiducial values for f and σ_8 for mocks and data, respectively. The green dashed lines indicate the empirical relation between σ_8 and the other variables. These empirical relations correspond to power law relations in linear space, and the slope of these lines is not affected by the shift of the mocks, as it is done in log -space. In particular, we have found that these empirical relations correspond to $f^{-0.43} \sim \sigma_8$, $b_1^{-1.40} \sim \sigma_8$ and $b_2^{-0.30} \sim \sigma_8$. In the right-hand panel of Fig. 4, we present the same distribution that in the right-hand panel but for the combined set of variables, $f^{0.43}\sigma_8$, $b_1^{1.40}\sigma_8$ and $b_2^{0.30}\sigma_8$. The distribution of results from the galaxy mocks are closer to a multivariate Gaussian distribution in these new set of variables than in the original set.

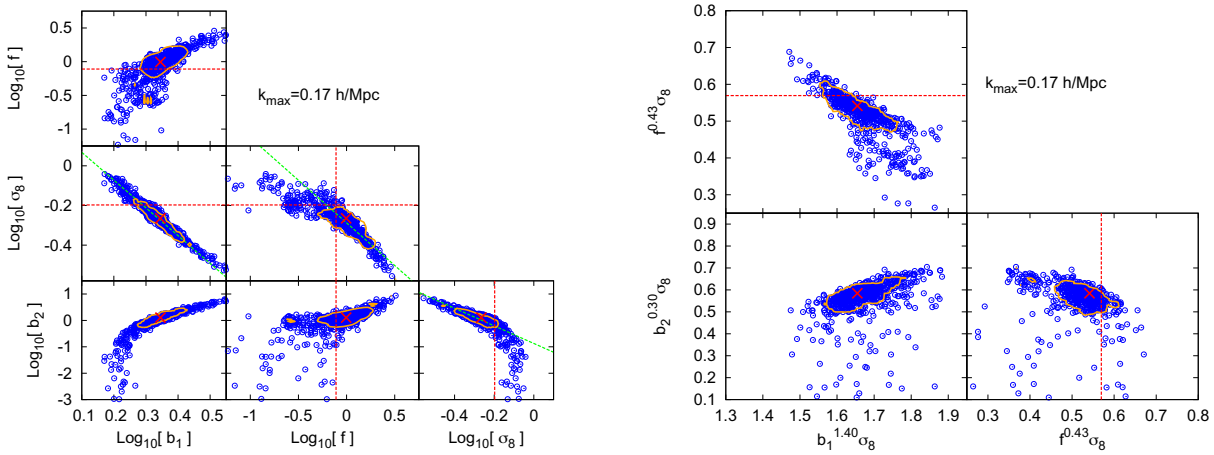

Figure 4. Two-dimensional distributions of the parameters of (cosmological) interest. Left-hand panels: we use $\log_{10}b_1$, $\log_{10}b_2$, $\log_{10}f$, $\log_{10}\sigma_8$ to obtain simpler degeneracies. The blue points represent the best fit of the 600 NGC mock catalogues and the red cross is the best fit from the data. The mocks distributions of points have been displaced in the $\log_{10}$ space to be centred on the best fit for the NGC data. If we consider the distribution of the mocks as a sample of the posterior distribution of the parameters, the orange contour lines enclose 68 per cent of the marginalized posterior. The green dashed lines represent the linearized direction of the degeneracy in parameter space in the region around the maximum of the distribution. The dashed red lines indicate the Planck13 cosmology. Right-hand panels: same notation as the left-hand panels but for the best constrained combination of parameters. The distributions appear more Gaussian than in the original variables.

Table 2 lists the best-fitting values and the errors for these new variables. The data used are always the DR11 CMASS galaxies monopole power spectrum and bispectrum when the Planck13 cosmology is assumed. The first two rows correspond to the NGC and SGC galaxy sample, respectively, whereas in the third row both samples are combined. For the three cases, the maximum scale is conservatively set to $k_{\rm max} = 0.17\,h\,{\rm Mpc}^{-1}$. A smaller $k_{\rm max}$ would yield too large error-bars, but at larger k non-linearities become important and we have evidence that our modelling starts breaking down. This issue is further discussed in Section 4.2, where we study the dependence of the best-fitting parameters with $k_{\rm max}$ and the choice motivated in details in Section 5.

The best-fitting $f^{0.43}\sigma_8$ is provided along with a systematic error-component, in addition to the statistical error. In Section 5.6, we present a full description of how this systematic error is obtained. In brief, we have indications that the model used for describing the power spectrum and bispectrum of *biased* tracers in redshift space presents a systematic and scale-independent underestimate of $f^{0.43}\sigma_8$ at the level of 0.05. The determination of this systematic error relies on the analysis of N-body haloes as well as mock galaxy catalogues. It is interesting that the systematic correction would cancel if we considered instead the quantity $f\sigma_8$ (Gil-Marín et al. 2014b); we will discuss this point in Section 5.6.

From the results in Table 2, we do not detect any strong tension between NGC and SGC for any of the parameters. We only observe a non-statistically significant trend $A_{\rm noise}$; the NGC galaxy sample tends to have a slightly sub-Poisson shot noise, whereas the SGC sample presents a slightly super-Poisson shot noise. However, these differences are not statistically significant and can be explained by a sample variance effect.

We understand that the parametrization $f^{0.43}\sigma_8$ is non-standard, although is the one that naturally arises from the shape of the parameter-space. In order to make a connection with the commonly estimated $f\sigma_8$, we can assume a value for f predicted for a standard ΛCDM model with parameters set by the *Planck* (Planck Collaboration XVI 2014) $f_{\rm Planck} = 0.777$ (as listed in Table 4), we can construct our estimator of $f\sigma_8$ as, $[f\sigma_8]_{\rm est.} \equiv [f^{0.43}\sigma_8] f_{\rm Planck}^{0.57}$. From the values of $f^{0.43}\sigma_8$ for NGC+SGC in Table 2, we obtain that $[f\sigma_8]_{\rm est.} = 0.504 \pm 0.069$. This result is in very good agreement with the prediction from *Planck*, $[f\sigma_8]_{\rm Planck} = 0.493$, with only 2 per cent offset.

4.2 Dependence on the maximum *k*

In the two panels of Fig. 5, we present the effect of varying the maximum k (smallest scale) included, $k_{\rm max}$. The left-hand panel displays the variation of $b_1^{1.40}\sigma_8$, $b_2^{0.30}\sigma_8$ and $f^{0.43}\sigma_8$ as function of $k_{\rm max}$, while the right-hand panel shows $A_{\rm noise}$, $\sigma^P_{\rm FoG}$ and $\sigma^B_{\rm FoG}$ as function of $k_{\rm max}$. The plotted values for the $f^{0.43}\sigma_8$ quantity have been corrected by the systematic offset of 0.05 as described in Section 5.6. The different colour lines correspond to the galaxy catalogue used to perform the analysis: blue lines for the NGC, red lines for the SGC and black lines when the catalogues are combined.

The three galaxy samples yield consistent quantities for all values of $k_{\rm max}$; there is no indication of a breakdown of the model (i.e. abrupt changes in the recovered parameters values when too small scales are included).

Extensive tests (see Section 5) indicate that, at least for N-body simulations and mock catalogues, the modelling adopted here starts to break down beyond $k = 0.17\,h\,{\rm Mpc}^{-1}$ for biased tracers in redshift space. However, we have checked that for $0.20 \leq k\,[h\,{\rm Mpc}^{-1}] \leq 0.17$, the modelling is still able to reproduce N-body simulations and mocks catalogues up to a few per cent accuracy. Because of this, we adopt a conservative approach, where we stop our analysis at $k_{\rm max} = 0.17\,h\,{\rm Mpc}^{-1}$, and a less conservative approach, where we push the analysis up to $k_{\rm max} = 0.20\,h\,{\rm Mpc}^{-1}$. In both cases, we add in quadrature a systematic contribution to the statistical error, $\sigma_{\rm sys}$, which we chose to be

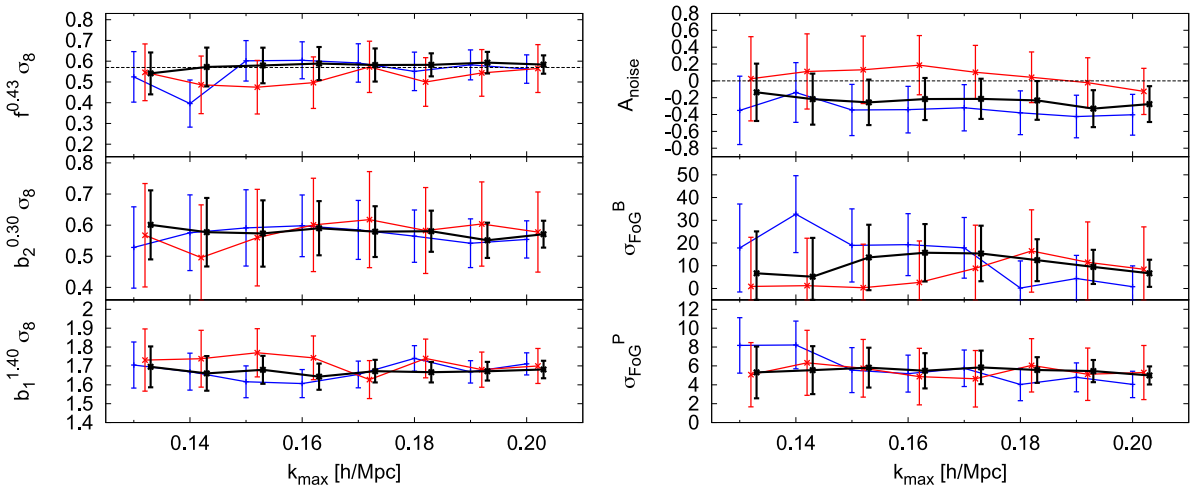

Figure 5. Best-fitting parameters as a function of k_{max} for NGC data (blue symbols), SGC data (red symbols) and a combination of both (black symbols) when the Planck13 cosmology is assumed. The quantity $f^{0.43}\sigma_8$ has been corrected by the systematic error as is listed in Table 2. For the $f^{0.43}\sigma_8$ panel, the corresponding fiducial values for GR are plotted in dashed black line. In the A_{noise} panel, the dotted line indicates no deviations from Poisson shot noise. The units of σ_{FoG} are Mpc h^{-1}. There is no apparent dependence with k_{max} for any of the displayed parameters for $k_{max} \leq 0.17\,h\,\mathrm{Mpc}^{-1}$.

Table 3. Best-fitting parameters for (NGC+SGC) for Planck13 cosmology for different k_{max}. This table corresponds to the black line of Fig. 5. The units for σ_{FoG} are Mpc h^{-1}. In the last column, a total error is given by $\sigma_{tot} \equiv \sqrt{\sigma_{est}^2 + [\sigma_{sys}/2]^2}$.

k_{max} [$h\,\mathrm{Mpc}^{-1}$]	${b_1}^{1.40}\sigma_8(z_{eff})$	${b_2}^{0.30}\sigma_8(z_{eff})$	A_{noise}	σ_{FoG}^B	σ_{FoG}^P	$f^{0.43}(z_{eff})\sigma_8(z_{eff}) \pm \sigma_{est} + \sigma_{sys}\,(\pm\sigma_{tot})$
0.13	1.69 ± 0.11	0.60 ± 0.11	-0.14 ± 0.34	7 ± 18	5.3 ± 2.7	$0.49 \pm 0.10 + 0.05\,(\pm 0.10)$
0.14	1.660 ± 0.091	0.58 ± 0.11	-0.22 ± 0.30	5 ± 17	5.6 ± 2.5	$0.522 \pm 0.094 + 0.05\,(\pm 0.097)$
0.15	1.679 ± 0.074	0.57 ± 0.11	-0.26 ± 0.27	14 ± 14	5.8 ± 2.1	$0.529 \pm 0.086 + 0.05\,(\pm 0.090)$
0.16	1.643 ± 0.069	0.590 ± 0.087	-0.22 ± 0.25	16 ± 13	5.5 ± 1.9	$0.538 \pm 0.080 + 0.05\,(\pm 0.084)$
0.17	1.672 ± 0.060	0.579 ± 0.082	-0.21 ± 0.24	15 ± 12	5.8 ± 1.8	$0.532 \pm 0.080 + 0.05\,(\pm 0.084)$
0.18	1.667 ± 0.054	0.580 ± 0.066	-0.23 ± 0.23	12.4 ± 9.2	5.7 ± 1.3	$0.532 \pm 0.055 + 0.05\,(\pm 0.060)$
0.19	1.672 ± 0.049	0.551 ± 0.057	-0.33 ± 0.22	9.5 ± 7.5	5.4 ± 1.2	$0.543 \pm 0.052 + 0.05\,(\pm 0.058)$
0.20	1.681 ± 0.046	0.571 ± 0.043	-0.28 ± 0.21	6.7 ± 6.0	4.99 ± 0.96	$0.534 \pm 0.044 + 0.05\,(\pm 0.051)$

50 per cent of the systematic shift, σ_{sys}. Therefore, in both cases the total error is given by $\sigma_{tot} \equiv \sqrt{\sigma_{est}^2 + [\sigma_{sys}/2]^2}$. For completeness, in Table 3 we report results as function of k_{max} as they are plotted in Fig. 5.

4.3 Dependence on the assumed cosmology

In the analysis of the CMASS DR11 data in the above section we have assumed the *Planck* cosmology (Planck13). This assumption is necessary to obtain the linear power spectrum which is the starting point for the galaxy power spectrum and bispectrum theoretical models. Since the results presented in Table 2 and Fig. 5 may be sensitive to the assumed cosmological parameters, in this section we repeat the analysis for the NGC galaxy sample assuming two variations of the Planck13 cosmology. We aim at quantifying how sensitive the parameter set $\{{b_1}^{1.40}\sigma_8,\ {b_2}^{0.30}\sigma_8,\ f^{0.43}\sigma_8,\ A_{noise},\ \sigma_{FoG}^P,\ \sigma_{FoG}^B\}$ is to the cosmological model assumed.

Table 4 presents the cosmological parameters for the Planck13 cosmology, assumed in Section 4.1, and present two additional Planck-like cosmologies sets, namely L-Planck13 and H-Planck13. These sets of parameters are generated using the uncertainties of Planck13 parameters reported in Planck Collaboration XVI (2014). The L-Planck13 cosmology has most parameters lowered by 1σ respect to Planck13, whereas for the H-Planck13 cosmology most of the parameters have been increased by 1σ. These cosmologies would be highly disfavoured by Planck data. We also include the cosmology of the mocks for comparison reasons. The definition of the parameters listed on Table 4 can be found in table 1 of Planck Collaboration XVI (2014). The parameters $\Omega_b h^2$, $\Omega_c h^2$, τ, A_s, n_s and h are the 'input parameters', whereas σ_8, D_+, f, Ω_m and $f^{0.43}\sigma_8$ are derived from those. We use the CAMB software (Lewis & Bridle 2002) to generate the linear dark matter power spectrum, P_{lin}, from each cosmological parameter set.

Fig. 6 displays the linear dark matter power spectrum of the Planck13, H-Planck13 and L-Planck13 cosmologies normalized by the power spectrum for the mocks cosmology in order to visualize the differences. The main changes are due to the parameter A_s, which regulates the amplitude of the linear power spectrum. However, since in the analysis of the data we always recover the parameters in combination with σ_8, we do not expect the results to depend on the choice of A_s. We also observe that the differences in the wiggles pattern among the Planck

Table 4. Parameters for the different cosmology models tested in this paper for the analysis of CMASS data: Planck13, L-Planck13 and H-Planck13. The mocks cosmology is shown as a reference.

	Mocks	Planck13	H-Planck13	L-Planck13
$\Omega_b h^2$	0.0196	0.022 068	0.0224	0.021 74
$\Omega_c h^2$	0.114 66	0.120 29	0.1165	0.1227
τ	0.091 23	0.0925	0.135	0.059
$10^9 A_s$	1.9946	2.215	2.39	2.07
n_s	0.95	0.9624	0.971	0.9522
h	0.70	0.6711	0.688	0.660
$\sigma_8(z=0)$	0.80	0.8475	0.8680	0.8252
$\sigma_8(z_{\rm eff})$	0.6096	0.6348	0.6564	0.6149
$f(z_{\rm eff})$	0.744	0.777	0.760	0.788
Ω_m	0.274	0.316	0.293	0.332
$f^{0.43}(z_{\rm eff})\sigma_8(z_{\rm eff})$	0.537	0.570	0.583	0.555

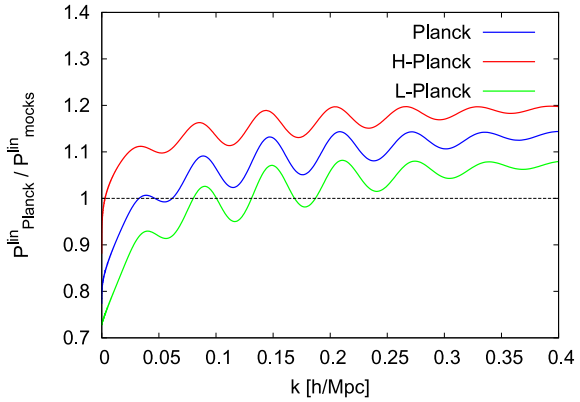

Figure 6. Linear power spectrum of Planck13 cosmology (blue line), H-Planck13 cosmology (red line) and L-Planck13 cosmology (green line). All the power spectra have been normalized by the mock linear power spectrum for clarity. The main difference between the Planck cosmologies relies on the amplitude, whereas for the mocks cosmology the BAO oscillations also present a different pattern. The details of these different cosmologies can be found in Table 4.

Table 5. Best-fitting parameters to CMASS DR11 NGC galaxy sample for four different underlying cosmologies: Planck13, L-Planck13, H-Planck13 and Mocks. The maximum scale is set to $k_{\rm max} = 0.17\,h\,{\rm Mpc}^{-1}$. The units for $\sigma^{(i)}_{\rm FoG}$ are Mpc h^{-1}.

$k_{\rm max} = 0.17\,h\,{\rm Mpc}^{-1}$	$b_1{}^{1.40}\sigma_8(z_{\rm eff})$	$b_2{}^{0.30}\sigma_8(z_{\rm eff})$	$A_{\rm noise}$	$\sigma^B_{\rm FoG}$	$\sigma^P_{\rm FoG}$	$f^{0.43}(z_{\rm eff})\sigma_8(z_{\rm eff})$
Planck13	1.655 ± 0.071	0.585 ± 0.094	-0.32 ± 0.27	17 ± 13	5.7 ± 1.9	$0.541 \pm 0.092 + 0.05$
H-Planck13	1.805 ± 0.071	0.579 ± 0.095	-0.41 ± 0.27	9 ± 13	3.9 ± 1.9	$0.526 \pm 0.092 + 0.05$
L-Planck13	1.572 ± 0.071	0.560 ± 0.095	-0.33 ± 0.27	18 ± 13	5.7 ± 1.9	$0.529 \pm 0.092 + 0.05$
Mocks	1.708 ± 0.071	0.533 ± 0.095	-0.50 ± 0.27	8 ± 13	3.9 ± 1.9	$0.493 \pm 0.092 + 0.05$

cosmologies are small. On the range of scales considered for our analysis the effect of other parameters, which change the broad-band shape of the power spectrum such as such as n_s, is small.

Table 5 lists the best-fitting parameters obtained from analysing the power spectrum and bispectrum monopoles from the DR11 CMASS NGC galaxy sample when four different cosmologies are assumed: Planck13, H-Planck, L-Planck and Mocks. As in Table 2, the maximum scale for the fit has been set to $0.17\,h\,{\rm Mpc}^{-1}$. Considering the relatively large changes in the input cosmological parameters, we do not observe any significant variation for most of the estimated parameters (shifts compared to the fiducial cosmology are typically $\lesssim 0.5\sigma$). The most sensitive parameter to the cosmology is $b_1^{1.40}\sigma_8$, which changes $\simeq 1\sigma$ at $k_{\rm max} \leq 0.17\,h\,{\rm Mpc}^{-1}$. On the other hand, the $f^{0.43}\sigma_8$ parameter does not present any significant trend within the cosmologies explored in this paper. Since we assume that the errors do not depend with cosmology, they are the same for all three cosmologies.

Fig. 7 displays how the best-fitting parameters depend on the maximum scale for the four cosmologies: Planck13 (blue lines), H-Planck (red lines), L-Planck (green lines) and Mocks (black lines). Dashed lines show the GR prediction for $f^{0.43}\sigma_8$ when a particular cosmological model is assumed.

We conclude that there is no need to increase the errors estimated form the mocks on the quantity $f^{0.43}\sigma_8$ to account for uncertainty in the cosmological parameters.

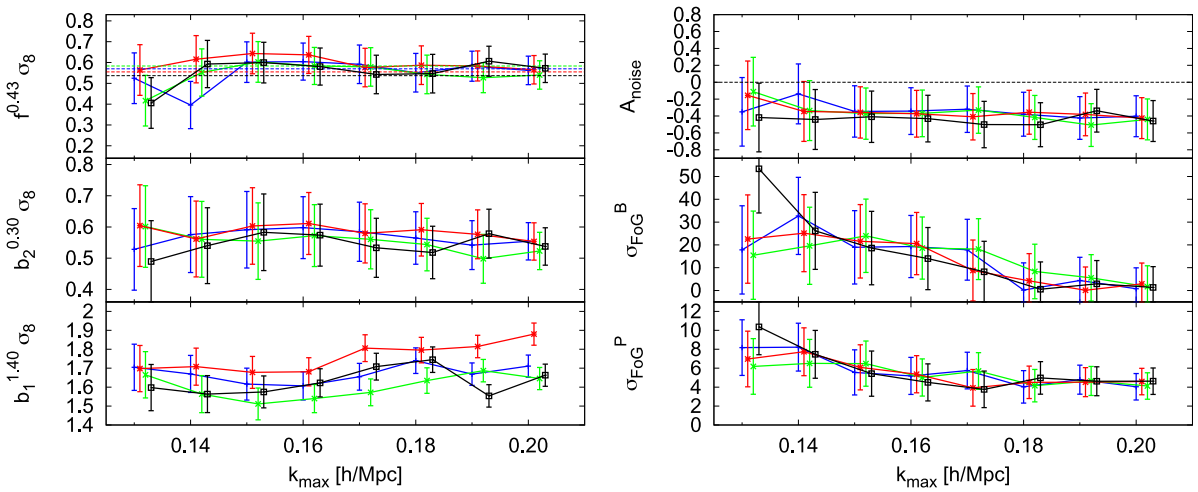

Figure 7. Best-fitting parameters as a function of $k_{\rm max}$ for NGC data assuming different cosmologies (listed in Table 4): Planck13 (blue symbols), L-Planck13 (green symbols), H-Planck13 (red symbols) and Mocks (black symbols). The quantity $f^{0.43}\sigma_8$ has been corrected by the systematic error as is listed in Table 2. For the $f^{0.43}\sigma_8$ panel, the corresponding fiducial values for GR are shown by dashed lines for the corresponding cosmology model. There is no apparent dependence with $k_{\rm max}$ for any of the displayed parameters for $k_{\rm max} \leq 0.17\,h\,{\rm Mpc}^{-1}$.

5 TESTS ON *N*-BODY SIMULATIONS AND SURVEY MOCK CATALOGUES

We have performed extensive tests to check for systematic errors induced by our method and to assess the performance of the different approximations we had to introduce. In particular, we have tested the power spectrum and bispectrum modelling on dark matter particles, haloes and mock galaxy catalogues. We also quantify the effects of the survey geometry and our approximation of these to match the FKP-estimator derived results.

5.1 Tests on *N*-body dark matter particles

In order to test the effect of our choice of triangle shapes on the best-fitting values and errors, we focus first on the simpler and cleaner case of dark matter simulations.

As described in Section 3.6, in the analysis of this paper we have chosen to use a subset of triangles where one of the ratios between two sides is fixed to equal $k_2/k_1 = 1$ or $k_2/k_1 = 2$. By doing so, we are discarding information contained in the triangle shapes we do not use, but analytically estimating exactly how this affects the errors is difficult since different triangles are in general correlated. Our kernel was calibrated on a slightly more extended set of shapes (see Gil-Marín et al. 2012a, 2014b) by reducing the average differences from the simulations; this decision could hide subtle cancellations that do not hold as well when only a subset of shapes is considered. Thus, we need to check for possible shifts in the parameter estimates.

One may instead choose to use all possible triangle configurations, varying all the three sides of the triangles with a step equal to the fundamental mode of the survey and imposing only that they form a closed triangle. This approach of course requires significantly more computational power, especially since our estimate of the errors is done by analysing on hundreds of mocks, but it is, in principle, possible. When using all shapes, one must extrapolate and interpolate the effective bispectrum kernel beyond the shapes for which it was calibrated, and this can induce a systematic error.

In order to tackle this issue, we apply our analysis to the simple case of dark matter in real space, for which we know that by definition $b_1 = 1$ and $b_2 = 0$, without complications due to halo bias, survey window etc. We use 60 *N*-body simulations among those used in Gil-Marín et al. (2012a) for an effective volume that is about 140 times larger than that of the survey. Using only bispectrum measurements, we find that there is no significant bias in b_1 using either the two selected shapes or all shapes. For b_2, we find a hint of a possible $+0.05$ bias which is, however, at the 1.5σ level and thus completely negligible for our data set. Using all shapes leads to reduced error-bars. This result is shown in the left-hand panel of Fig. 8.

The fractional difference in the errors indicates there is roughly a factor 2 improvement in using all the configurations.

In the right-hand panel of Fig. 8, we compare the errors obtained with a simple Fisher matrix estimate (following Scoccimarro et al. 1998 appendix A2 and Gil-Marín et al. 2012a equation A3). This figure indicates that that one can take the – band-power – bispectra to have a Gaussian distribution for this volume and for the binning adopted here.

These findings demonstrate that in principle the statistical errors could be reduced by using more shapes. This approach, however, will not be implemented here for several reasons: (i) it is computationally extremely challenging (ii) it requires an extrapolation/interpolation of kernels that have been calibrated on a subset of shapes. This extrapolation works fine for real space but its effectiveness has not been explored in redshift space (iii) most importantly, in the present analysis, systematic errors are kept (just) below the statistical errors, so the full benefit of shrinking the statistical errors will not be realized.

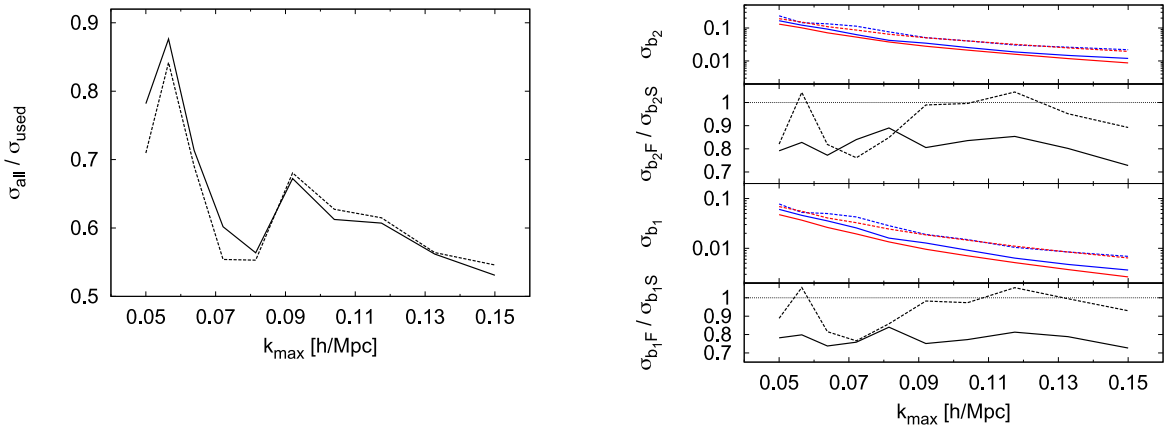

Figure 8. Left-hand panel: ratio between errors obtained using all possible triangles and only $k_2/k_1 = 1, 2$ triangles. The solid line is for b_1 and dashed line is for b_2. Errors are computed from the scatter of 60 realizations of dark matter. Right-hand panel: red lines correspond to the predictions of the errors of b_1 and b_2 using Fisher analysis, whereas blue lines when these errors are predicted from the scatter of best-fitting values of different realizations. Black lines correspond to the ratio between Fisher predictions (subscript F) and scatter predictions (subscript S). Solid lines are the predictions when all the possible triangles are used, whereas dashed lines are for triangles with $k_2/k_1 = 1, 2$. These plots indicate that the statistical errors could potentially be reduced by using more shapes, although by doing this, the systematic effects would dominate the results and the full benefit of shrinking the statistical errors will not be realized.

5.2 *N*-body haloes versus PTHALOS in real space and redshift space

The mock galaxy catalogues are based on PTHALOS, which only provides an approximation to fully non-linear dark matter halo distributions. Here, we check the differences at the level of the power spectrum and bispectrum between *N*-body haloes and PTHALOS.

PTHALOS and *N*-body haloes simulations (Section 2.2) have the same underlying cosmology, but different mass resolutions. The large scale power spectrum is therefore different for the two catalogues (there is a relative bias) because the minimum mass of the resolved haloes is not identical. However, since the definition of halo cannot be the same for both (see Manera et al. 2013 for a complete discussion on the differences between *N*-body-halo and PTHALOS mass), setting the mass threshold to be the same for the two catalogues does not completely solve this problem.

Therefore, we choose the minimum mass of the *N*-body catalogues so that the resulting halo power spectrum matches the amplitude of PTHALOS power spectrum at large scales in real space. This occurs at $\log_{10}(M_{\rm min}[{\rm M}_\odot\, h^{-1}]) = 12.892$ where for the PTHALOS catalogue the minimum mass is $\log_{10}(M_{\rm min}[{\rm M}_\odot\, h^{-1}]) = 12.700$. The PTHALOS mass we report, is the sum of the masses of the particles that form each PTHALO. Hence, this is the halo mass *before* the re-assignment and should not be confused with the re-assigned mass that matches the mass function from *N*-body haloes.

Fig. 9 presents the comparison between *N*-body haloes (red lines) and PTHALOS (blue lines). The top-left panel shows the comparison between the power spectra in real space (normalized by the non-linear matter power spectrum prediction for clarity) and the others of the panels display the comparison between different shapes of the bispectrum in real space (also normalized by the non-linear matter prediction): equilateral triangles, $k_2/k_1 = 1$ and $k_2/k_1 = 2$ triangles, as indicated in each panel. In all the panels, the symbols represent the mean value among 50 realizations for PTHALOS and 20 realizations for *N*-body haloes. The errors-bars correspond to the error of the mean. The error-bars for *N*-body haloes are slightly larger due to the difference in the number of realizations ($\sqrt{(50 \times 2.4)/(20 \times 1.5)} = 2$), and therefore in the total volume. Note also that these error-bars do not take into account the uncertainty on the measurement of $P_{\rm m}$ and $B_{\rm m}$, which have been computed using five realizations, and therefore the displayed error-bars are slightly underestimated. The agreement between *N*-body haloes and PTHALOS is excellent at large scales for the power spectrum. At small scales, $k \geq 0.2\, h\,{\rm Mpc}^{-1}$, the PTHALOS power spectrum overestimates the *N*-body prediction by few per cent. The agreement is also good for the bispectrum. For the equilateral shape both *N*-body and PTHALOS agree for $k \leq 0.15\, h\,{\rm Mpc}^{-1}$. We do not go beyond this scale, given that our set of triangles with $k_1 = k_2$ are limited to $k_1 \leq 0.15\, h\,{\rm Mpc}^{-1}$, as we have mentioned in Section 3.8. Also for the scale of $k_1 = 0.1\, h\,{\rm Mpc}^{-1}$, PTHALOS reproduces the shape described by *N*-body haloes, for different values of k_2/k_1 ratio. Therefore, we conclude that PTHALOS is able to describe accurately the clustering predicted by *N*-body haloes for both the power spectrum and bispectrum up to mildly non-linear scales, typically $k_i \lesssim 0.2$ at $z = 0.55$ (recall that in deriving our main results we use $k_{\rm max} = 0.17\, h\,{\rm Mpc}^{-1}$).

The panels of Fig. 10 use the same notation as Fig. 9 showing the redshift-space monopole for the power spectrum and bispectrum. In this case, the halo mass cut for *N*-body has been set to $\log_{10}(M_{\rm min}[{\rm M}_\odot\, h^{-1}]) = 12.875$. If the mass cut were maintained to the same value than in real space, we would not have obtained a good match between *N*-body and PTHALOS. Assuming that *N*-body haloes are a better description of real haloes than PTHALOS, these discrepancies may indicate that even large-scale redshift-space distortions are not well captured by PTHALOS. However, we observe that these discrepancies can be mitigated rescaling slightly the mass cut for *N*-body halo catalogues. This does not represent any practical problem, since for the final galaxy mocks the mass cut of the mocks is calibrated with observations, i.e. in redshift space.

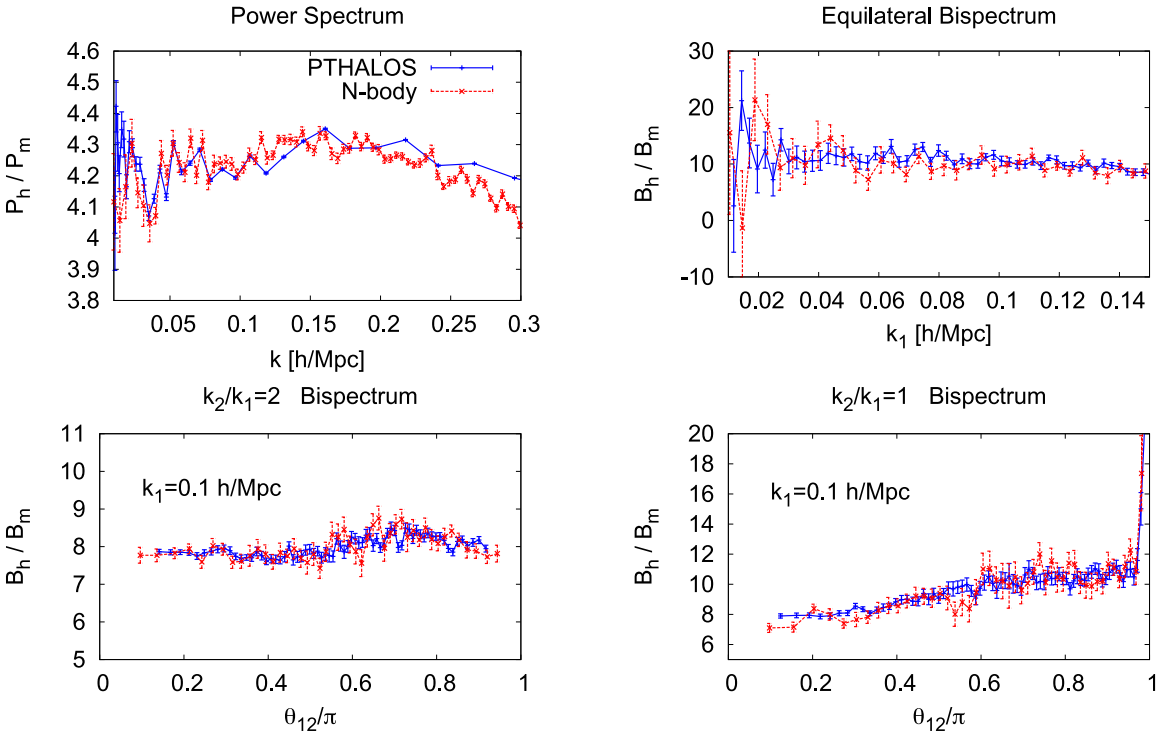

Figure 9. Power spectra (top-left panel) and bispectra (other panels) for *N*-body haloes (red lines) and PTHALOS (blue lines) both in real space normalized by $P_{\rm matter}$ and $B_{\rm matter}$, respectively. Poisson noise is assumed. There is good agreement for power spectrum and bispectrum of *N*-body haloes and PTHALOS for $k \lesssim 0.2\,h\,{\rm Mpc}^{-1}$. The halo mass cut has been $\log_{10}(M_{\rm min}[{\rm M}_\odot\,h^{-1}]) = 12.892$.

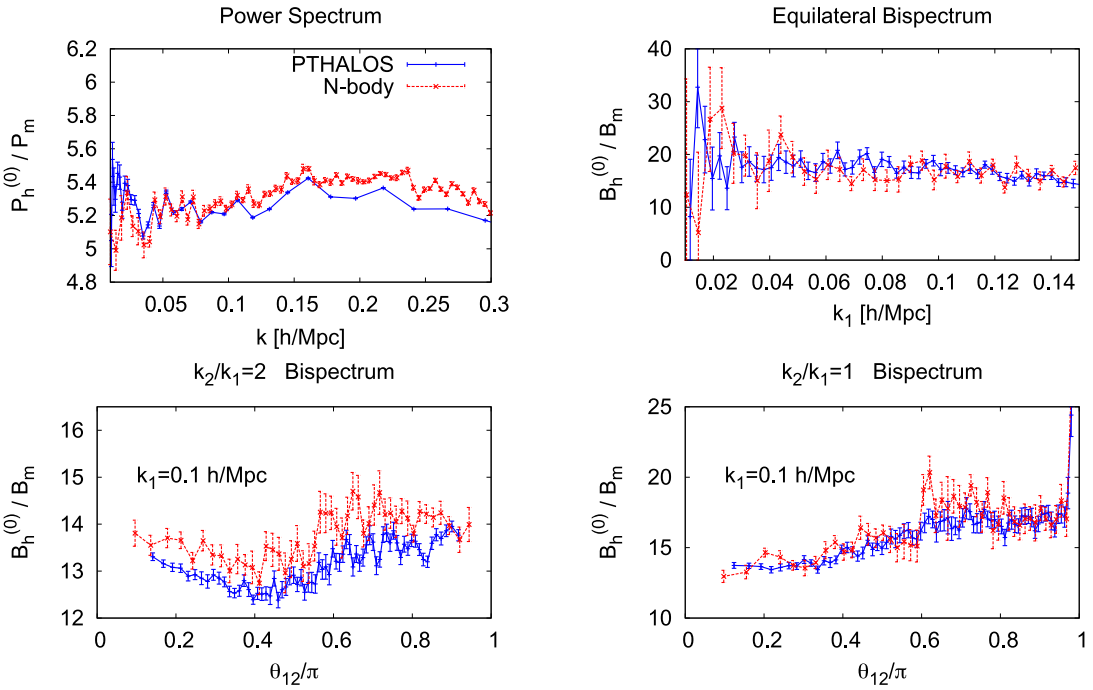

Figure 10. Same notation that in Fig. 9 but for redshift-space monopole statistics. PTHALOS tend to underestimate the monopole redshift-space quantities, and this start to be significant ($\simeq 5$ per cent deviation) for the power spectrum at $k > 0.10\,h\,{\rm Mpc}^{-1}$ and for the bispectrum shape where $k_2 = 2k_1$. The halo mass cut has been $\log_{10}(M_{\rm min}[{\rm M}_\odot\,h^{-1}]) = 12.875$.

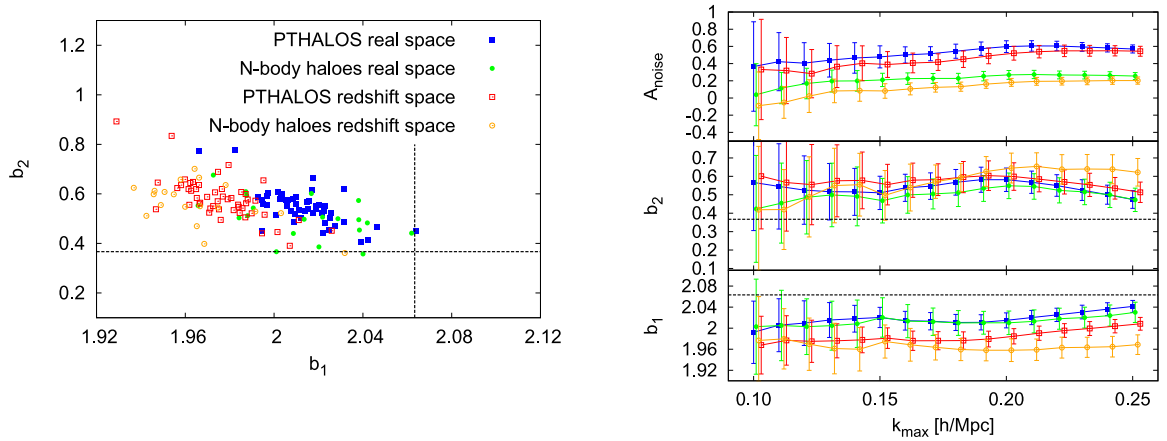

Figure 11. Left-hand panel: best-fitting bias parameters for *N*-body haloes and PTHALOS estimated from their bispectrum only. Green (blue) symbols are *N*-body haloes (PTHALOS) best-fitting values from real space bispectrum. Red (orange) symbols are *N*-body haloes (PTHALOS) best-fitting values from redshift-space monopole bispectrum. Right-hand panel: best-fitting bias parameters and shot noise amplitude as a function of $k_{\rm max}$, using the same colour notation that in left-hand panel. Error-bars correspond to the 1σ dispersion among the different realizations. In both panels, black dashed lines represent the measured cross bias parameters as they are defined in equations (33)–(34). This analysis assumes $k_{\rm max} = 0.17\,h\,{\rm Mpc}^{-1}$. There are no significant differences in the bias parameters predicted from *N*-body haloes and PTHALOS catalogues.

From the panels of Fig. 10, we observe a very good match on the power spectrum monopole for $k \leq 0.10\,h\,{\rm Mpc}^{-1}$. For large values of k the differences slightly grow, but they are always below 5 per cent. There are small differences between the bispectra of *N*-body and PTHALOS for the $k_1 = k_2 = 1$ shape. There is a significant $\sim$5 per cent offset for the $k_2/k_1 = 2$. From the plots of Fig. 10, it is not clear how these offsets can affect to the parameter estimation. In order to check this, we compare the recovered bias parameters from *N*-body and PTHALOS both in real and redshift space.

We start by estimating the bias parameters b_1 and b_2 for PTHALOS and *N*-body haloes assuming that the underlying cosmological parameters, such as σ_8 and f, are known. For simplicity (and speed), we also assume no damping term is needed for the redshift-space bispectrum monopole (i.e. equation 26 applies with $D^B_{\rm FoG} = 1$). It is well known that no FoG-like velocity dispersion is expected when considering the clustering of haloes (mapped by their centre of mass point).

In order to estimate the bias parameters, we follow the method described in Section 3, in particular Sections 3.5 and 3.6, but using only the bispectrum. For the non-linear density dark matter power spectrum needed in the bispectrum model, we use the quantity directly estimated from dark matter simulations themselves. For this analysis, we have only three parameters: b_1, b_2 and $A_{\rm noise}$.

The left-hand panel of Fig. 11 presents the best-fitting bias parameters, b_1 and b_2, for the 20 (50) different realizations for *N*-body haloes (PTHALOS) using the bispectrum triangles with $k_2/k_1 = 1$ and 2. Blue filled squares show the estimate from PTHALOS in real space, green filled circles from *N*-body haloes in real space, red empty squares from PTHALOS in redshift space and orange empty circles *N*-body haloes in redshift space. All these estimates were made setting the maximum k_i ($i = 1, 2, 3$) to $0.17\,h\,{\rm Mpc}^{-1}$. The right-hand panel of Fig. 11 displays how the mean value of b_1, b_2 and $A_{\rm noise}$ changes with $k_{\rm max}$. The colour notation is the same in both panels. The error-bars in the right-hand panel represent the 1σ dispersion among all the realizations. We also include the values of $b_1^{\rm cross}$ and $b_2^{\rm cross}$ measured from the cross halo-matter power spectrum, $P_{\rm hm}$ and the cross halo-matter–matter bispectrum for comparison in black dashed lines,

$$b_1^{\rm cross} \equiv \langle P_{\rm hm}(k)/P_{\rm mm}(k)\rangle_{k,\,\rm realiz.}, \tag{33}$$

$$b_2^{\rm cross} \equiv \langle [B_{\rm hmm}(k_1,k_2,k_3) - b_1^{\rm cross} B_{\rm mmm}(k_1,k_2,k_3)]/[P_{\rm mm}(k_2)P_{\rm mm}(k_3)] + 4/7(b_1^{\rm cross}-1)S_2(k_1,k_2,k_3)\rangle_{k_i,\,\rm realiz.}, \tag{34}$$

where the average $\langle\ldots\rangle_{k,\,\rm realiz.}$ is taken among different k-modes and 70 different realizations of 2LPT dark matter and PTHALOS. For the $b_1^{\rm cross}$, we have considered k-bins with $k \leq 0.03\,h\,{\rm Mpc}^{-1}$, and for $b_2^{\rm cross}$ we have taken into account the $k_1/k_2 = 1, 2$ triangles with $0.01 \leq k_i[h\,{\rm Mpc}^{-1}] \leq 0.03$. The obtained values for the cross-bias parameters are: $b_1^{\rm cross} = 2.063$ and $b_2^{\rm cross} = 0.367$. The reason of using only such large-scale modes is because we have checked that 2LPT is not a good description of *N*-body dark matter at smaller scales.

In general, we do not observe any significant differences for the bias parameters estimated from the real space bispectrum: both PTHALOS (blue lines/symbols) and *N*-body haloes (green lines/symbols) present a similar distribution of b_1 and b_2 values over the entire k-range studied here. In redshift space, there is also in good agreement for the b_1 and b_2 between *N*-body (orange lines/symbols) and PTHALOS (red lines/symbols) prediction, with $\lesssim$1 per cent deviation for $k \leq 0.20\,h\,{\rm Mpc}^{-1}$. The bias parameters estimated from the bispectrum of *N*-body haloes and PTHALOS in real space present differences respect to the cross-bias parameters obtained from equations (33)–(34): b_1 is underestimated by $\sim$2.5 per cent respect to $b_1^{\rm cross}$ and b_2 is overestimated by $\sim$50 per cent respect to $b_2^{\rm cross}$. However, these differences are considerably reduced when $P_{\rm hh}$ is combined with $B_{\rm hhh}$. As shown in (Gil-Marín et al. 2014b, see table 4 and Fig. 9, where the same set of

N-body haloes is used), the bias parameters estimated in real and redshift space from $P_{\rm hh}^{(0)}$ and $B_{\rm hhh}^{(0)}$ are $b_1 = 2.05$ and $b_2 = 0.47$, which represent a deviation of $\sim$0.5 and $\sim$30 per cent respect to the $b_i^{\rm cross}$ values. Thus, we conclude that the linear bias parameter, b_1, obtained from $B_{\rm hhh}$ is biased by about $\sim$2.5 per cent respect to $b_1^{\rm cross}$, but this difference is reduced to 0.5 per cent when $P_{\rm hh}$ is added to the analysis. On the other hand, b_2 is significantly biased respect to the $b_2^{\rm cross}$ value.

We also observe differences in the $A_{\rm noise}$ parameter. First of all, redshift-space quantities present a lower $A_{\rm noise}$ parameter than real space quantities, which means that the shot noise tends to be more super-Poisson in redshift space. This result can be perfectly understood if we recall that objects in redshift space present a higher clustering, which produce super-Poisson statistics. We will return to this point in Section 5.5.2. Conversely, N-body statistics presents a significant different noise than PTHALOS statistics: N-body haloes have a shot noise closer to the Poisson prediction, whereas PTHALOS statistics have sub-Poissonian shot noise. The original differences observed in Fig. 10 are somehow absorbed by the $A_{\rm noise}$ parameter, and the bias parameters are relatively insensitive to these differences. The reason why these two simulations present different shot noise is unclear, but it may be related to the definition of halo, which varies from PTHALOS to N-body haloes. This issue should not concern us here, as we will treat $A_{\rm noise}$ as a nuisance parameter and marginalize over it. Moreover, we use the mocks to estimate error-bars not to model the signal directly.

We conclude that using PTHALOS rather than N-body haloes for the mock survey catalogues does not introduce significant systematic biases in the determination of the b_1 and b_2 parameters at $k_{\rm max} < 0.20\,h\,{\rm Mpc}^{-1}$. Smaller scales may introduce systematic errors, especially for the second-order bias, b_2. We also detect a small systematic in the estimation of b_1 between real and redshift spaces, which may arise from the halo bias and the modelling of redshift-space distortions (see Gil-Marín et al. 2014b for further discussion). Since this systematic is smaller than the statistical errors of this survey, we do not consider to correct for this effect.

The possible bias introduced on the growth parameter f is investigated in Section 5.6.

5.3 Test of the effect of the survey geometry on dark matter haloes

In this section, we test how the survey geometry, or mask, affects the power spectrum, and, more importantly, the bispectrum, and the performance of our approximations. In Section 3.6, we saw how the fiducial statistics are related to the measured statistics through a convolution with the window mask (see equations 8 and 11). In order to explore the effect of the mask, we use the 50 realizations of PTHALOS used in Section 5.2. These realizations are contained in a box with a constant mean density. Hereafter, we will refer to them as *unmasked* PTHALOS realizations. On the other hand, we also have 50 realizations of PTHALOS with the northern DR10 survey geometry. We will refer them as the *masked* PTHALOS realizations. By computing the power spectrum and bispectrum for these two different sets of 50 PTHALOS realizations, we can directly quantify the effect of the survey geometry.

For the power spectrum, the effect of the survey geometry is described by equation (8), which is an exact relation between the fiducial power spectrum, $P_{\rm gal}$, and the measured one, $\langle F_2^2\rangle$. The top-left panel of Fig. 12 presents the redshift-space power spectrum monopole from 50 unmasked realizations (blue symbols) and from the masked ones (red symbols). Both power spectra have been normalized by the linear power spectrum for clarity, therefore the plotted quantity is the square of an effective bias parameter. Differences are stronger at large scales and unimportant at small scales; this result is expected, as discussed in Section 3.6, where we argue that the effect of the survey mask becomes negligible at small scales.

To test the performance of the convolution described in equation (8), we divide the measured monopole power spectrum from the masked realizations, namely $\langle F_2^2\rangle$, by the linear power spectrum convolved with the window, as is described in the right-hand side of equation (8). This calculation is shown by the dashed red line. The original difference between the masked and unmasked power spectra is now corrected. The different lines of Fig. 12 are summarized as follows.

(i) $\langle F_2^2\rangle/P^{\rm lin}$, where $\langle F_2^2\rangle$ is computed from the unmasked sample (blue solid lines).
(ii) $\langle F_2^2\rangle/P^{\rm lin}$, where $\langle F_2^2\rangle$ is computed from the masked sample (red solid lines).
(iii) $\langle F_2^2\rangle/(P^{\rm lin}\otimes W_2)$, where $\langle F_2^2\rangle$ is computed from the masked sample and $P^{\rm lin}\otimes W_2$ is the convolution of $P^{\rm lin}$ with the survey window according to equation (14) (red dashed lines).

For the bispectrum, the effect of the mask is fully described by the equation (11). However, this equation involves a double convolution between the mask and the theoretical bispectrum formula. Since this calculation is computationally too expensive to be viable in practice, we have introduced the approximation described by equation (13), which splits the double convolution into two simple ones, i.e. the complexity of this computation is reduced to the same complexity used for the power spectrum. The remainder of the panels of Fig. 12 display the redshift-space bispectrum monopole measurement, $\langle F_3^3\rangle$ for the unmasked PTHALOS catalogue (blue lines) and for the masked data set (red solid lines).[6] Both the unmasked and masked bispectrum monopole are normalized by the real space matter prediction. The red dashed lines represent the masked bispectrum monopole normalized by the real space matter prediction convolved with the mask according the approximation described by equation (13). The different cases can be summarized as

(i) $\langle F_3^3\rangle/B_{\rm matter}$, where $\langle F_3^3\rangle$ is computed from the unmasked sample and $B_{\rm matter}$ is the tree-level matter bispectrum without any window effect (blue solid lines).

[6] The errors on the masked measurements are not shown for clarity.

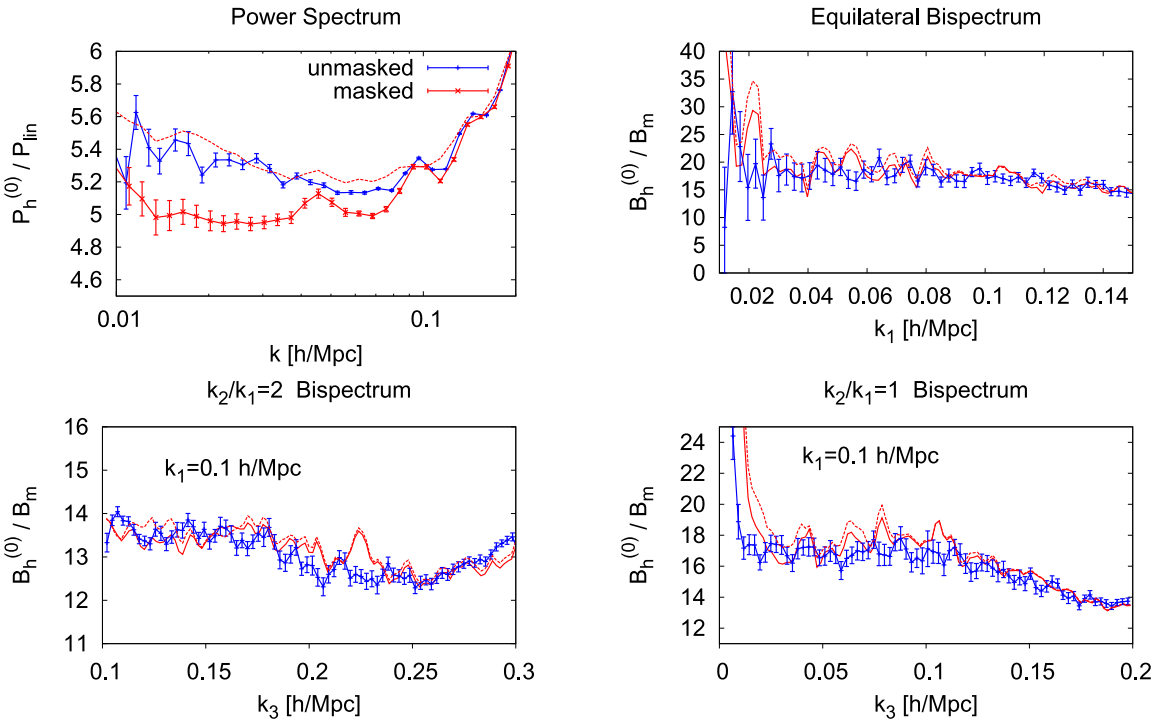

Figure 12. Power spectra (top-left panel) and bispectra (other panels) for PTHALOS in redshift space. The red (blue) solid lines are the measurements of the power spectrum and bispectrum from the masked (unmasked) PTHALOS normalized by their linear power spectrum and matter bispectrum, respectively: $\langle F_2^2\rangle / P^{\rm lin}$ and $\langle F_3^3\rangle / B_{\rm matter}$. The red dashed lines are the measurement of power spectrum and bispectrum from the masked PTHALOS normalized by the convolution of the linear power spectrum and real space matter bispectrum, respectively, as it described in the right-hand side of equation (8) and the approximation described by equation (13): $\langle F_2^2\rangle / (P^{\rm lin} \otimes W_2)$ and $\langle F_3^3\rangle / (B_{\rm matter} \otimes W_3)$. Poisson noise is assumed. The effect of the mask is accurately modelled by the FKP-estimator described in Sections 3.2 and 3.3.

(ii) $\langle F_3^3\rangle / B_{\rm matter}$, where $\langle F_3^3\rangle$ is computed from the masked sample and $B_{\rm matter}$ is the tree-level matter bispectrum without any window effect (red solid lines).

(iii) $\langle F_3^3\rangle / (B_{\rm matter} \otimes W_3)$, where $\langle F_3^3\rangle$ is computed from the masked sample and $B_{\rm matter} \otimes W_3$ is the convolution of $B_{\rm matter}$ with the survey window according to the approximation described in the second line of equation (13) (red dashed lines).

The difference between the dark matter bispectrum and its convolution according to equation (13) are small (red solid and dashed lines are similar). For the power spectrum, the effect of the mask is a clear broad-band suppression of $\sim$5 per cent level at scales of $k \sim 0.03\,h\,{\rm Mpc}^{-1}$ (and even higher at larger scales) and therefore include the standard mask calculation where calculating models. For the bispectrum, the effect of the mask is an enhancement of the bispectrum signal at $k_3 \lesssim 0.03\,h\,{\rm Mpc}^{-1}$. At smaller scales the differences are always below $\sim$10 per cent and we do not observe any clear systematic trend generated by the effect of the mask. However, we have checked that not including the mask in the bispectrum model (through the approximation described in equation 13) leads to a systematic error in the estimation of the linear and non-linear bias parameters by 1–2 per cent. Therefore, in this paper we will account the effect of the mask by correcting the bispectrum model using the approximation described in equation (13). In any case, since the bispectrum measurement presents a considerable scatter due to sample variance limitations (both for masked and unmasked), it is difficult to quantify exactly the accuracy of the approximation below $\sim$10 per cent.

For most of the shapes and scales of the bispectra compared here, the differences between masked and unmasked are at the few per cent level. However, for very squeezed triangles, $k_3 \lesssim k_1 = k_2$, the bispectrum for masked PTHALOS overpredicts the unmasked one, even when the approximation of the mask correction is applied (equation 13). We have determined that this is a large-scale effect; for $k_i \gtrsim 0.03\,h\,{\rm Mpc}^{-1}$, the masked and unmasked PTHALOS bispectrum agree, and the only discrepancies occur at large scales. Thus, in order to avoid spurious effects, in this paper we only consider k-modes larger than $0.03\,h\,{\rm Mpc}^{-1}$ when estimating the bispectrum.

We conclude that the approximation of equation (13) introduces a completely negligible systematic error for $k_i \gtrsim 0.03\,h\,{\rm Mpc}^{-1}$: thus the effect of the mask can accurately described by equations (8) and (13).

In order to test the performance of the approximation of equation (13) in describing the mask, we estimate b_1 and b_2 for the masked and unmasked PTHALOS using the bispectrum triangles with $k_2/k_1 = 1$ and 2. As before, we follow the method of Section 3.6 using the same model that in Section 5.2. We set the cosmological parameters to their fiducial values and set $A_{\rm noise}$ to be a free parameter in the fitting process. We adopt $k_{\rm min}$ to $0.03\,h\,{\rm Mpc}^{-1}$ to avoid the large-scale mask effects that cannot be accounted by our approximation. The left-hand panel of Fig. 13 presents a similar information to the one shown in Fig. 11 for $k_{\rm max} = 0.17\,h\,{\rm Mpc}^{-1}$. In this case, blue (green) points refer to the

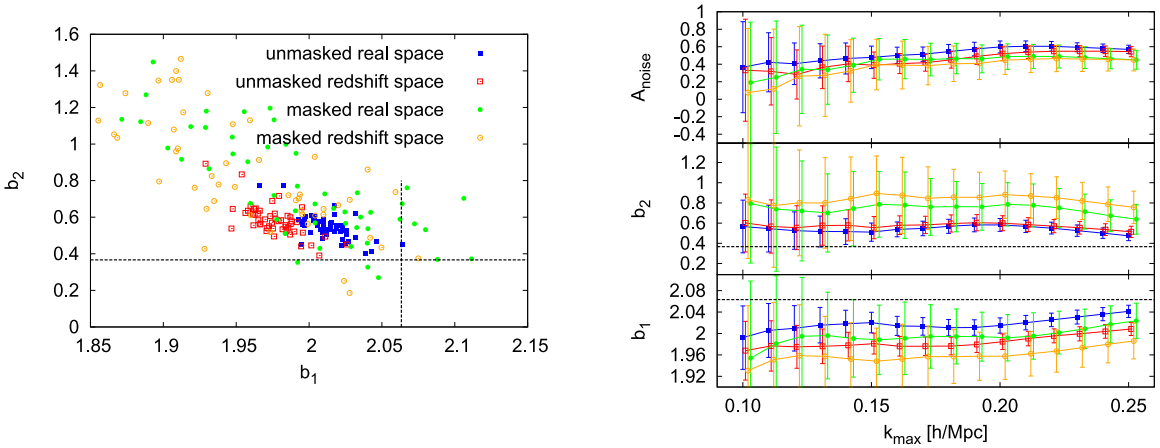

Figure 13. Left-hand panel: Best-fitting bias parameters for PTHALOS estimated from masked and unmasked realizations, from the real and redshift-space monopole bispectra. Green (blue) symbols are the best-fitting values from real space bispectrum masked (unmasked) realizations. Red (orange) symbols are best-fitting values from redshift-space monopole bispectrum masked (unmasked) realizations using $k_{\rm max} = 0.17\,h\,{\rm Mpc}^{-1}$. Right-hand panel: Best-fitting bias parameters and $A_{\rm noise}$ as a function of $k_{\rm max}$ using same colour notation that in the left-hand panel. Error-bars correspond to the 1σ dispersion among the different realizations. In both panels, black dashed lines represent the measured cross bias parameters defined in equations (33)–(34). The observed differences between the masked and unmasked catalogues are significantly smaller than 1σ of the typical statistical errors obtained for the CMASS galaxy survey.

best-fitting values b_1 and b_2 computed from the real space bispectrum monopole of unmasked (masked) PTHALOS, whereas red (orange) points are computed from the redshift-space monopole bispectrum of unmasked (masked) PTHALOS. In black dashed lines, the values of $b_1^{\rm cross}$ and $b_2^{\rm cross}$ measured according to equations (33)–(34) are shown. In both real and redshift space, the effect of the mask is to enhance the scatter. This effect is due to the differences in effective volumes between the masked and unmasked catalogues. Recalling that the masked catalogues have been generated from the unmasked ones by masking off haloes in order to match both the angular and the radial mask. The effective volume of the masked sample can be defined as (Tegmark 1997)

$$V_{\rm mask}^{\rm eff}(k) \equiv \int \frac{[\bar{n}(\boldsymbol{r})P(k)]^2}{[1+\bar{n}(\boldsymbol{r})P(k)]^2}\,{\rm d}^3\boldsymbol{r}. \tag{35}$$

At $k = 0.17\,h\,{\rm Mpc}^{-1}$, the amplitude of the power spectrum is about $8000\,[{\rm Mpc}\,h^{-1}]^3$ and the effective volume of the masked sample about $4.66\times10^8\,[{\rm Mpc}\,h^{-1}]^3$. For the unmasked sample, the volume is at any k, $V_{\rm unmask} = 2400^3\,[{\rm Mpc}\,h^{-1}]^3$. The effective volume has been reduced by $V_{\rm mask}^{\rm eff}/V_{\rm unmask} \simeq 0.033$ at scales of $k\sim0.17\,h\,{\rm Mpc}^{-1}$; thus we expect that at these scales the 1σ dispersion is $\sqrt{V_{\rm unmask}/V_{\rm mask}^{\rm eff}} \simeq 5.4$ higher. The right-hand panel of Fig. 13 displays the best-fitting values for b_1, b_2 and $A_{\rm noise}$ as a function of $k_{\rm max}$. In summary, the recovered b_1 tends to be smaller in the *masked* realizations than in the *unmasked* one, although the differences are smaller than the statistical errors. We observe these differences both in real and in redshift space, so they may be due to some residual effect of the mask. We quantify these shifts to be about ∼1 per cent for b_1, which represents a ∼40 per cent shift of 1σ of the masked realizations. The effect of the mask is more important for b_2: the *masked* realizations predict a ∼0.2 higher b_2 (∼30 per cent) than the *unmasked* realizations, which in this case represent ∼80 per cent shift of the 1σ of the masked realizations. These differences are within 1σ of the statistical errors. In particular, this $+0.2$ shift for b_2 tends to *cancel* the -0.2 shift seen in Sections 5.2 and 5.5.2. Moreover, in this paper we treat b_2 as a nuisance parameter that can absorb other systematic effects, such as the effect of truncation. We therefore advocate not correcting the b_2 recovered values for a systematic shift. The differences between the estimated bias parameters and the cross-bias parameters from equations (33)– (34) are similar and fully consistent with the ones reported in Section 5.2.

Bear in mind that all the statistical σ-values reported in Section 5 correspond to the marginal error distribution respect to b_1, b_2 and $A_{\rm noise}$; where f, σ_8, and σ_B have been set to their fiducial values. When we have analysed the data in Section 4, all the reported errors were marginalized with respect to all the parameters, i.e. $\{b_1,\ b_2,\ ,\sigma_8,\ f,\ A_{\rm noise},\ \sigma_{\rm FoG}^P,\ \sigma_{\rm FoG}^B\}$. Therefore, the statistical error values reported for the data in Section 4 are larger than the statistical errors reported in Section 5.

5.4 Test: Is the measurement consistent across shapes?

In this section, we test how the choice of different triangle shapes affects the estimation of the bias parameters from the bispectrum. In the ideal case, we should always obtain the same bias parameters, whatever shapes are chosen. However, the bispectrum model may present different systematic errors that can vary from shape to shape as the *anzatz* for effective the kernel was set a priori and then the kernel was calibrated to reduce the average differences from the simulations. Moreover, the maximum k at which the model is accurate might depend on the shape chosen.

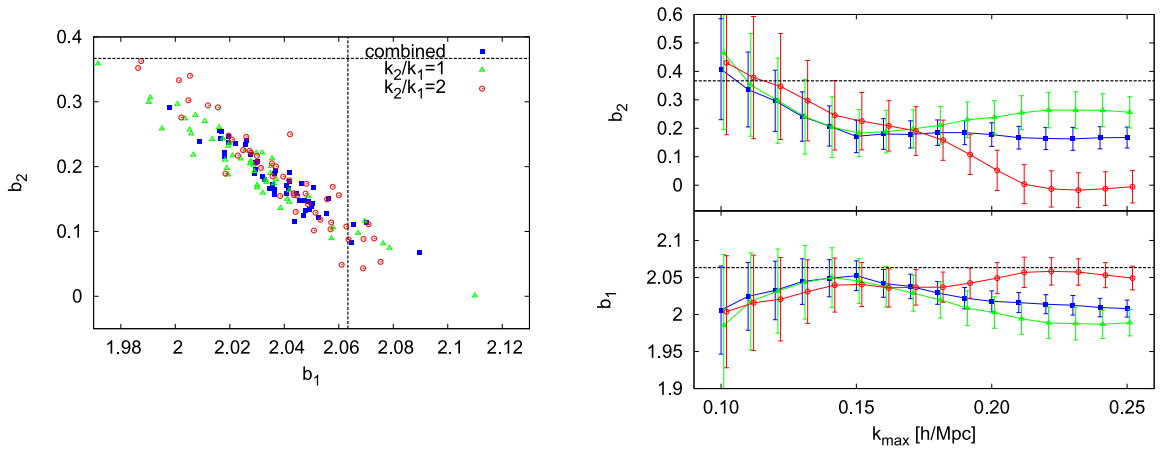

Figure 14. Left-hand panel: best-fitting bias parameter for PTHALOS from the real space bispectrum using different triangular shapes: $k_2/k_1 = 1$ (green points), $k_2/k_1 = 2$ (red points), and a combination of both (blue points), where $k_{\rm max} = 0.17\,h\,{\rm Mpc}^{-1}$. Right-hand panel: best-fitting bias parameters as a function of $k_{\rm max}$. Same colour notation in both panels. There is no significant shape dependence on the bias parameters for $k_{\rm max} \leq 0.17\,h\,{\rm Mpc}^{-1}$. In both panels, black dashed lines represent the measured cross bias parameters defined in equations (33)–(34).

The main point of this subsection is, therefore, to check whether the measurements of the bias parameters are consistent across shapes. Thus, the idea is to test effects one by one, isolating each from all the other as much as possible in order to gain insight into each of the presented tests. We tried to isolate this question from other factors such as survey effects or redshift-space distortions. Therefore, we think that a simple and clean way to approach this question is using unmasked boxes because they have larger volume and therefore is easier to detect potential systematics. Since the effect of the mask is tested elsewhere, we prefer not to re-introduce it here. We could have done this test in redshift space. However, redshift-space modelling adds an extra degree of complexness, which is addressed and discussed (separately) later in Section 5.5.2.

Here, we consider separately the performance of the two shapes adopted: $k_2/k_1 = 1$ and $k_2/k_1 = 2$. As we have said, for simplicity, we stay in real space and we use the unmasked realizations. As the shot noise should not vary with the triangle shape, we assume that the shot noise is given by Poisson statistics. Any variation form the Poisson prediction will be the same for all triangles and we are only concerned with relative changes. The theoretical model is given by equation (25), and the cosmological parameters are set to their fiducial values. To estimate the bias parameters, we use the bispectrum applying the method described in Section 3, as in Sections 5.2 and 5.3. We use the (unmasked) PTHALOS realizations as this also tests the performance of the adopted bias model. As discussed in Section 3.4, this approach is a truncation of an expansion of the complex relationship between $\delta_{\rm m}$ and $\delta_{\rm h}$, and will have a limited regime of validity.

The left-hand panel of Fig. 14 presents the best-fitting b_1 and b_2 parameters from the (unmasked) PTHALOS realizations. The red points show best-fitting parameters estimated from the bispectrum using the $k_2/k_1 = 1$ shape; the green points from $k_2/k_1 = 2$ shape; and the blue points both shapes combined. In this figure, the maximum k is set to $0.17\,h\,{\rm Mpc}^{-1}$. The right-hand panel displays the best-fitting parameters as a function of $k_{\rm max}$ with the same colour notation in both panels. The errors are the 1σ dispersion among the 50 PTHALOS realizations. Black dashed lines show the measured cross-bias parameters as defined in equations (33)–(34).

For $k_i \leq 0.18\,h\,{\rm Mpc}^{-1}$, both shapes predict the same bias parameters. For $k > 0.18\,h\,{\rm Mpc}^{-1}$, the $k_2/k_1 = 2$ shape tends to overpredict b_1 and underpredict b_2 with respect to the $k_2/k_1 = 1$ shape, for which the inferred parameters do not change significantly. In order to understand the behaviour of the $k_2/k_1 = 2$ triangles, one must recall that this shape is always limited by $k_1 \leq 0.1\,h\,{\rm Mpc}^{-1}$ and therefore by $k_2 \leq 0.2\,h\,{\rm Mpc}^{-1}$. So in the range $0.2 \leq k\,[h\,{\rm Mpc}^{-1}] \leq 0.3$, this shape only adds new scales through k_3, for those triangles with $k_1 \simeq 0.1\,h\,{\rm Mpc}^{-1}$. The decrease in recovered b_2 with $k_{\rm max}$ in Fig. 14, which matches the trend seen in the full fits, suggests that such triangles are responsible of misestimating the bias parameters at these scales. On larger scales, the effect of these triangles is suppressed by other shapes, which also satisfy $k_2/k_1 = 2$. In fact, when we add both $k_2/k_1 = 1$ and 2 shapes, the bias parameters at the scales $0.2 \leq k\,[h\,{\rm Mpc}^{-1}] \leq 0.3$ have a consistent behaviour with larger scales. This analysis confirms two features: (i) the responsibility for misestimating the bias parameters lies with the folded triangles with $k_1 \simeq k_3 \simeq k_2/2$, and (ii) the effect of these triangles is mitigated by including other shapes.

Comparing the real and redshift-space measurements later in Section 5.5.2, we find no systematic offset for b_1. Since there are no systematics between real and redshift space for b_1 and there are no systematic across shapes in real space, it is reasonable to assume that there are no systematics between shapes in redshift space either.

We conclude that for $k \leq 0.18\,h\,{\rm Mpc}^{-1}$, the best-fitting bias parameters are robust to the choice of the bispectrum shape (at least in real space and for haloes). For smaller scales, the behaviour of the $k_2/k_1 = 2$ triangles is responsible for underestimating b_2.

We observe that $b_1^{\rm cross}$ agrees better with the obtained b_1 from $B_{\rm hhh}$ than it does in Figs 11 and 13. On the other hand, b_2 is underestimated respect to $b_2^{\rm cross}$. These differences are because in this section we have set $A_{\rm noise}$ to 0 for simplicity. However, as we reported in Section 5.2, when $P_{\rm hh}$ is added to the analysis and $A_{\rm noise}$ is set free, we are able to recover b_1 with almost no bias, and b_2 with a $\sim$30 per cent bias.

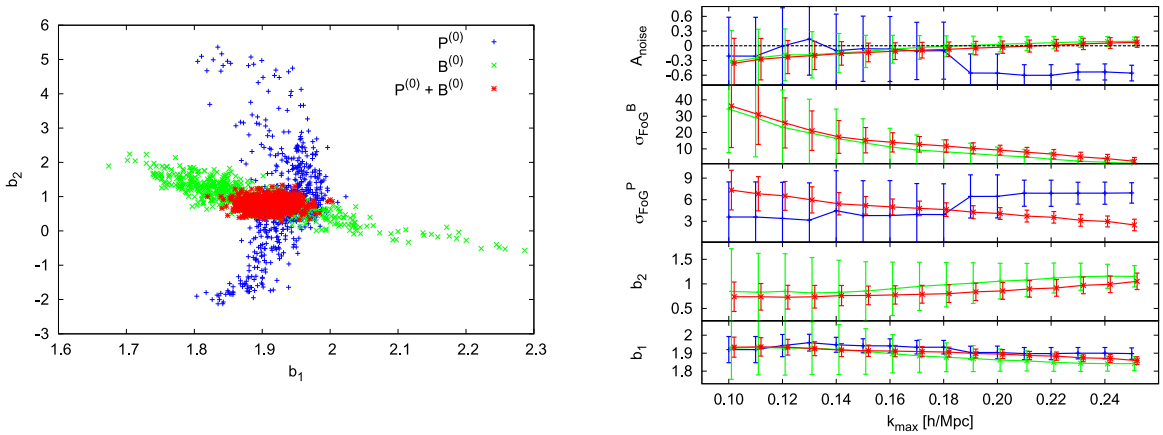

Figure 15. Left-hand panel: best-fitting b_1, b_2 and $A_{\rm noise}$ parameters for the galaxy mocks in redshift space, when the power spectrum monopole is used (blue points), when the bispectrum monopole is used (green points), and when both statistics are combined (red points). The quantities $\sigma^P_{\rm FoG}$ and $\sigma^B_{\rm FoG}$ are varied but are not shown for clarity. The maximum k used for this fitting is $0.17\,h\,{\rm Mpc}^{-1}$. Right-hand panel: best-fitting parameters as a function of $k_{\rm max}$. The error-bars are the 1σ dispersion for a single realization. There is a good agreement in the bias parameters, b_1 and b_2, estimated form the power spectrum and bispectrum.

5.5 Tests on galaxy mocks.

In this section, we perform a series of tests on the galaxy mocks used to estimate the errors of the data in Section 4. Since some tests have already been performed for the PTHALOS boxes they are not repeated for the mocks. By using mocks, we include many real-world effects present in the survey and test the performance of the adopted bias model, which was derived for haloes and not galaxies. In particular, we focus on three tests for aspects that can produce the systematic errors. First, we check the consistency of the bias parameters estimated from the power spectrum and bispectrum. An inconsistency would indicate that the bias model adopted cannot describe the clustering of galaxies. Secondly, we check the effect of redshift-space distortions on estimating the bias parameters when we combine the power spectrum and bispectrum. Finally, we investigate the possible systematic errors produced when we estimate the growth factor simultaneously as the bias parameters and σ_8. In order to estimate the best-fitting parameters, for both power spectrum and bispectrum, we use the same method applied to the data and described in Section 3. For the power spectrum, we use equation (22) for real space and equation 23 for redshift space, where the non-linear power spectrum terms $P_{\delta\delta}$, $P_{\delta\theta}$ and $P_{\theta\theta}$ are described by 2L-RPT (equation B20). The bispectrum is given by equations (25, real space) and (26, redshift space). The rms scatter among the mocks provides our estimate of the 1σ uncertainty for the survey measurements.

5.5.1 Bias parameters from power spectrum & bispectrum

We start by analysing the power spectrum and bispectrum in redshift space for the CMASS DR11 NGC galaxy mocks. These mocks contain the same observational effects as the data, so for extracting the statistical moments, we use the FKP estimator as described in Section 3.6. We weight the galaxies according to the systematic weights described in Section 2. The effect of the weights on the shot noise term is described in Appendix A.

Our goal is to extract the bias parameters from different statistics and to check their consistency. Since we are considering galaxy clustering in redshift space, we expect a non-linear damping term due to the FoG effect of the satellite galaxies inside the haloes. In total, the list of free parameters to be fitted: b_1, b_2, $A_{\rm noise}$, $\sigma^P_{\rm FoG}$ and $\sigma^B_{\rm FoG}$. In this section, we set the cosmological parameters f and σ_8 to their fiducial value, as well as fixing the shape of the linear matter power spectrum.

The left-hand panel of Fig. 15 presents the scatter of the 600 best-fitting values for the galaxy mocks with the CMASS DR11 NGC survey mask. The blue points are the constraints from the power spectrum monopole, green points from the bispectrum monopole, and red points the combination of both statistics. The $k_{\rm max}$ used is $0.17\,h\,{\rm Mpc}^{-1}$.

When using only one statistic there are large degeneracies between parameters. In particular, for the power spectrum monopole, b_2 is poorly constrained as it is highly degenerate with $A_{\rm noise}$ and $\sigma^P_{\rm FoG}$, whereas b_1 is relatively well constrained. Indeed b_2 only affects the power spectrum amplitude at mildly non-linear scales, which is precisely where the shot noise term and $\sigma^P_{\rm FoG}$ start to be relevant. On the other hand, the amplitude of the clustering at large scales is solely determined by b_1.

The constraints placed by the bispectrum on the bias parameters show a strong degeneracy between b_1 and b_2, and are consistent with the power spectrum predictions. The bispectrum constrains $A_{\rm noise}$ much better than the power spectrum for two reasons, (i) the shot noise is more important compared to the signal for the bispectrum and (ii) the shape dependence of this parameter is different from that of e.g. the bias parameters. The strong degeneracy between b_1 and b_2 is well known; at leading order in perturbation theory for a power-law power spectrum every shape can only constrain a linear combination of b_1 and b_2. The linear combination has a weak shape dependence, which is why combining different shapes both parameters can be measured.

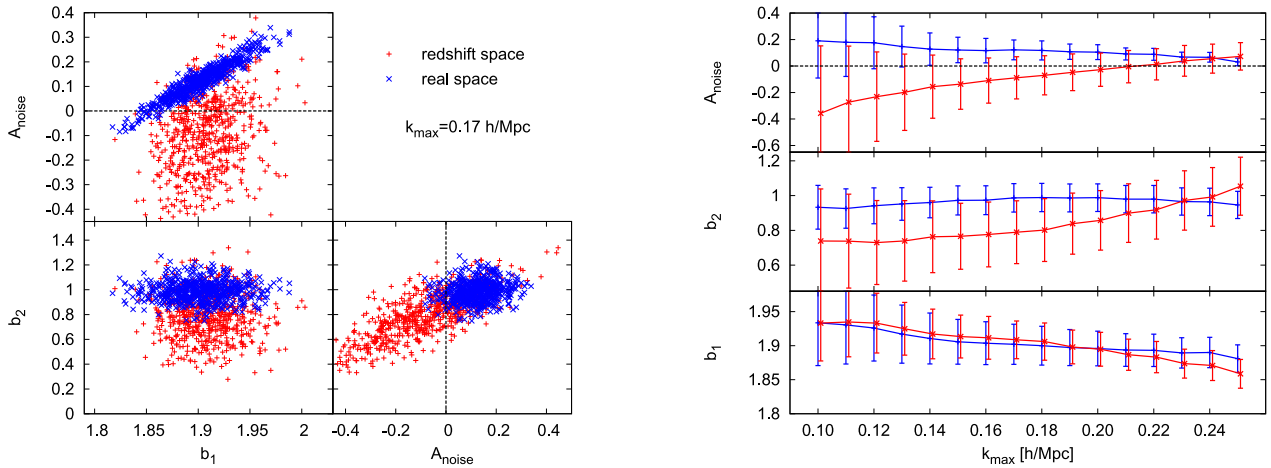

Figure 16. Left-hand panel: best-fitting parameters, b_1, b_2, $A_{\rm noise}$, for the galaxy mocks in real space (blue points) and in redshift space (red points). The maximum scale for the fitting is set to $k_{\rm max} = 0.17\,h\,{\rm Mpc}^{-1}$. Right-hand panel: best-fitting parameters as a function of $k_{\rm max}$. Same colour notation that in the left-hand panel. The error-bars correspond to 1σ dispersion of the 600 realizations. There is a good agreement in the bias parameters, b_1 and b_2, estimated form the real and redshift space.

The right-hand panel of Fig. 15 shows how the mean value of the best-fitting parameters estimated from the different statistics evolve with the variation of $k_{\rm max}$. The error-bars correspond to the 1σ dispersion among the different realizations. For $k_{\rm max} \lesssim 0.17\,h\,{\rm Mpc}^{-1}$, the bias parameters do not present a strong trend with the maximum scale used and the estimates obtained from power spectrum and bispectrum agree. However, as probe smaller scales, there is a small tension for the best-fitting value of b_1 between the power spectrum and bispectrum predictions. For the noise parameter, $A_{\rm noise}$, there is a suggestion that, as we increase $k_{\rm max}$, $A_{\rm noise}$ moves from slightly super-Poisson values ($A_{\rm noise} < 0$) to slightly sub-Poisson values ($A_{\rm noise} > 0$). We do expect this parameter to change with the scale, due to the different clustering at different scales.

We also observe that the two FoG parameters, $\sigma^P_{\rm FoG}$ and $\sigma^B_{\rm FoG}$, clearly decrease with $k_{\rm max}$. These parameters aim to parametrize the internal dispersion of galaxies inside haloes, consistent with setting the constraints $\sigma^P_{\rm fog} > 0$ and $\sigma^B_{\rm fog} > 0$, and there being low signal-to-noise ratio for small $k_{\rm max}$. In addition, we have argued previously that these parameters should be interpreted as nuisance rather than physical parameters.

A comparison of the bias parameters we would get from the cross galaxy-matter power spectrum is not possible for galaxies. The reason is that we do not have realizations of galaxies without the survey mask geometry. This is because the galaxies were added to the halo and dark matter field at the end of the production of the galaxy mocks, after the survey geometry was applied. Thus, it is not possible to compute a cross-correlation between dark matter and galaxies in this case.

5.5.2 *Effect of redshift-space distortions on the bias parameters*

In this section, we test the differences between the bias parameters and shot noise obtained from real and redshift-space power spectrum and bispectrum. Following the same methodology as in Section 5.5.1. In this section, we keep f and σ_8 fixed to their fiducial values in order to isolate the effect of redshift-space distortions into the bias parameters. Later in Section 5.6, we check the effects of the survey mask and of the modelling on estimating these two parameters. The left-hand panel of Fig. 16 displays the best-fitting parameters, b_1, b_2, and $A_{\rm noise}$ for the galaxy mocks in real space (blue points) and in redshift space (red points), where $k_{\rm max}$ is set to $0.17\,h\,{\rm Mpc}^{-1}$. The large-scale bias parameter, b_1, is consistent between real and redshift-space statistics. Conversely, the scatter of the b_2 parameter is larger for the redshift-space statistics. This result is due to the fact that for redshift space there are two more free parameters that describe the FoG effect. We know that both b_2 and $\sigma^P_{\rm FoG}$ affect the amplitude of the power spectrum at mildly non-linear scales: the two parameters are highly correlated, so by allowing $\sigma^P_{\rm FoG}$ to vary freely and then marginalizing over it we naturally add more uncertainty on b_2. On the other hand, we observe a small tendency for b_2 to be underestimated by about $\sim$0.2 in redshift space with respect to real space, although the shift is within 1σ.

The best-fitting value for $A_{\rm noise}$ is significantly different from real to redshift space. In real space, we see that $A_{\rm noise}$ tends to be slightly sub-Poisson, which is generally associated with halo-exclusion (Casas-Miranda et al. 2002; Manera & Gaztañaga 2011). This result indicates that for this particular type of galaxies, the halo exclusion dominates over the clustering at the scales studied here. Recall that for the CMASS galaxy sample, most of the haloes are occupied only by a central galaxy. However, in redshift space there is more clustering at large scales due to the Kaiser effect (Kaiser 1987) which is not prevented by halo exclusion. This extraclustering produces a higher shot noise in redshift space than in real space. In real space, halo exclusion is driving the shot noise towards the sub-Poisson region, whereas the redshift-space extraclustering drives it back towards the Poisson prediction and overtakes it slightly, making the final noise slightly super-Poisson. Since the extraclustering in redshift space is scale-dependent, we expect that the effective shot noise in redshift space possesses a scale dependence, from higher values at large scales to lower values at smaller scales. In the right-hand panel of Fig. 16, we see the dependence of the bias

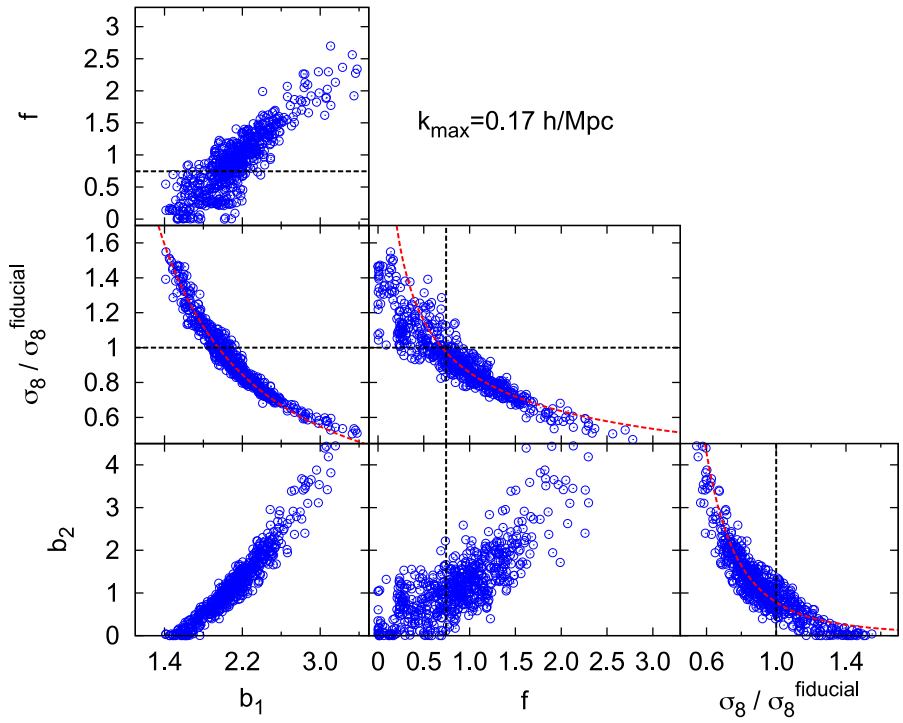

Figure 17. Best-fitting parameters, b_1, b_2, f, $\sigma_8/\sigma_8^{\rm fiducial}$ for 600 realizations of NGC galaxy mocks in redshift space (blue points) when power spectrum and bispectrum monopole are used. The relations between the best-fitting parameters can be empirically modelled by power law relations. In particular, red dashed lines represent the power-law relations for $\sigma_8 - b_1$, $\sigma_8 - b_2$ and $\sigma_8 - f$ (see the text for their exact values). Black dashed lines show the fiducial values for f and $\sigma_8/\sigma_8^{\rm fiducial}$. The maximum scale for the analysis is set to $k_{\rm max} = 0.17\,h\,{\rm Mpc}^{-1}$.

parameters and $A_{\rm noise}$ as a function of the maximum scale. The shot noise follows the expected trend; in real space, the shot noise is slightly sub-Poisson at all studied scales, whereas the shot noise in redshift space presents a scale dependence that moves from super-Poisson at large scales towards a sub-Poisson at smaller scales.

The right-hand panel of Fig. 16 demonstrates that the prediction for b_1 is consistent in real and redshift space and does not depend on the scale for $k_{\rm max} \lesssim 0.17\,h\,{\rm Mpc}^{-1}$, which is the range of validity for the power spectrum model. It is also clear that b_2 has some scale dependence in redshift space (which becomes more significant for $k > k_{\rm max}$). This behaviour may be due to the fact that this parameter is highly correlated with $\sigma_{\rm FoG}$, producing a parameter degeneracy in redshift space. Furthermore, the adopted FoG model is phenomenological and may not fully describe the non-linearities in the power spectrum (and perhaps also in the bispectrum); other parameters sensitive to the same range of scales may therefore be misestimated. However, given the size of the error-bars of this particular galaxy survey, the scale dependence of b_2 is negligible.

We conclude that, given the typical errors of CMASS DR11 galaxy sample, the redshift space models for the power spectrum (equation 23) and bispectrum (equation 26) give a consistent description of the (mock) galaxy clustering for scales $k \leq 0.17\,h\,{\rm Mpc}^{-1}$.

5.5.3 Constraining gravity and bias simultaneously

In this section, we drop the assumption that the growth of structure is described by GR and introduce two extra parameters: the linear growth rate f and the linear matter power spectrum amplitude parametrized by σ_8. We constrain simultaneously b_1, b_2, $A_{\rm noise}$, $\sigma^P_{\rm FoG}$, $\sigma^B_{\rm FoG}$, f and σ_8 from the measurement of the power spectrum and bispectrum monopole. We still have to assume that the bispectrum kernels remain the same as those calibrated on GR-based N-body simulations and that the mildly non-linear evolution of the power spectrum is well described by our model. We also assume that the initial linear power spectrum is given by GR. However, the analysis can be considered as a null hypothesis test if no significant deviations from the GR-predicted values for f are found. Moreover studies show that, at least for the $f(R)$ family of modified gravity theories, the GR-derived bispectrum kernel is still a good description of the bispectrum (Gil-Marín et al. 2011).

Fig. 17 displays the scatter for some of these parameters from 600 realizations of the NGC galaxy mocks (blue symbols). The black dashed lines show the fiducial values for f and σ_8. Since we are only using two statistics (power spectrum and bispectrum monopole), we cannot constrain efficiently both σ_8 and f. In a similar way, if we were using the power spectrum monopole and quadrupole, only the combination $f\sigma_8$ would be suitable to be efficiently constrained. For the joint analysis of power spectrum and bispectrum monopole, a slightly different combination of f and σ_8 is measured efficiently. This creates the possibility of measuring both f and σ_8 from a combined analysis of power spectrum monopole and quadrupole and bispectrum monopole (Gil-Marín et al. 2014b). While in the case of the power spectrum

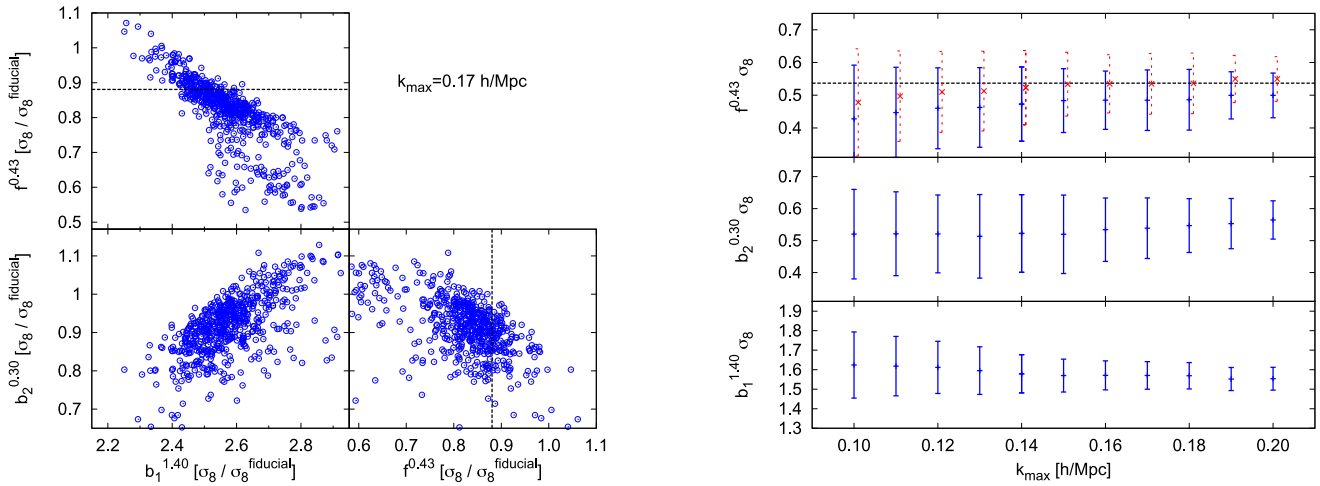

Figure 18. Left-hand panel: best-fitting parameters, $b_1^{1.40}\sigma_8$, $b_2^{0.30}\sigma_8$, $f^{0.43}\sigma_8$, for 600 realizations of galaxy mocks in redshift space (blue points) when power spectrum and bispectrum monopole are measured. When these new variables are used, the scatter distribution is more Gaussian and the errors can be estimated from the dispersion among the different realizations. Black dashed lines show the fiducial values for $f^{0.43}\sigma_8$. The maximum scale for the fitting is set to $k_{\rm max} = 0.17\,h\,{\rm Mpc}^{-1}$. Right-hand panel: single parameters estimate as a function of $k_{\rm max}$. Blue error-bars correspond to 1σ dispersion. For the panel corresponding to $f^{0.43}\sigma_8$, the results corrected by a systematic offset of 0.05 are shown in red dashed lines. No significant $k_{\rm max}$-dependence is observed.

monopole and quadrupole, it is clear from examining the large-scale limit of the model that the relevant parameter combination is $\sigma_8 \sim f^{-1}$, this is not the case for the power spectrum and bispectrum monopole combination. The bias parameters are involved and even at large scales, the power spectrum has a non-negligible contribution of b_2. Fig. 17 suggests that parameters are mostly distributed along one-to-one relations determined directly from the distribution of the best-fitting parameters from the mocks. Thus, we can empirically determine the degeneracy directions of importance.

We approximate these relations with power-law equations, which are the red dashed lines in Fig. 17. This information suggests that we can constrain three combinations of the four parameters b_1, b_2, f and σ_8. In particular, given the *ansatz* relations $\sigma_8 \sim f^{-n_1}$, $\sigma_8 \sim b_1^{-n_2}$ and $\sigma_8 \sim b_2^{-n_3}$, the best fit to the distributions around the maximum are $n_1 = 0.43$, $n_2 = 1.40$, $n_3 = 0.30$. We recognize that these values do not correspond to universal relations for these parameters, but are effective fits given a particular galaxy population. For other samples they may no longer be optimal.

Results in the new combinations $f^{0.43}\sigma_8$, $b_1^{1.40}\sigma_8$ and $b_2^{0.30}\sigma_8$ are shown in right-hand panel of Fig. 18. In these new variables, the distribution appears more Gaussian, and it is more meaningful to estimate the error-bars from the dispersion of the distribution.

In the right-hand panel, the blue solid lines show the mean and the error-bars (computed from the distribution of the mocks best-fitting values) for these variables as a function of $k_{\rm max}$. The black dashed line in the panels of Fig. 18 is the fiducial value for $f^{0.43}\sigma_8$. There is an offset between the mean of the galaxy mocks and the fiducial value, which is constant with $k_{\rm max}$. This offset is at the 0.05 level, below 1σ statistical error for the survey, but the analysis tends to underestimate the fiducial value of $f^{0.43}\sigma_8$. In red dashed lines, the value of $f^{0.43}\sigma_8$ is corrected by this 0.05 offset. Recall that the error on the mean is some 24 times smaller than the reported errors, so while the systematic shift is below the statistical error for the survey, it can be measured from the mocks with high statistical significance, and can also be observed in Fig 17. In the next section, we explore the source of this systematic error.

5.6 Systematic errors on f and σ_8

There are several effects that could systematically shift in the combination $f^{0.43}\sigma_8$. To assess the treatment of the survey window and the fact that galaxy mocks are based on PTHALOS and not on N-body haloes, we estimate b_1, b_2, f, σ_8, $A_{\rm noise}$ and $\sigma^P_{\rm FoG}$ from the 20 realizations of N-body haloes and from the 50 realizations of masked and unmasked PTHALOS. Since we are considering the clustering of haloes, all the FoG contributions should vanish (i.e. we should strictly set $\sigma^P_{\rm FoG}$ and $\sigma^B_{\rm FoG}$ to 0). However, it has been shown (Nishimichi & Taruya 2011) that at least for the power spectrum, it is necessary to incorporate a term of the form of $\sigma^P_{\rm FoG}$ in order to account for inaccuracies of the model, hence our inclusion of $\sigma^P_{\rm FoG}$ as a free parameter.

Fig. 19 presents the distribution of the best-fitting values for b_1, b_2, f and σ_8 for N-body haloes (black filled circles), for unmasked PTHALOS (blue empty circles) and for masked PTHALOS (red empty squares) estimated from the power spectrum monopole and bispectrum. Recall that these three different halo catalogues have different effective volumes, so we expect different magnitudes of the scatter for the estimated parameters. However, the best-fitting values should be the same for the three sets if there are no systematics related to the nature of the simulation or the window. We observe that there are no significant differences when comparing masked and unmasked catalogues, indicating (as already shown in Section 5.3) that the survey window is modelled correctly for both the power spectrum and bispectrum. If we now compare the N-body and PTHALOS results, we notice few differences. N-body haloes tend to have a smaller value for b_1, b_2 and f, but

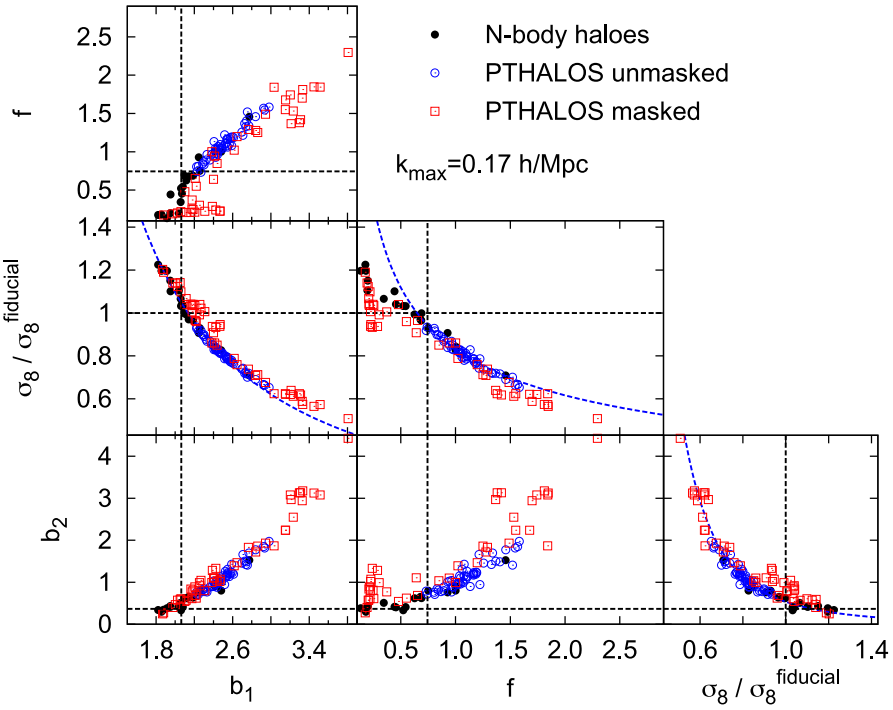

Figure 19. Best-fitting parameters, b_1, b_2, f, $\sigma_8/\sigma_8^{\rm fiducial}$ for 20 realizations of N-body haloes in redshift space (black filled circles), for 50 realizations of masked (red empty squares) and unmasked (blue empty circles) PTHALOS when power spectrum and bispectrum monopole are measured. Black dashed lines show the fiducial values for f and $\sigma_8/\sigma_8^{\rm fiducial}$ and the measured cross-bias parameters defined in equations (33)–(34). Blue dashed lines show the power-law relations for some of these parameters (see the text for their exact values). The maximum scale for the fitting is set to $k_{\rm max} = 0.17\,h\,{\rm Mpc}^{-1}$. The power-law relations observed in Fig. 17 for the galaxy mocks are very similar for N-body haloes and PTHALOS, and therefore potentially applicable to the observed data set.

a higher value for σ_8, than PTHALOS. However, these differences are small and lie along the degeneracy direction (blue dashed lines). As for galaxy mocks, we assume power-law relations between b_1, b_2 and f. In black dashed lines, we show the cross-bias parameters reported in Section 5.2 combined with σ_8.

We assume that the values for the indices n_1, n_2 and n_3 are the same as those obtained from the galaxy mocks: $n_1 = 0.43$, $n_2 = 1.40$ and $n_3 = 0.30$. Independently of these relations, the parameter distributions for N-body haloes and PTHALOS are slightly offset from the fiducial value in the f-σ_8 panel of Fig. 19 in a similar way as observed for the galaxy mocks in Fig. 17.

The relation between f and σ_8 obtained (i.e. $f^{0.43}\sigma_8$) is not always perfect and does not hold for any value of f or σ_8. This can be seen in the $\sigma_8 - f$ panel in Fig. 19. Let us say that f and σ_8 are correlated according to $f^{0.43}\sigma_8 =$ constant, for $0.3 \leq f$, which is a wide range for the possible values of f (it is very unlikely that the observed galaxies have an f value outside this range, but we could take it as a mild prior). We note that for the unmasked PTHALOS the volume of the boxes is large enough that f is always inside this range, and the relation $f^{0.43}\sigma_8$ holds for all the mocks. When we reduce the volume (masking the boxes) the scatter increases and some realizations predict a best-fitting value of f outside this range. Since for these points the $f^{0.43}\sigma_8$ relation does not hold anymore they seem to present a larger deviation.

The left-hand panel of Fig. 20 displays the distribution of these parameters combinations obtained from the different realizations of N-body haloes, masked and unmasked PTHALOS with the same colour notation that in Fig. 19. The fiducial value for $f^{n_1}\sigma_8$ is represented by black dotted line. For PTHALOS and N-body, we have plotted the values whose $f < 0.3$ as crosses and the values whose $f > 0.3$ as squares and circles, respectively. We see clearly that the binomial distribution observed for PTHALOS and N-body in the $f^{0.43}\sigma_8 - b_1^{1.40}\sigma_8$ panel is due to the fact that low f values do not follow the $f^{0.43}\sigma_8$ relation. In this section, we consider the mild prior $f > 0.3$, which helps to hold the $f^{0.43}\sigma_8$ relation, when the total volume is small. In these new variables and taking into account the mild prior on f, is easy to appreciate the good agreement between masked and unmasked realizations and between PTHALOS and N-body haloes. The right-hand panel of Fig. 20 shows how these parameters depend on $k_{\rm max}$. Again the offset in $f^{0.43}\sigma_8$ is constant across $k_{\rm max}$ and also present at large scales. For the PTHALOS and N-body haloes, the mild prior $f > 0.3$ has been applied.

This feature indicates that the systematic offset observed in Section 5.5.3 is present in PTHALOS, with and without survey mask, and in N-body haloes. It is therefore produced by a failure of the modelling of the combination of redshift-space distortions and bias for haloes. Gil-Marín et al. (2014b) reports that the modelling of redshift-space distortions adopted here works well and does not induce any bias for the (unbiased) dark matter distribution in redshift space. When we examine (biased) haloes in redshift space, the adopted model seem to be insufficient to reach accuracy levels of few per cent. We believe we have reached the limitations of the currently available semi-analytic modelling of redshift-space clustering of dark matter tracers: shrinking the statistical errors below this level is not useful until these limitations can be overcome.

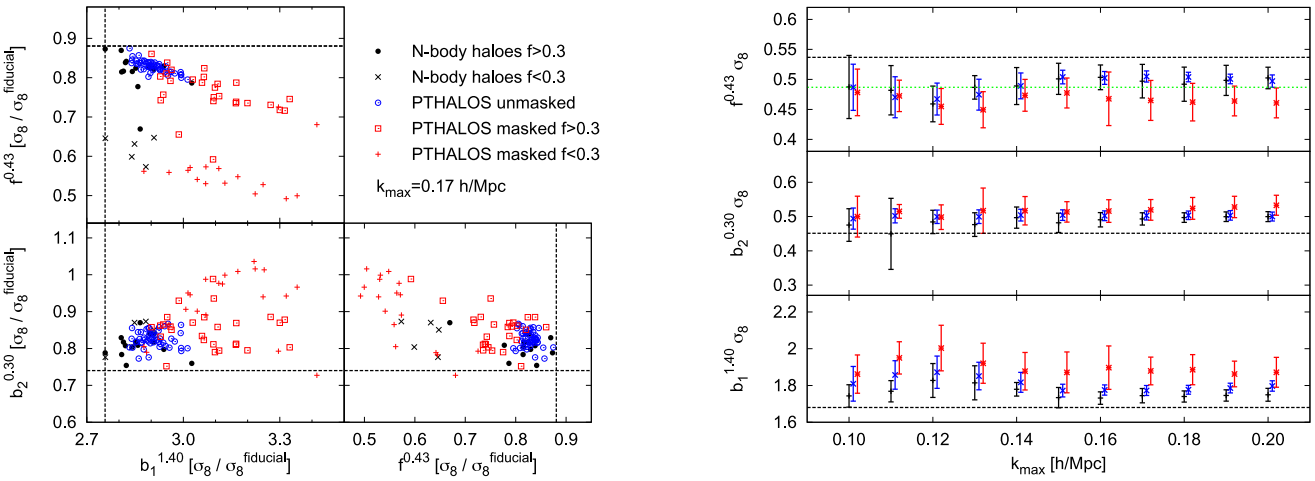

Figure 20. Best-fitting parameters, $b_1^{1.40}\sigma_8$, $b_2^{0.30}\sigma_8$, $f^{0.43}\sigma_8$, for 20 realizations of N-body haloes, masked and unmasked PTHALOS (same colour notation that in Fig. 19), when power spectrum and bispectrum monopole are measured. For PTHALOS and N-body haloes, the crosses show those realizations whose best fit f is below 0.3, whereas squares and circles above 0.3, respectively. Only those realizations whose $f > 0.3$ have been included in the computation of mean values and error-bars of the right-hand panel. Black dashed lines show the fiducial values for $f^{0.43}\sigma_8$ and for $(b_1^{\rm cross})^{1.40}\sigma_8$ and $(b_2^{\rm cross})^{0.30}\sigma_8$. The maximum scale for the fitting is set to $k_{\rm max} = 0.17\,h\,{\rm Mpc}^{-1}$. Green dotted line is the theoretical prediction reduced by a systematic offset of 0.05. When the new variables are used the original distributions of Fig. 19 appears more Gaussian. However, the systematic shift on $f^{0.43}\sigma_8$ observed for the galaxy mocks, is also present for N-body haloes. This indicates that the systematic shift is not due to a limitation of the mocks, but a limitation in the theoretical description of the halo power spectrum and bispectrum in redshift space.

We conclude that the method adopted here to measure $f^{0.43}\sigma_8$ from the power spectrum monopole and bispectrum underestimate its fiducial value by about 0.05, which is a 10 per cent effect. In the right-hand panel of Fig. 20 this offset is shown by the green dotted line, while black dashed line corresponds to the fiducial value. When reporting our main results, we will always apply a correction for this offset. We also see that the values $b_1^{1.40}\sigma_8$ and $b_2^{0.30}\sigma_8$ are biased respect to the true values of σ_8 and the measured cross-bias parameters defined in equations (33)–(34): $b_1^{1.40}\sigma_8$ and $b_2^{0.30}\sigma_8$ are biased $\sim$10 per cent higher respect to $(b_1^{\rm cross})^{1.40}\sigma_8$ and $(b_2^{\rm cross})^{0.30}\sigma_8$, respectively. In this paper, we do not correct the bias parameter by the systematic shifts found respect to the cross-bias parameters. The main result of this paper is the constraint on the combination of f and σ_8 from the CMASS galaxy data, but not the galaxy bias parameters, the shot noise properties or the FoG redshift-space distortion parameter, which we treat as a nuisance parameters.

6 CONCLUSIONS

We have presented a measurement of the bispectrum of the CMASS DR11 galaxy sample of the BOSS of the SDSSIII. This is the largest survey (in terms of volume and number of objects) to date where the bispectrum has been measured, offering an unprecedented signal-to-noise ratio.

The bispectrum is the Fourier counterpart of the three-point function, and as such encloses information about non-linear clustering, biasing and gravity. Because of the complicated nature of redshift-space distortions on the triplets of Fourier modes that create the bispectrum, we have only considered the bispectrum monopole (i.e. angle-averaged with respect to the line-of-sight direction). The bispectrum signal is detected at high statistical significance, which enables its use to measure cosmological parameters of interest. The bispectrum shows the characteristic shape dependence induced by gravitational evolution in the mildly non-linear regime, indicating that the large volume of the survey allows us to discard highly non-linear scales and still have a useful signal-to-noise ratio. We aim at measuring galaxy bias and the growth of structure. To reduce degeneracies among these quantities, we jointly fit the power spectrum and bispectrum monopoles.

In order to interpret this signal, we have developed a description of the mildly non-linear power spectrum and bispectrum for biased dark matter tracers in redshift space, which is presented in Section 3. The bias model is particularly important. The simple, local, quadratic bias expansion, which has been the workhorse to date to analyse the bispectrum from surveys and is widely used for forecasts, is not good enough for the precision offered by the CMASS DR11 survey. For instance, the bias parameters recovered from analysing the bispectrum are not consistent with those obtained from the power spectrum adopting this bias model. Similar problems were reported by Pollack, Smith & Porciani (2014) when the local model is applied. Here, for CMASS galaxies, we must move beyond this simple model. We adopt for the bispectrum a non-linear, non-local bias model that was originally developed for haloes (McDonald & Roy 2009; Baldauf et al. 2012; Gil-Marín et al. 2014b; Saito et al. 2014) and recently applied to power spectrum analyses (Beutler et al. 2014). This approach is still a two-parameter bias model, but b_1 and b_2 do not have the same meaning as in the quadratic local bias model. Despite this bias model being strictly physically motivated for dark matter haloes, we apply it to galaxies, motivated by the fact that CMASS galaxies are believed to closely trace massive dark matter haloes. Nevertheless, the quadratic bias parameter b_2 should be treated as an effective parameter that absorbs limitations of the adopted modelling.

The mildly non-linear description of these statistics in redshift space is also a crucial starting ingredient; because of the complicated formulae, the description and derivations are reported in the appendices. In brief, we use the bispectrum kernel calibrated from *N*-body simulations in real and redshift space and include a suite of effective parameters which, in principle, describe physical quantities such as non-linear incoherent velocity dispersion (FoG effects), and deviations from purely Poisson shot noise. In practice, we treat these quantities as nuisance parameters to be marginalized over, and these parameters *absorb* several of possible inaccuracies of the modelling. Even with this improvement, there are indications that we have reached the limitations of the currently available modelling of redshift-space clustering of dark matter tracers: shrinking the statistical errors below this level is not useful until these limitations can be overcome.

Our measurements are supported by an extensive series of tests performed on dark matter *N*-body simulations, halo catalogues (obtained both from *N*-body and PTHALOS simulations) and mock galaxy catalogues. These tests are also used to identify the regime of validity of the adopted modelling: this regime occurs when all k modes of the bispectrum triangles are larger than $0.03\,h\,\mathrm{Mpc}^{-1}$ and less than $k_{\rm max} = 0.17\,h\,\mathrm{Mpc}^{-1}$ being conservative or less than $k_{\rm max} = 0.20\,h\,\mathrm{Mpc}^{-1}$ being more optimistic. We also account for real word effects such as survey windows and systematic weighting of objects. We opt to add in quadrature the statistical error and half of the systematic shift to account for the uncertainty in the systematic correction.

The bispectrum calculation is computationally intensive because of the number of bispectrum triplets, which increases as the number of k modes in the survey to the third power. For this reason, we only consider a subset of all possible bispectrum shapes. This is consistent with what has been done in previous literature; while it does not extract all the possible information from the survey it is a good compromise between accuracy and computational feasibility. If we were to use all possible shapes we could, in principle, almost halve the statistical error-bars. The price to pay, however, will be much less control over the theoretical modelling, and the resulting measurements would become systematic-dominated.

An additional complication we had to overcome to perform the analysis is that there is no fully developed, tested and motivated estimator for the bispectrum or a quantity that depends on it (see e.g. Verde et al. 2013), whose probability distribution function is known, and none exist for the joint power spectrum and bispectrum analyses. We therefore had to resort to a suboptimal but still unbiased approach. We ignore correlations between shapes in determining the parameters and then estimate the errors from the distribution of the best parameters values obtained from 600 mock galaxy surveys. Our cosmologically interesting parameters are two bias parameters b_1 and b_2, the linear matter clustering amplitude σ_8 and the growth rate of fluctuations $f = \mathrm{d}\ln\delta/\mathrm{d}\ln a$, where δ denotes the dark matter over density and a the scale factor. If gravity is described by GR at cosmological scales, then f is effectively given by $\Omega_{\rm m}$.

We find that even jointly, the bispectrum and power spectrum monopole cannot measure all four parameter separately, but do constrains the following combinations: $f^{0.43}\sigma_8$, $b_1^{1.40}\sigma_8$ and $b_2^{0.30}\sigma_8$. In these variables, the distribution of the best-fitting parameters for the mock catalogues are much closer a Gaussian distribution than in the original four parameters. When we set $k_{\rm max} = 0.17\,h\,\mathrm{Mpc}^{-1}$, we obtain $b_1(z_{\rm eff})^{1.40}\sigma_8(z_{\rm eff}) = 1.672 \pm 0.060$ and $b_2^{0.30}(z_{\rm eff})\sigma_8(z_{\rm eff}) = 0.579 \pm 0.082$ at the effective redshift of the survey, $z_{\rm eff} = 0.57$. The main cosmological result in this case is the constraint on the combination $f^{0.43}(z_{\rm eff})\sigma_8(z_{\rm eff}) = 0.582 \pm 0.084$. Adopting a less conservative approach allow us to set $k_{\rm max} = 0.20\,h\,\mathrm{Mpc}^{-1}$, which produces: $b_1(z_{\rm eff})^{1.40}\sigma_8(z_{\rm eff}) = 1.681 \pm 0.046$, $b_2^{0.30}(z_{\rm eff})\sigma_8(z_{\rm eff}) = 0.571 \pm 0.043$ and $f^{0.43}(z_{\rm eff})\sigma_8(z_{\rm eff}) = 0.584 \pm 0.051$.

The $f^{0.43}\sigma_8$ combination is affected by a 0.05 systematic error – extensively quantified and calibrated from simulations – and this correction has been applied. This issue represents the main obstacle in further reducing the statistical errors.

The present analysis measures a combination of f–σ_8 that differs from that obtained from the combination of the power spectrum monopole and quadrupole (which yields $f\sigma_8$). This creates the possibility of measuring both f and σ_8 from a combined analysis of power spectrum monopole and quadrupole and bispectrum monopole. The potential of this approach is presented in the companion paper (Gil-Marín et al. 2014a); a more detailed joint analysis is left to future work.

The mock catalogues based in PTHALOS are adequate for performing the analysis described in this paper. In particular, they are essential to extract the empirical relations between b_1, b_2, σ_8 and f, which are applied to the data, as well as to obtain a reliable estimation of the diagonal terms of the covariance matrix of the power spectrum and bispectrum. On the other hand, the limitation of the mocks for describing the observed clustering of the data at mildly non-linear scales suggests that there is space for improvement. Performing a similar bispectrum analysis on the next generation of surveys will require more realistic mocks that better match the observations both of the mildly non-linear power spectrum and bispectrum for the adopted tracers. This will be an important ingredient to improve the modelling of the data to significantly reduce the systematic errors and keep them below the statistical ones.

The constraints on $f^{0.43}\sigma_8$ will be useful in a joint analysis with other cosmological data sets (in particular CMB data) for setting stringent constraints on neutrino mass, gravity, curvature as well as number of neutrino species. Further, the joint constraints on $f^{0.43}\sigma_8$, $b_1^{1.40}\sigma_8$, and $b_2^{0.30}\sigma_8$, can be used to include the broad-band shape and amplitude of the galaxy power spectrum when doing cosmological parameters estimation. These are presented in a companion paper (Gil-Marín et al. 2014a).

ACKNOWLEDGEMENTS

HGM thanks Florian Beutler for useful discussions about the survey mask and the power spectrum and bispectrum estimator. We thank Román Scoccimarro for useful comments on the final draft. We also thank Beth Reid for providing the *N*-body haloes used to test the systematics of the power spectrum and bispectrum model.

HGM is grateful for support from the UK Science and Technology Facilities Council through the grant ST/I001204/1. JN is supported in part by ERC grant FP7-IDEAS-Phys.LSS. LV is supported by the European Research Council under the European Community's Seventh Framework Programme grant FP7-IDEAS-Phys.LSS and acknowledges Mineco grant FPA2011-29678- C02-02. WJP is grateful for support from the UK Science and Technology Facilities Research Council through the grant ST/I001204/1, and the European Research Council through the 'Darksurvey' grant.

Funding for SDSS-III has been provided by the Alfred P. Sloan Foundation, the Participating Institutions, the National Science Foundation, and the US Department of Energy Office of Science. The SDSS-III web site is http://www.sdss3.org/.

SDSS-III is managed by the Astrophysical Research Consortium for the Participating Institutions of the SDSS-III Collaboration including the University of Arizona, the Brazilian Participation Group, Brookhaven National Laboratory, University of Cambridge, Carnegie Mellon University, University of Florida, the French Participation Group, the German Participation Group, Harvard University, the Instituto de Astrofisica de Canarias, the Michigan State/Notre Dame/JINA Participation Group, Johns Hopkins University, Lawrence Berkeley National Laboratory, Max Planck Institute for Astrophysics, Max Planck Institute for Extraterrestrial Physics, New Mexico State University, New York University, Ohio State University, Pennsylvania State University, University of Portsmouth, Princeton University, the Spanish Participation Group, University of Tokyo, University of Utah, Vanderbilt University, University of Virginia, University of Washington, and Yale University. This research used resources of the National Energy Research Scientific Computing Center, which is supported by the Office of Science of the US Department of Energy under Contract no. DE-AC02-05CH11231.

Numerical computations were done on the Sciama High Performance Compute (HPC) cluster which is supported by the ICG, SEPNet and the University of Portsmouth and on Hipatia ICC-UB BULLx High Performance Computing Cluster at the University of Barcelona.

The simulations for *N*-body haloes used in this paper were analysed at the National Energy Research Scientific Computing Center, the Shared Research Computing Services Pilot of the University of California and the Laboratory Research Computing project at Lawrence Berkeley National Laboratory.

REFERENCES

Ahn C. P. et al., 2012, ApJS, 203, 21
Ahn C. P. et al., 2014, ApJS, 211, 17
Anderson L. et al., 2012, MNRAS, 427, 3435
Anderson L. et al., 2014, MNRAS, 441, 24
Baldauf T., Seljak U., Desjacques V., McDonald P., 2012, Phys. Rev. D, 86, 083540
Bernardeau F., 1994, ApJ, 433, 1
Bernardeau F., Colombi S., Gaztañaga E., Scoccimarro R., 2002, Phys. Rep., 367, 1
Beutler F. et al., 2014, MNRAS, 443, 1065
Blake C. et al., 2013, MNRAS, 436, 3089
Bolton A. S. et al., 2012, AJ, 144, 144
Bouchet F. R., Juszkiewicz R., Colombi S., Pellat R., 1992, ApJ, 394, L5
Casas-Miranda R., Mo H. J., Sheth R. K., Boerner G., 2002, MNRAS, 333, 730
Catelan P., Moscardini L., 1994a, ApJ, 426, 14
Catelan P., Moscardini L., 1994b, ApJ, 436, 5
Catelan P., Lucchin F., Matarrese S., Moscardini L., 1995, MNRAS, 276, 39
Catelan P., Lucchin F., Matarrese S., Porciani C., 1998, MNRAS, 297, 692
Chan K. C., Scoccimarro R., Sheth R. K., 2012, Phys. Rev. D, 85, 083509
Chuang C.-H. et al., 2013, MNRAS, 433, 3559
Crocce M., Scoccimarro R., 2006, Phys. Rev. D, 73, 063519
Davis M., Efstathiou G., Frenk C. S., White S. D. M., 1985, ApJ, 292, 371
Dawson K. S. et al., 2013, AJ, 145, 10
Doi M. et al., 2010, AJ, 139, 1628
Eisenstein D. J., 1997, preprint (arXiv:e-prints)
Eisenstein D. J. et al., 2011, AJ, 142, 72
Feldman H. A., Kaiser N., Peacock J. A., 1994, ApJ, 426, 23
Feldman H. A., Frieman J. A., Fry J. N., Scoccimarro R., 2001, Phys. Rev. Lett., 86, 1434
Fry J. N., 1984, ApJ, 279, 499
Fry J. N., 1994, Phys. Rev. Lett., 73, 215
Fry J. N., Gaztañaga E., 1993, ApJ, 413, 447
Fry J. N., Seldner M., 1982, ApJ, 259, 474
Fukugita M., Ichikawa T., Gunn J. E., Doi M., Shimasaku K., Schneider D. P., 1996, AJ, 111, 1748
Gaztañaga E., Scoccimarro R., 2005, MNRAS, 361, 824
Gil-Marín H., Schmidt F., Hu W., Jimenez R., Verde L., 2011, J. Cosmol. Astropart. Phys., 11, 19
Gil-Marín H., Wagner C., Fragkoudi F., Jimenez R., Verde L., 2012a, J. Cosmol. Astropart. Phys., 2, 47
Gil-Marín H., Wagner C., Verde L., Porciani C., Jimenez R., 2012b, J. Cosmol. Astropart. Phys., 11, 29 (2L-RPT)
Gil-Marín H. et al., 2014a, preprint (arXiv:1408.0027)
Gil-Marín H., Wagner C., Noreña J., Verde L., Percival W., 2014b, J. Cosmol. Astropart. Phys., 12, 29
Goroff M. H., Grinstein B., Rey S.-J., Wise M. B., 1986, ApJ, 311, 6
Groth E. J., Peebles P. J. E., 1977, ApJ, 217, 385

Gunn J. E. et al., 1998, AJ, 116, 3040
Gunn J. E. et al., 2006, AJ, 131, 2332
Heavens A. F., Matarrese S., Verde L., 1998, MNRAS, 301, 797
Jain B., Bertschinger E., 1994, ApJ, 431, 495
Jing Y. P., Börner G., 2004, ApJ, 607, 140
Kaiser N., 1987, MNRAS, 227, 1
Kamionkowski M., Buchalter A., 1999, ApJ, 514, 7
Lewis A., Bridle S., 2002, Phys. Rev. D, 66, 103511
McDonald P., Roy A., 2009, J. Cosmol. Astropart. Phys., 8, 20
Makino N., Sasaki M., Suto Y., 1992, Phys. Rev. D, 46, 585
Manera M., Gaztañaga E., 2011, MNRAS, 415, 383
Manera M. et al., 2013, MNRAS, 428, 1036
Marín F., 2011, ApJ, 737, 97
Marín F. A. et al., 2013, MNRAS, 432, 2654
Matarrese S., Verde L., Heavens A. F., 1997, MNRAS, 290, 651
Matsubara T., 2007, ApJS, 170, 1
Nishimichi T., Taruya A., 2011, Phys. Rev. D, 84, 043526
Peebles P. J. E., Groth E. J., 1975, ApJ, 196, 1
Percival W. J., Verde L., Peacock J. A., 2004, MNRAS, 347, 645
Percival W. J. et al., 2014, MNRAS, 439, 2531
Planck Collaboration XVI 2014, A&A, 571, A16
Pollack J. E., Smith R. E., Porciani C., 2014, MNRAS, 440, 555
Press W. H., Teukolsky S. A., Vetterling W. T., Flannery B. P., 1992, Numerical recipes in FORTRAN, the art of scientific computing. Cambridge Univ. Press, Cambridge
Ross A. J. et al., 2013, MNRAS, 428, 1116
Saito S., Baldauf T., Vlah Z., Seljak U., Okumura T., McDonald P., 2014, preprint (arXiv:1405.1447)
Samushia L. et al., 2014, MNRAS, 439, 3504
Sánchez A. G. et al., 2014, MNRAS, 440, 2692
Saunders W. et al., 2000, MNRAS, 317, 55
Scoccimarro R., 2000, ApJ, 544, 597
Scoccimarro R., Couchman H. M. P., 2001, MNRAS, 325, 1312
Scoccimarro R., Colombi S., Fry J. N., Frieman J. A., Hivon E., Melott A., 1998, ApJ, 496, 586
Scoccimarro R., Couchman H. M. P., Frieman J. A., 1999, ApJ, 517, 531
Scoccimarro R., Feldman H. A., Fry J. N., Frieman J. A., 2001, ApJ, 546, 652
Smee S. A. et al., 2013, AJ, 146, 32
Smith J. A. et al., 2002, AJ, 123, 2121
Springel V., 2005, MNRAS, 364, 1105
Taruya A., Nishimichi T., Saito S., 2010, Phys. Rev. D, 82, 063522
Tegmark M., 1997, Phys. Rev. Lett., 79, 3806
Verde L., Heavens A. F., Matarrese S., Moscardini L., 1998, MNRAS, 300, 747
Verde L. et al., 2002, MNRAS, 335, 432
Verde L., Jimenez R., Alvarez-Gaume L., Heavens A. F., Matarrese S., 2013, J. Cosmol. Astropart. Phys., 6, 23
Wang Y., Yang X., Mo H. J., van den Bosch F. C., Chu Y., 2004, MNRAS, 353, 287
White M. et al., 2011, ApJ, 728, 126
Yamamoto K., Nakamichi M., Kamino A., Bassett B. A., Nishioka H., 2006, PASJ, 58, 93

APPENDIX A: SHOT NOISE FOR WEIGHED GALAXY MOCK CATALOGUES

In this appendix, we propose a formalism to incorporate the completeness weights in the Poisson shot noise terms of the FKP-estimator. The formalism itself is general enough that can be applied to any galaxy catalogue with completeness weights. However, the values for the x_i parameters of equations (A7), (A16) and (A19) must be calibrated to match the unweighted galaxy power spectrum for the specific mocks (here we use Manera et al. 2013).

According to the FKP-estimator, the Poisson shot noise contribution for the unweighted field F_2 (see equation 8) is given by

$$P_{\rm noise}^{\rm nw} = I_2^{-1} \int {\rm d}\boldsymbol{r}\, \langle n \rangle(\boldsymbol{r}) \left[1 + \alpha^{-1}\right]. \tag{A1}$$

where α is the ratio between the number of galaxies in the survey and the number in the synthetic random catalogue. When the completeness weights $w_{\rm c}$ (and systematic weights $w_{\rm sys}$) are introduced into the formalism, the shot noise depends on them. In this appendix, we assume that the systematic weights do not modify the shot noise when they are added. This behaviour is expected from the fact that, although the correction is not random, is related to a Poisson process, such as the presence of a galaxy around a star (see Section 2.1 for details). On the other hand, recall that the completeness weights are included to take into account galaxies whose radial position (redshift) is unknown. For the CMASS DR11 sample this can arise, for instance, because of fibre collisions and redshift failures (see Section 2.1 for a complete discussion). In the end, the effect of the completeness weighting process is to remove the affected galaxy and to upweight a nearby one. The

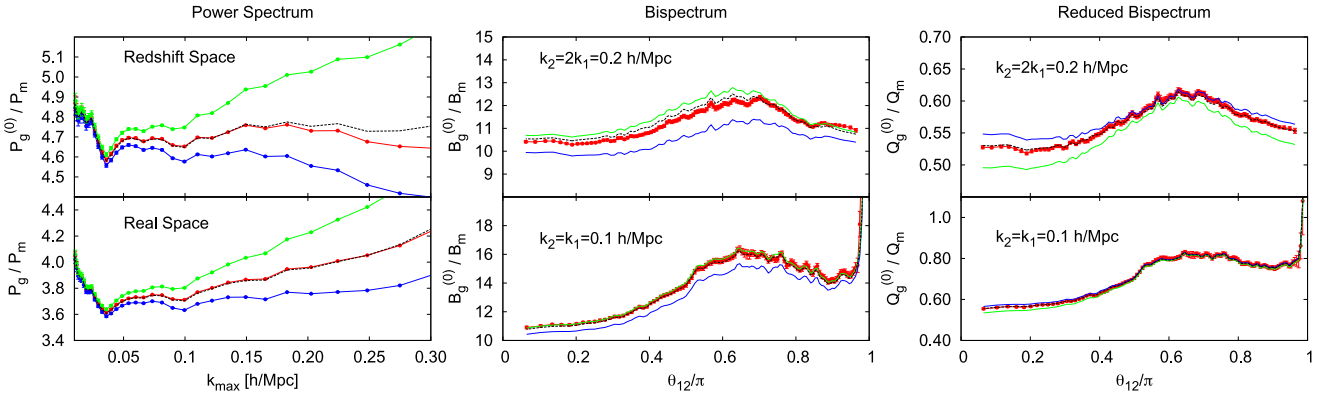

Figure A1. Left-hand panel: the power spectrum normalized by the non-linear matter (convolved with the corresponding window) for the unweighted galaxy mocks (red line) and for the weighted mocks with a subtraction according to $P_{\rm noise}^{\rm (false\,pairs)}$ (blue line) and $P_{\rm noise}^{\rm (true\,pairs)}$ (green line). Our proposed model of equation (A7) is shown in dashed black line for $x_{\rm PS} = 0.58$ and is able to accurately describe the unweighted galaxy mocks for the $k \lesssim 0.20\,h\,{\rm Mpc}^{-1}$. As labelled, the upper panel presents redshift-space quantities and the lower panel the real space value. The central and right-hand panels show the redshift-space monopole of the bispectrum and reduced bispectrum, respectively, normalized by the non-linear matter bispectrum model of equation (25), for two different shapes, $k_1/k_2 = 1, 2$, as labelled. The colour notation is the same as in the left-hand panels. In this case, the black line represents our proposed model of equation (A16) with $x_{\rm Bis} = 0.2$ and equation (A19) with $x_{\rm Q} = 0.66$ for the reduced bispectrum. Also for the bispectrum, our proposed model describe accurately the unweighted measurements.

missing and the up-weighted galaxies are angularly close, but we do not know if they are a true pair or just a chance alignment. If all of these angular pairs were true pairs, the weighting process would not modify the large-scale shot noise, in the same way that a smoothing filter of the galaxy field does not change the large-scale shot noise. In this case, if we assume that the shot noise is Poisson, the correlation function of the weighted number density of galaxies would read

$$\langle w_{\rm c}(\boldsymbol{r}_1)n(\boldsymbol{r}_1)w_{\rm c}(\boldsymbol{r}_2)n(\boldsymbol{r}_2)\rangle = \langle w_{\rm c}n\rangle(\boldsymbol{r}_1)\langle w_{\rm c}n\rangle(\boldsymbol{r}_2)\left[1+\xi_{\rm gal}(\boldsymbol{r}_1-\boldsymbol{r}_2)\right] + w_{\rm sys}(\boldsymbol{r}_2)\langle w_{\rm c}n\rangle(\boldsymbol{r}_1)\delta^D(\boldsymbol{r}_1-\boldsymbol{r}_2), \tag{A2}$$

and therefore the corresponding shot noise term is

$$P_{\rm noise}^{\rm (true\,pairs)} = I_2^{-1}\int {\rm d}\boldsymbol{r}\; w_{\rm FKP}^2(\boldsymbol{r})\langle w_{\rm c}n\rangle(\boldsymbol{r})\left[w_{\rm sys}(\boldsymbol{r})+\alpha\right]. \tag{A3}$$

On the other hand, if all these angular pairs were not true pairs, the process of removing one and up-weighting the other introduces extra shot noise. In this case, the correlation function of galaxies would read

$$\langle w_{\rm c}(\boldsymbol{r}_1)n(\boldsymbol{r}_1)w_{\rm c}(\boldsymbol{r}_2)n(\boldsymbol{r}_2)\rangle = \langle w_{\rm c}n\rangle(\boldsymbol{r}_1)\langle w_{\rm c}n\rangle(\boldsymbol{r}_2)\left[1+\xi_{\rm gal}(\boldsymbol{r}_1-\boldsymbol{r}_2)\right] + w_{\rm c}(\boldsymbol{r}_2)\langle w_{\rm c}n\rangle(\boldsymbol{r}_1)\delta^D(\boldsymbol{r}_1-\boldsymbol{r}_2), \tag{A4}$$

and therefore the shot noise term is

$$P_{\rm noise}^{\rm (false\,pairs)} = I_2^{-1}\int {\rm d}\boldsymbol{r}\; w_{\rm FKP}^2(\boldsymbol{r})\langle w_{\rm c}n\rangle(\boldsymbol{r})\left[w_{\rm c}(\boldsymbol{r})+\alpha\right]. \tag{A5}$$

We can write these two extreme cases in a more compact way,

$$P_{\rm noise}^{(i)} = I_2^{-1}\int {\rm d}\boldsymbol{r}\; w_{\rm FKP}^2(\boldsymbol{r})\langle w_{\rm c}n\rangle(\boldsymbol{r})\left[w_i(\boldsymbol{r})+\alpha\right], \tag{A6}$$

where i can be 'true pairs' and w_i is $w_{\rm sys}$, or i corresponds to 'false pairs' and w_i is $w_{\rm c}$. Reality will be an intermediate case where a fraction of the missing galaxies are true pairs and the rest are chance alignments. We propose a parametrization of the effective shot noise as

$$P_{\rm noise} = x_{\rm PS}\,P_{\rm noise}^{\rm (false\,pairs)} + (1-x_{\rm PS})\,P_{\rm noise}^{\rm (true\,pairs)}, \tag{A7}$$

where $x_{\rm PS}$ is a free parameter between 0 and 1 to be fitted from the galaxy mocks.

In the left-hand panel of Fig. A1, we show the comparison of these two shot noise predictions for the power spectrum of the galaxy mocks: unweighted galaxy power spectrum (red line), weighted galaxy power spectrum with the shot noise assumption of equation (A5, blue line), and weighted galaxy power spectrum with the shot noise assumption of equation (A3, green line). In this case, the galaxy power spectrum has been normalized by the non-linear matter power spectrum for clarity. For $x_{\rm PS} = 0.58$, our proposed *ansatz* of equation (A7) produces a good fit to the unweighted true distribution (black dotted lines) up to $k_{\rm max} \sim 0.18\,h\,{\rm Mpc}^{-1}$ in redshift space (much larger k in real space). This result indicates that the maximum k for our final joint power spectra and bispectra analysis should be close to and not be much larger than this value.

The same argument used for the power spectrum can be applied to the bispectrum. The unweighted quantity for the shot noise when is assumed Poisson is given by

$$B^{\rm nw}_{\rm noise}(\boldsymbol{k}_1,\boldsymbol{k}_2) = \frac{I_2}{I_3}\int \frac{{\rm d}\boldsymbol{k}'}{(2\pi)^3}\, P_{\rm gal}(\boldsymbol{k}')|W^{\rm nw}_2(\boldsymbol{k}_1-\boldsymbol{k}')|^2 + {\rm cyc.} + {\rm I}_3^{-1}\int {\rm d}\boldsymbol{r}\,\langle {\rm n}\rangle(\boldsymbol{r})\left[1-\alpha^2\right], \tag{A8}$$

with

$$W^{\rm nw}_2(\boldsymbol{k}) \equiv I_2^{-1/2}\int {\rm d}^3\boldsymbol{r}\,\langle n\rangle(\boldsymbol{r}){\rm e}^{+i\boldsymbol{k}\cdot\boldsymbol{r}}. \tag{A9}$$

As before, the (Poisson) shot noise contribution for the bispectrum depends on whether the angular triplets are true triplets or not (note that for simplicity we do not consider mix triplets between true and false). Expanding this expression produces

$$B^{(i)}_{\rm noise}(\boldsymbol{k}_1,\boldsymbol{k}_2) = \frac{I_2}{I_3}\int \frac{{\rm d}\boldsymbol{k}'}{(2\pi)^3}\, P_{\rm gal}(\boldsymbol{k}')W^*_2(\boldsymbol{k}_1-\boldsymbol{k}')\widetilde{W}^{(i)}_2(\boldsymbol{k}_1-\boldsymbol{k}') + {\rm cyc.} + {\rm I}_3^{-1}\int {\rm d}\boldsymbol{r}\,\langle {\rm w_c n}\rangle(\boldsymbol{r}){\rm w}^3_{\rm FKP}(\boldsymbol{r})\left[{\rm w}^2_{\rm i}(\boldsymbol{r})-\alpha^2\right], \tag{A10}$$

where we have introduced $\widetilde{W}^{(i)}_2$ as

$$\widetilde{W}^{(i)}_2(\boldsymbol{k}) \equiv I_2^{-1/2}\int {\rm d}^3\boldsymbol{r}\, w^2_{\rm FKP}(\boldsymbol{r})w_i(\boldsymbol{r})\langle w_{\rm c} n\rangle(\boldsymbol{r}){\rm e}^{+i\boldsymbol{k}\cdot\boldsymbol{r}}, \tag{A11}$$

and W_2 is the same as defined in equation (9),

$$W_2(\boldsymbol{k}) \equiv I_2^{-1/2}\int {\rm d}^3\boldsymbol{r}\, w_{\rm FKP}(\boldsymbol{r})\langle w_{\rm c} n\rangle(\boldsymbol{r}){\rm e}^{+i\boldsymbol{k}\cdot\boldsymbol{r}}. \tag{A12}$$

Our goal is to write equation (A10) as a function of the measured power spectrum. We define

$$\mathcal{A}^{(i)} \equiv \int {\rm d}\boldsymbol{r}\,\langle w_i(\boldsymbol{r})n_g(\boldsymbol{r})\rangle^2(\boldsymbol{r})w_i(\boldsymbol{r})w^3_{\rm FKP}, \tag{A13}$$

which provides the normalization for the power spectrum convolution of equation (A10). Thus, we can perform the approximation,

$$\frac{I_2}{\mathcal{A}^{(i)}}\int \frac{{\rm d}\boldsymbol{k}'}{(2\pi)^3}\, P_{\rm gal}(\boldsymbol{k}')W^*_2(\boldsymbol{k}-\boldsymbol{k}')\widetilde{W}^{(i)}_2(\boldsymbol{k}-\boldsymbol{k}') \simeq \int \frac{{\rm d}\boldsymbol{k}'}{(2\pi)^3}\, P_{\rm gal}(\boldsymbol{k}')|W_2(\boldsymbol{k}-\boldsymbol{k}')|^2 = \langle|F_2(\boldsymbol{k})|^2\rangle - P^{(i)}_{\rm noise}, \tag{A14}$$

which should be an accurate assumption, especially at small scales where the shot noise term is important. Thus, finally we write equation (A10) in terms of the measured power spectrum $\langle|F_2(\boldsymbol{k})|^2\rangle$,

$$B^{(i)}_{\rm noise}(\boldsymbol{k}_1,\boldsymbol{k}_2) = \frac{\mathcal{A}^{(i)}}{I_3}\left[\langle|F_2(\boldsymbol{k}_1)|^2\rangle + {\rm cyc.} - 3P^{(i)}_{\rm noise}\right] + I_3^{-1}\int {\rm d}\boldsymbol{r}\,\langle w_{\rm c} n\rangle(\boldsymbol{r})w^3_{\rm FKP}(\boldsymbol{r})\left[w^2_i(\boldsymbol{r})-\alpha^2\right]. \tag{A15}$$

In a similar approach as was used for the power spectrum, we can approximate the effective (Poisson) shot noise term for the bispectrum as

$$B_{\rm noise}(\boldsymbol{k}_1,\boldsymbol{k}_2) = x_{\rm Bis}B^{(\text{false triplets})}_{\rm noise}(\boldsymbol{k}_1,\boldsymbol{k}_2) + (1-x_{\rm Bis})B^{(\text{true triplets})}_{\rm noise}(\boldsymbol{k}_1,\boldsymbol{k}_2). \tag{A16}$$

Finally, combining the shot noise terms obtained for the power spectrum and bispectrum, we can write the (Poisson) shot noise terms for the reduced bispectrum Q as

$$Q^{\rm nw}_{\rm noise}(k_1,k_2,k_3) = \frac{B^{\rm nw}_{\rm noise}(k_1,k_2,k_3)}{[P(k_1)-P^{\rm nw}_{\rm noise}][P(k_2)-P^{\rm nw}_{\rm noise}]+{\rm cyc.}}, \tag{A17}$$

$$Q^{(i)}_{\rm noise}(k_1,k_2,k_3) = \frac{B^{(i)}_{\rm noise}(k_1,k_2,k_3)}{[P(k_1)-P^{(i)}_{\rm noise}][P(k_2)-P^{(i)}_{\rm noise}]+{\rm cyc.}}, \tag{A18}$$

and therefore the effective term of the Poisson shot noise for the reduced bispectrum is

$$Q_{\rm noise}(\boldsymbol{k}_1,\boldsymbol{k}_2) = x_{\rm Q}Q^{(\text{false triplets})}_{\rm noise}(\boldsymbol{k}_1,\boldsymbol{k}_2) + (1-x_{\rm Q})Q^{(\text{true triplets})}_{\rm noise}(\boldsymbol{k}_1,\boldsymbol{k}_2). \tag{A19}$$

In the central panel of Fig. A1, we show the redshift-space monopole galaxy bispectrum (normalized by the corresponding non-linear matter bispectrum) of the unweighed galaxy catalogue with the shot noise subtraction of equation (A8, red), and for the weighed galaxy catalogue when the shot noise term subtracted is $B^{(\text{false triplets})}_{\rm noise}$ (blue lines) and $B^{(\text{true triplets})}_{\rm noise}$ (green lines). The black dashed lines display the interpolated model of equation (A16) with the fitted value $x_{\rm Bis} = 0.20$. The top panel presents the bispectrum for the shape $k_2/k_1 = 2$, whereas the bottom panel for $k_2/k_1 = 1$ as indicated. In the right-hand panel, the same formalism applied to the reduced bispectrum Q. In this case, the interpolation parameter has been set to $x_Q = 0.66$. Note that x_Q could be in principle related to x_P and x_B, since Q, P and B are related. However, this relation is far from being simple as equation (A19) and the functional between $Q_{\rm noise}$, $Q^{(\text{false triplets})}_{\rm noise}$ and $Q^{(\text{true triplets})}_{\rm noise}$ is not linear. In this paper, we have tried a linear relation, treating x_Q as a free parameter. Given that the performance of x_Q in Fig. A1 seems pretty similar to x_B, we assume that equation (A19) is a good approximation of the full relation given by x_B and x_P.

Table A1. Interpolation values x_P, x_B, x_Q used for the shot noise weighted statistics.

	$x_{(P,\,B,\,Q)}$	Equation
P	0.58	A7
B	0.20	A16
Q	0.66	A19

To conclude, in this paper we always assume that the Poisson shot noise prediction of the weighted galaxy catalogues by Manera et al. (2013) is given by equations (A7), (A16) and (A19) with the values summarized in Table A1.

APPENDIX B: POWER SPECTRUM IN REDSHIFT SPACE

In this appendix, we specify the formulae we use to compute the galaxy power spectrum in redshift space. The full formulae derivation can be found in the papers cited by the equations. The starting point is the non-local bias model given in equation (17). From there we obtain the real space power spectrum

$$P_{g,\delta\delta}(k) = b_1^2 P_{\delta\delta}(k) + 2b_2 b_1 P_{b2,\delta}(k) + 2b_{s^2} b_1 P_{bs2,\delta}(k) + b_2^2 P_{b22}(k) + 2b_2 b_{s^2} P_{b2s2}(k) + b_{s^2}^2 P_{bs22}(k) + 2b_1 b_{3\rm nl}\sigma_3^2(k) P^{\rm lin}(k), \tag{B1}$$

where $P_{\delta\delta}$ and $P^{\rm lin}$ are the non-linear and linear matter power spectra. The power spectra that multiply the bias parameters b_2 and b_s can be given by the following one-loop integrals (McDonald & Roy 2009; Beutler et al. 2014),

$$P_{b2,\delta} = \int \frac{{\rm d}^3 q}{(2\pi)^3}\, P^{\rm lin}(q) P^{\rm lin}(|\boldsymbol{k}-\boldsymbol{q}|) \mathcal{F}_2^{\rm SPT}(\boldsymbol{q}, \boldsymbol{k}-\boldsymbol{q}), \tag{B2}$$

$$P_{bs2,\delta} = \int \frac{{\rm d}^3 q}{(2\pi)^3}\, P^{\rm lin}(q) P^{\rm lin}(|\boldsymbol{k}-\boldsymbol{q}|) \mathcal{F}_2^{\rm SPT}(\boldsymbol{q}, \boldsymbol{k}-\boldsymbol{q}) S_2(\boldsymbol{q}, \boldsymbol{k}-\boldsymbol{q}), \tag{B3}$$

$$P_{b2s2} = -\frac{1}{2}\int \frac{{\rm d}^3 q}{(2\pi)^3}\, P^{\rm lin}(q) \left[\frac{2}{3} P^{\rm lin}(q) - P^{\rm lin}(|\boldsymbol{q}-\boldsymbol{k}|) S_2(\boldsymbol{q}, \boldsymbol{k}-\boldsymbol{q})\right], \tag{B4}$$

$$P_{bs22} = -\frac{1}{2}\int \frac{{\rm d}^3 q}{(2\pi)^3}\, P^{\rm lin}(q) \left[\frac{4}{9} P^{\rm lin}(q) - P^{\rm lin}(|\boldsymbol{k}-\boldsymbol{q}|) S_2(\boldsymbol{q}, \boldsymbol{k}-\boldsymbol{q})^2\right], \tag{B5}$$

$$P_{b22} = -\frac{1}{2}\int \frac{{\rm d}^3 q}{(2\pi)^3}\, P^{\rm lin}(q) \left[P^{\rm lin}(q) - P^{\rm lin}(\boldsymbol{k}-\boldsymbol{q}|)\right], \tag{B6}$$

$$\sigma_3^2(k) = \int \frac{{\rm d}^3 \boldsymbol{q}}{(2\pi)^3}\, P^{\rm lin}(q) \left[\frac{5}{6} + \frac{15}{8} S_2(\boldsymbol{q}, \boldsymbol{k}-\boldsymbol{q}) S_2(-\boldsymbol{q}, \boldsymbol{k}) - \frac{5}{4} S_2(\boldsymbol{q}, \boldsymbol{k}-\boldsymbol{q})\right]. \tag{B7}$$

The S_2 kernel is given in equation (19) and the $\mathcal{F}_2^{\rm SPT}$ kernel (e.g. Goroff et al. 1986; Catelan & Moscardini 1994a,b and Bernardeau et al. 2002 for a review) is given by

$$\mathcal{F}_2^{\rm SPT}(\boldsymbol{k}_i, \boldsymbol{k}_j) = \frac{5}{7} + \frac{1}{2}\frac{\boldsymbol{k}_i \cdot \boldsymbol{k}_j}{k_i k_j}\left(\frac{k_i}{k_j} + \frac{k_j}{k_i}\right) + \frac{2}{7}\left[\frac{\boldsymbol{k}_i \cdot \boldsymbol{k}_j}{k_i k_j}\right]^2. \tag{B8}$$

These integrals can be reduced to two-dimensional integrals due to rotational invariance of the linear power spectrum. These contributions are illustrated in the left-hand panel of Fig. B1.

To obtain the redshift-space power spectrum, we also need the terms $P_{g\theta}$ and $P_{\theta\theta}$. Since we assume no velocity bias, $P_{\theta\theta}$ is the same for non-linear matter and galaxies,

$$P_{g\theta}(k) = b_1 P_{\delta\theta}(k) + b_2 P_{b2,\theta}(k) + b_{s^2} P_{bs2,\theta}(k) + b_{3\rm nl}\sigma_3^2(k) P^{\rm lin}(k), \tag{B9}$$

where $P_{\delta\theta}$ is the matter density–velocity non-linear power spectrum, and the other two terms are given by one-loop integrals,

$$P_{b2,\theta}(k) = \int \frac{{\rm d}^3 q}{(2\pi)^3}\, P^{\rm lin}(q) P^{\rm lin}(|\boldsymbol{k}-\boldsymbol{q}|) \mathcal{G}_2^{\rm SPT}(\boldsymbol{q}, \boldsymbol{k}-\boldsymbol{q}), \tag{B10}$$

$$P_{bs2,\theta}(k) = \int \frac{{\rm d}^3 q}{(2\pi)^3}\, P^{\rm lin}(q) P^{\rm lin}(|\boldsymbol{k}-\boldsymbol{q}|) \mathcal{G}_2^{\rm SPT}(\boldsymbol{q}, \boldsymbol{k}-\boldsymbol{q}) S_2(\boldsymbol{q}, \boldsymbol{k}-\boldsymbol{q}). \tag{B11}$$

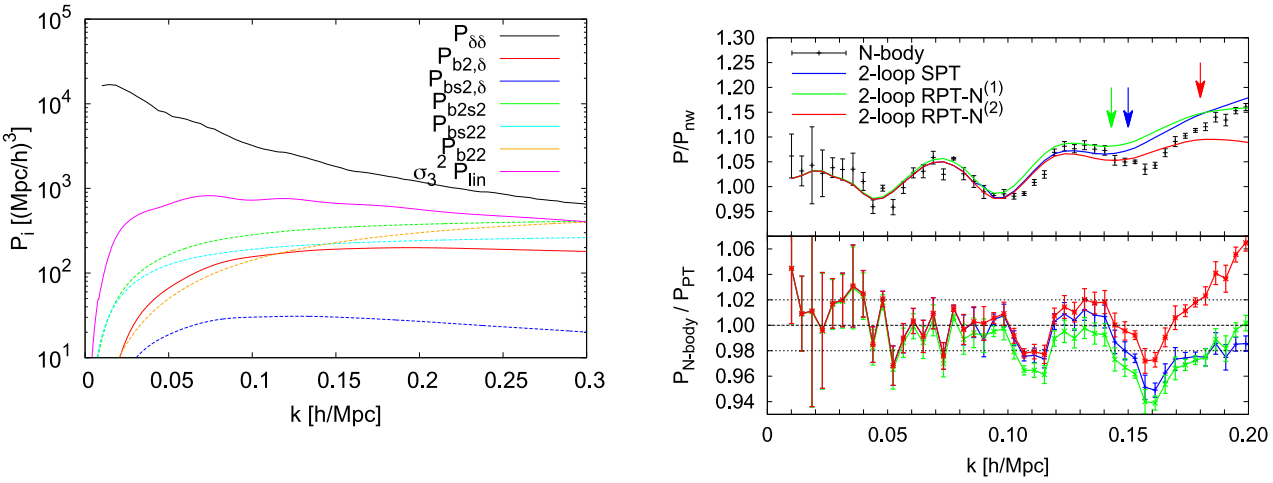

Figure B1. Left-hand panel: the different contributions of equations (B2)–(B7). Right-hand panel: perturbation theory and N-body simulation predictions for the dark matter power spectrum $P_{\delta\delta}$. The top panel displays the actual power spectrum normalized by a non-wiggle linear model for clarity. Bottom panel shows the relative difference of each PT model to the N-body simulations. Blue lines correspond to SPT, green lines to RPT-$\mathcal{N}^{(1)}$ and red lines to RPT-$\mathcal{N}^{(2)}$. The arrows indicate where each model starts to deviate with respect to N-body mocks higher than 2 per cent. The cosmology chosen is the same of the galaxy mocks described in Section 2.2 at $z = 0.55$. The errors of N-body correspond to the error of the mean among five different realizations, with a total effective volume of $V_{\rm eff} = 16.875\,{\rm Mpc}\,h^{-1}$.

The $\mathcal{G}_2^{\rm SPT}$ kernels are (Goroff et al. 1986; Catelan & Moscardini 1994a,b)

$$\mathcal{G}_2^{\rm SPT}(\boldsymbol{k}_i, \boldsymbol{k}_j) = \frac{3}{7} + \frac{1}{2}\frac{\boldsymbol{k}_i \cdot \boldsymbol{k}_j}{k_i k_j}\left(\frac{k_i}{k_j} + \frac{k_j}{k_i}\right) + \frac{4}{7}\left[\frac{\boldsymbol{k}_i \cdot \boldsymbol{k}_j}{k_i k_j}\right]^2 . \tag{B12}$$

The kernels $\mathcal{F}_2^{\rm SPT}$ and $\mathcal{G}_2^{\rm SPT}$ have only weak cosmology dependence (Bouchet et al. 1992; Bernardeau 1994; Catelan et al. 1995; Eisenstein 1997; Matarrese et al. 1997; Kamionkowski & Buchalter 1999). Once we have the real space quantities, P_{gg}, $P_{g\theta}$ and $P_{\theta\theta}$, the redshift-space power spectrum can be written using the mapping provided by Taruya et al. (2010) and Nishimichi & Taruya (2011),

$$P_g^{(s)}(k,\mu) = D_{\rm FoG}^P(k,\mu,\sigma_{\rm FoG}^P[z])\left[P_{g,\delta\delta}(k) + 2f\mu^2 P_{g,\delta\theta}(k) + f^2\mu^4 P_{\theta\theta}(k) + b_1^3 A^{\rm TNS}(k,\mu,f/b_1) + b_1^4 B^{\rm TNS}(k,\mu,f/b_1)\right], \tag{B13}$$

where $A^{\rm TNS}$ and $B^{\rm TNS}$ are correction terms arising from the coupling between the Kaiser and the FoG effects. The expression of these terms (to leading order for the bias) is given in Taruya et al. (2010),

$$A^{\rm TNS}(k,\mu,b) = (k\mu f)\int \frac{{\rm d}^3\boldsymbol{q}}{(2\pi)^3}\frac{q_z}{q^2}\left\{B_\sigma(\boldsymbol{q},\boldsymbol{k}-\boldsymbol{q},-\boldsymbol{k}) - B_\sigma(\boldsymbol{q},\boldsymbol{k},-\boldsymbol{k}-\boldsymbol{q})\right\}, \tag{B14}$$

$$B^{\rm TNS}(k,\mu,b) = (k\mu f)^2\int \frac{{\rm d}^3\boldsymbol{q}}{(2\pi)^3}F^{\rm TNS}(\boldsymbol{q})F^{\rm TNS}(\boldsymbol{k}-\boldsymbol{q}), \tag{B15}$$

where,

$$F^{\rm TNS}(\boldsymbol{q}) \equiv \frac{q_z}{q^2}\left\{b_1 P_{\delta\theta}(q) + f\frac{q_z^2}{q^2}P_{\theta\theta}(q)\right\}, \tag{B16}$$

and

$$(2\pi)^3\delta_D(\boldsymbol{k}_{123})B_\sigma(\boldsymbol{k}_1,\boldsymbol{k}_2,\boldsymbol{k}_3) \equiv \left\langle\theta(\boldsymbol{k}_1)\left\{b_1\delta(\boldsymbol{k}_2) + f\frac{k_{2z}^2}{k_2^2}\theta(\boldsymbol{k}_2)\right\}\left\{b_1\delta(\boldsymbol{k}_3) + f\frac{k_{3z}^2}{k_3^2}\theta(\boldsymbol{k}_3)\right\}\right\rangle, \tag{B17}$$

with $\boldsymbol{k}_{123} \equiv \boldsymbol{k}_1 + \boldsymbol{k}_2 + \boldsymbol{k}_3$. Since we expect $A^{\rm TNS}$ and $B^{\rm TNS}$ to be small compared to $P_{\delta\delta}$, $P_{\delta\theta}$ and $P_{\theta\theta}$, we have assumed that only the leading terms for the galaxy power spectrum and bispectrum contribute in the integrals of equations (B14) and (B15). In other words, $P_{\delta\delta}$, $P_{\delta\theta}$ and $P_{\theta\theta}$ are approximated by $P^{\rm lin}$ and $B_{\delta\delta\theta}$, $B_{\delta\theta\theta}$, $B_{\theta\theta\theta}$ by the corresponding tree level quantities in equations (B14) and (B15).

The function $D_{\rm FoG}^P$ accounts for the fully non-linear damping due to the velocity dispersion of satellite galaxies inside the host halo which we parametrize through a one-free parameter Lorentzian distribution,

$$D_{\rm FoG}^P(k,\mu,\sigma_{\rm FoG}^P[z]) = \left(1 + k^2\mu^2\sigma_{\rm FoG}^P[z]^2/2\right)^{-2}. \tag{B18}$$

We must specify the procedure to compute the non-linear matter power spectra, $P_{\delta\delta}$, $P_{\delta\theta}$ and $P_{\theta\theta}$. One option would be to run a suite of N-body simulations and measure these quantities *in situ*. However, if we want to change the cosmology we would need to re-run simulations with the new cosmological parameters, which would be prohibitively expensive. More importantly, the quantities that involves the θ-field need are delicate to compute as there are many grid-cells with no particles (Voronoi tessellation methods can be used to address this issue).

Here, we adopt the approach of using analytical expressions based on perturbation theory. According to SPT, the two-loop prediction for the power spectrum reads (e.g. see Makino, Sasaki & Suto 1992; Jain & Bertschinger 1994 for the first pioneering studies)

$$P_{ij}^{\rm SPT}(k) = P^{\rm lin}(k) + 2P_{ij}^{(13)}(k) + P_{ij}^{(22)}(k) + 2P_{ij}^{(15)}(k) + 2P_{ij}^{(24)}(k) + P_{ij}^{(33)}(k) \tag{B19}$$

with the compact notation where i and j can be δ and θ. The terms $P_{ij}^{(13)}$, $P_{ij}^{(22)}$, $P_{ij}^{(15)}(k)$, $P_{ij}^{(24)}$ and $P_{ij}^{(33)}$ can be found in the references above and any perturbation theory review (see for e.g. Bernardeau et al. 2002 among many others). Crocce & Scoccimarro (2006) proposed a reorganization of the infinite terms of the SPT series and a resummation of part of them in what is called the *resummed propagator*. In this formalism, the behaviour when truncating the infinite series at certain loop improves moderately with respect to SPT. According to this RPT, at two-loop truncation the power spectrum reads

$$P_{ij}^{\rm RPT}(k) = [P^{\rm lin}(k,z) + P_{ij}^{(22)}(k,z) + P_{ij}^{(33)\,-2{\rm L}}(k,z)]\,\mathcal{N}_{ij}^{(i)}, \tag{B20}$$

where $P_{ij}^{(33)\,-2{\rm L}}$ is the part of $P_{ij}^{(33)}$ that accounts for the full two-loop coupling, and $\mathcal{N}_{ij}$ is the resummed propagator. The full expression of the resummed propagator $\mathcal{N}$ depends on how all the infinite terms of the series have been approximated just before the resummation. When these terms are resummed using one-loop kernels, we refer to the resummed propagator as $\mathcal{N}^{(1)}$. However, the propagator can also be resummed using higher order loop kernels. In general, we refer to the resummed propagator using ℓ-loop kernels as, $\mathcal{N}^{(\ell)}$. The expressions for one- and two-loop can be found, respectively, in Crocce & Scoccimarro (2006) and Gil-Marín et al. (2012b) and read

$$\mathcal{N}_{ij}^{(1)}(k) \equiv \exp\left[P_{ij}^{(13)}(k)/P^{\rm lin}(k)\right], \tag{B21}$$

$$\mathcal{N}_{ij}^{(2)}(k) \equiv \cosh\left[\sqrt{\frac{2P_{ij}^{(15)}(k)}{P^{\rm lin}(k)}}\right] + \frac{P_{ij}^{(13)}(k)}{P^{\rm lin}(k)}\sqrt{\frac{P^{\rm lin}(k)}{2P_{ij}^{(15)}(k)}}\sinh\left[\sqrt{\frac{2P_{ij}^{(15)}(k)}{P^{\rm lin}(k)}}\right]. \tag{B22}$$

The order at which we approximate the resummed propagator has nothing to do with the order of truncation of the infinite series of the remaining (non-resummed) terms, which is something done after the resummation process.

In Fig. B1, we show the performance of these different approximation schemes for the matter power spectrum: two-loop SPT (blue lines), two-loop RPT-$\mathcal{N}^{(1)}$ (green lines) and two-loop RPT-$\mathcal{N}^{(2)}$ (red lines). The matter power spectrum at $z = 0.55$ from N-body simulations (described in Section 2.2) is indicated by the black symbols; the cosmology is the same as the mock catalogues. The top panel displays the different power spectra normalized by a non-wiggle linear power spectrum for clarity. The bottom panel presents the relative difference to N-body predictions. The arrows indicate where every model starts to deviate more than 2 per cent with respect to N-body simulation measurements. For SPT and RPT-$\mathcal{N}^{(1)}$, this happens at about $k \simeq 0.15\,h\,{\rm Mpc}^{-1}$, whereas RPT-$\mathcal{N}^{(2)}$ is able to describe N-body result up to $k \simeq 0.18\,h\,{\rm Mpc}^{-1}$, within 2 per cent errors. Because of this effect, in this paper we choose RPT-$\mathcal{N}^{(2)}$ to compute P_{ij}. The observed behaviour in Fig. B1 indicates that our maximum k for the analysis might not be much larger than the values pointed by the arrows, as our description starts breaking down. For simplicity, in the rest of the paper we refer to RPT-$\mathcal{N}^{(2)}$ as 2L-RPT.

The redshift-space power spectrum depends on the angle with respect to the line of sight and thus can be expressed in the Legendre polynomials base,

$$P^{(s)}(k,\mu) = \sum_{\ell=0}^{\infty} P^{(\ell)}(k) L_\ell(\mu), \tag{B23}$$

where P_ℓ are the ℓ-order multipoles and L_ℓ are the Legendre polynomials. Most of the signal of the original $P^{(s)}$ function is contained in the first non-zero multipoles. In particular, at large scales, the only multipoles that are non-zero are $\ell = 0$ (monopole), $\ell = 2$ (quadrupole) and $\ell = 4$ (hexadecapole), but almost all the signal is contained in the first two terms. In this paper, we focus on the monopole. This is the only multipole whose Legendre polynomial is unitary, $L_0(\mu) = 1$, and therefore it does not depend on the orientation of the line of sight. Because of this, we can safely apply the FKP-estimator to measure it from the galaxy survey. Inverting equation (B23), we can express the multipoles as a function of $P^{(s)}$,

$$P_g^{(\ell)}(k) = \frac{2\ell+1}{2}\int_{-1}^{+1} {\rm d}\mu\; P_g^{(s)}(k,\mu) L_\ell(\mu). \tag{B24}$$

For $\ell = 0$, we obtain the monopole, $P_g^{(0)}$.

APPENDIX C: BISPECTRUM IN REAL AND REDSHIFT SPACE

According to perturbation theory, the leading order correction for the dark matter density- and velocity bispectrum can be expressed as a function of the linear power spectrum and the symmetrized two-point kernel (Fry 1994; Heavens et al. 1998; Scoccimarro et al. 1998; Verde et al. 1998),

$$B_\delta(\boldsymbol{k}_1,\boldsymbol{k}_2) = 2P^{\rm lin}(k_1)P^{\rm lin}(k_2)\mathcal{F}_2^{\rm SPT}(\boldsymbol{k}_1,\boldsymbol{k}_2) + {\rm cyc.} \tag{C1}$$

$$B_\theta(\boldsymbol{k}_1,\boldsymbol{k}_2) = 2P^{\rm lin}(k_1)P^{\rm lin}(k_2)\mathcal{G}_2^{\rm SPT}(\boldsymbol{k}_1,\boldsymbol{k}_2) + {\rm cyc.}, \tag{C2}$$

with the two-point kernel $\mathcal{F}_2^{\rm SPT}$ given by equation (B8) and the $\mathcal{G}_2^{\rm SPT}$ kernel by equation (B12). These formulae only reproduce the N-body predictions at the largest scales. The tree-level model of equation (C1) can be improved by substituting the linear power spectra by the non-linear correction and the $\mathcal{F}_2^{\rm SPT}$ kernel by an effective kernel $\mathcal{F}_2^{\rm eff}$, as initially proposed in Scoccimarro & Couchman (2001), improved in Gil-Marín et al. (2012a) and reported in equation (D1) in Appendix D. Similarly the tree-level equation (C2) can be improved and made valid into the (mildly)non-linear regime by introducing an effective kernel $\mathcal{G}_2^{\rm eff}$, described in Gil-Marín et al. (2014b) reported in equation (D3) in Appendix D.

These effective kernels do not show a strong dependence with cosmology or with z; the dependence of the bispectrum on cosmology and redshift is dominated by that of the power spectra. This model has shown a better description of the matter density-bispectrum up to mildly non-linear regime ($k \lesssim 0.2\,h\,{\rm Mpc}^{-1}$) at low redshifts ($z \leq 1.5$).

The galaxy-bispectrum can be written according to the bias model of equation (17) as

$$B_g(k_1,k_2,k_3) = b_1^3 B(k_1,k_2,k_3) + b_1^2\left[b_2 P(k_1)P(k_2) + b_{s^2}P(k_1)P(k_2)S_2(\boldsymbol{k}_1,\boldsymbol{k}_2) + {\rm cyc.}\right], \tag{C3}$$

where P and B are the non-linear matter power spectrum and bispectrum, respectively. We neglect the terms proportional to b_2^2, b_{s2}^2, which belong to higher order contributions. Applying the tree-level form for the matter bispectrum, we can write the real space galaxy bispectrum as a function of the non-linear matter power spectrum and the effective kernel,

$$B_g(k_1,k_2,k_3) = 2P(k_1)P(k_2)\left[b_1^3\mathcal{F}_2^{\rm eff}(\boldsymbol{k}_1,\boldsymbol{k}_2) + \frac{b_1^2 b_2}{2} + \frac{b_1^2 b_{s^2}}{2}S_2(\boldsymbol{k}_1,\boldsymbol{k}_2)\right] + {\rm cyc.} \tag{C4}$$

In this case, the non-local bias b_{s2} contributes to the leading order and introduces a new shape dependence through S_2, which was not present in the matter bispectrum. We do not consider the contribution of $b_{\rm 3nl}$ because for the bispectrum (in contrast to the power spectrum) it only appears in fourth and higher order corrections in δ_g.

We next derive the expression for the galaxy bispectrum in redshift space.

The mapping from the real space radial coordinate to the redshift-space radial coordinate depends on the Hubble flow and the Doppler effect due to the peculiar motions of particles, namely peculiar velocities $\boldsymbol{v}$. Under the distant observer approximation, the redshift-space coordinate $\boldsymbol{s}$ reads as

$$s = x + \frac{v_z(\boldsymbol{x})}{H(a)a}\hat{\boldsymbol{x}}_z, \tag{C5}$$

where v_z is the radial component of the velocity, a the scale factor and H the Hubble parameter. Using the scaled velocity field, $\boldsymbol{u} \equiv -\boldsymbol{v}/[H(a)af(a)]$, where f is the logarithmic grow factor, we write the mapping as

$$\boldsymbol{s} = \boldsymbol{x} - f u_z(\boldsymbol{x})\hat{\boldsymbol{x}}_z. \tag{C6}$$

According to this expression, we can express the Fourier space density contrast in redshift space as a function of the real space density contrast as

$$\delta^{(s)}(\boldsymbol{k}) = \int \frac{{\rm d}^3\boldsymbol{x}}{(2\pi)^3}\,{\rm e}^{-i\boldsymbol{k}\boldsymbol{I}}{\rm e}^{if k_z v_z(\boldsymbol{x})}\left[\delta(\boldsymbol{x}) + f\nabla_z v_z(\boldsymbol{x})\right], \tag{C7}$$

where just those points with $f\nabla_z u_z(9) < 1$ have been taken into account. Expanding the second exponential in power series, we can write the galaxy density contrast in redshift space as

$$\delta_g^{(s)}(\boldsymbol{x}) = \sum_{i=1}^{\infty}\int {\rm d}^3\boldsymbol{k}_1\ldots d^3\boldsymbol{k}_n\delta^D(\boldsymbol{k}-\boldsymbol{k}_1-\ldots\boldsymbol{k}_n)\delta_g(\boldsymbol{k}_1) + f\mu_1^2\theta(\boldsymbol{k}_1)\frac{(f\mu k)^{n-1}}{(n-1)!}\frac{\mu_2}{k_2}\theta(\boldsymbol{k}_2)\ldots\frac{\mu_n}{k_n}\theta(\boldsymbol{k}_n), \tag{C8}$$

where we have defined $\theta(\boldsymbol{k}) \equiv [-i\boldsymbol{k}\cdot\boldsymbol{v}]/[af(a)H(a)]$. We also have assumed an unbiased velocity bias relation for galaxies $\theta_g(\boldsymbol{k}) = \theta(\boldsymbol{k})$. Plugging the bias model of equation (17) and expanding perturbatively the dark matter and k-velocities overdensities we can re-write

$$\delta_g^s(\boldsymbol{k}) = \sum_{i=1}^{\infty}\int {\rm d}^3\boldsymbol{k}_1\ldots d^3\boldsymbol{k}_n\delta^D(\boldsymbol{k}-\boldsymbol{k}_1-\ldots\boldsymbol{k}_n)Z_n(\boldsymbol{k}_1,\ldots,\boldsymbol{k}_n)\delta^{(1)}(\boldsymbol{k}_1)\ldots\delta^{(1)}(\boldsymbol{k}_n), \tag{C9}$$

where the Z_i are the redshift-space i-loop kernels. The first two kernels read as

$$Z_1(\boldsymbol{k}_i) \equiv (b_1 + f\mu_i^2), \tag{C10}$$

$$Z_2(\boldsymbol{k}_1,\boldsymbol{k}_2) \equiv b_1\left[\mathcal{F}_2^{\rm SPT}(\boldsymbol{k}_1,\boldsymbol{k}_2) + \frac{f\mu k}{2}\left(\frac{\mu_1}{k_1}+\frac{\mu_2}{k_2}\right)\right] + f\mu^2\mathcal{G}_2^{\rm SPT}(\boldsymbol{k}_1,\boldsymbol{k}_2) + \frac{f^2\mu k}{2}\mu_1\mu_2\left(\frac{\mu_2}{k_1}+\frac{\mu_1}{k_2}\right) + \frac{b_2}{2} + \frac{b_{s^2}}{2}S_2(\boldsymbol{k}_1,\boldsymbol{k}_2), \tag{C11}$$

with $\mu_i \equiv 2_i\cdot\hat{x}_z/k_i$, $\mu \equiv (\mu_1 k_1 + \mu_2 k_2)/k$, $k^2 = (2_1 + ?_2)^2$; $\mathcal{F}_2^{\rm SPT}$ and $\mathcal{G}_2^{\rm SPT}$ are the second-order kernels of the densities and velocities, respectively (see equations B8 and B12).

The Z_i kernels play the same role as $\mathcal{F}_i$ but now in redshift space. Thus, the redshift-space galaxy bispectrum becomes

$$B_g^{(s)}(\boldsymbol{k}_1,\boldsymbol{k}_2) = 2P(k_1)\,Z_1(\boldsymbol{k}_1)\,P(k_2)\,Z_1(\boldsymbol{k}_2)\,Z_2(\boldsymbol{k}_1,\boldsymbol{k}_2) + \text{cyc.} \tag{C12}$$

For the unbiased case of dark matter without radial peculiar velocities ($b_1 = 1$ and $f = 0$), $Z_1 \to 1$ and $Z_2 \to \mathcal{F}_2^{\rm SPT}$, and we recover the tree-level expression in real space.

To extend this description more into the (mildly) non-linear regime, a FoG term can be added,

$$B_g^{(s)}(\boldsymbol{k}_1,\boldsymbol{k}_2) = D^B_{\rm FoG}(k_1,k_2,k_3,\sigma^B_{\rm FoG}[z])\left[2P(k_1)\,Z_1(\boldsymbol{k}_1)\,P(k_2)\,Z_1(\boldsymbol{k}_2)\,Z_2^{\rm eff}(\boldsymbol{k}_1,\boldsymbol{k}_2) + \text{cyc.}\right]. \tag{C13}$$

Similarly to what is done in real space, the redshift-space kernel Z_2 has been substituted by an effective kernel $Z_2^{\rm eff}$ of the form (Gil-Marín et al. 2014b),

$$Z_2^{\rm eff}(\boldsymbol{k}_1,\boldsymbol{k}_2) \equiv b_1\left[\mathcal{F}_2^{\rm eff}(\boldsymbol{k}_1,\boldsymbol{k}_2) + \frac{f\mu k}{2}\left(\frac{\mu_1}{k_1}+\frac{\mu_2}{k_2}\right)\right] + f\mu^2\mathcal{G}_2^{\rm eff}(\boldsymbol{k}_1,\boldsymbol{k}_2) + \frac{f^3\mu k}{2}\mu_1\mu_2\left(\frac{\mu_2}{k_1}+\frac{\mu_1}{k_2}\right) + \frac{b_2}{2} + \frac{b_{s^2}}{2}S_2(\boldsymbol{k}_1,\boldsymbol{k}_2), \tag{C14}$$

where $\mathcal{F}_2^{\rm eff}$ is given by equation (D1) and $\mathcal{G}_2^{\rm eff}$ by equation (D3).

In equation (C13), analogous to what was done for the power spectrum, we included $D^B_{\rm FoG}$: a damping term that aims to describe the FoG effect due to velocity dispersion inside virialized structures through one-free parameter, $\sigma^B_{\rm FoG}$. For the bispectrum, we parametrize this term as (see e.g. Verde et al. 1998; Scoccimarro, Couchman & Frieman 1999)

$$D^B_{\rm FoG}(k_1,k_2,k_3,\sigma^B_{\rm FoG}[z]) = \left(1 + [k_1^2\mu_1^2 + k_2^2\mu_2^2 + k_3^2\mu_3^2]^2\sigma^B_{\rm FoG}[z]^2/2\right)^{-2}, \tag{C15}$$

where $\sigma^B_{\rm FoG}$ is a different parameter than $\sigma^P_{\rm FoG}$ in equation (23). In this paper, we treat $\sigma^P_{\rm FoG}$ and $\sigma^B_{\rm FoG}$ as independent parameters, although they may be weakly correlated.

As it is done for the power spectrum, we can express the redshift-space bispectrum in spherical harmonics,

$$B^{(s)}(\boldsymbol{k}_1,\boldsymbol{k}_2) = \sum_{\ell=0}^{\infty}\sum_{m=-\ell}^{\ell} B_m^\ell(k_1,k_2,k_3)Y_\ell^m(\mu_1,\mu_2). \tag{C16}$$

The original signal of $B^{(s)}$ is now spread along the different multipoles $B_{\ell,m}$. However, most of the signal is contained in those multipoles with lower values of ℓ and m. As for the power spectrum only the first multipole with $\ell = 0$ and $m = 0$ (monopole) can be extracted using the FKP-estimator, since $Y_0^0 = 1$. The bispectrum monopole can be written as a function of the bispectrum in redshift space as[7]

$$B_g^{(0)}(k_1,k_2,k_3) = \int \mathrm{d}\mu_1 d\mu_2 B_g^{(s)}(\boldsymbol{k}_1,\boldsymbol{k}_2) \equiv \int_{-1}^{+1}\mathrm{d}\mu_1\int_0^{2\pi}\mathrm{d}\varphi\; B_g^{(s)}(\boldsymbol{k}_1,\boldsymbol{k}_2), \tag{C17}$$

where φ has been defined to be $\mu_2 \equiv \mu_1 x_{12} - \sqrt{1-\mu_1^2}\sqrt{1-x_{12}^2}\cos\varphi$, where $x_{12} \equiv (9_1 \cdot F_2)/(k_1k_2)$.

Integrating over the line of sight of the two vectors we obtain an expression for the monopole,

$$B_g^{(0)}(\boldsymbol{k}_1,\boldsymbol{k}_2) = \int \mathrm{d}\mu_1 d\mu_2 B_g^{(s)}(\boldsymbol{k}_1,\boldsymbol{k}_2). \tag{C18}$$

An expression for $B_g^{(0)}$ can be analytically written only when $D^B_{\rm FoG} = 1$. This is not the case in general (only when we describe halo without substructure). However, even in this simplified case, having an analytical expression helps understanding the behaviour of the different terms,

$$\begin{aligned} B_g^{(0)}(\boldsymbol{k}_1,\boldsymbol{k}_2) = {} & P(k_1)P(k_2)b_1^4\left\{\frac{1}{b_1}\mathcal{F}_2(k_1,k_2,\cos\theta_{12})\mathcal{D}^{(0)}_{\rm SQ1} + \frac{1}{b_1}\mathcal{G}_2(k_1,k_2,\cos\theta_{12})\mathcal{D}^{(0)}_{\rm SQ2}\right. \\ & \left. + \left[\frac{b_2}{b_1^2} + \frac{b_{s^2}}{b_1^2}S_2(\boldsymbol{k}_1,\boldsymbol{k}_2)\right]\mathcal{D}^{(0)}_{\rm NLB} + \mathcal{D}^{(0)}_{\rm FoG}\right\} + \text{cyc.}, \end{aligned} \tag{C19}$$

where $\mathcal{D}^{(0)}_{\rm SQ1}$ and $\mathcal{D}^{(0)}_{\rm SQ2}$ are the first- and second-order contribution for the large-scale squashing (Kaiser effect or pancakes-of-God), $\mathcal{D}^{(0)}_{\rm NLB}$ is the non-linear bias contribution and $\mathcal{D}^{(0)}_{\rm FoG}$ is the damping effect due to the velocity dispersion (linear part of FoG). The $\mathcal{F}$ and $\mathcal{G}$ terms can either be SPT or effective. All these terms depends on x_{ij}, y_{ij} and $\beta \equiv f/b_1$: $\mathcal{D}_l^{(0)}(x_{ij},\,y_{ij};\beta)$,

$$\mathcal{D}^{(0)}_{\rm SQ1} = \frac{2(15+10\beta+\beta^2+2\beta^2x_{12}^2)}{15}, \tag{C20}$$

$$\begin{aligned} \mathcal{D}^{(0)}_{\rm SQ2} = {} & 2\beta\left(35y_{12}^2 + 28\beta y_{12}^2 + 3\beta^2y_{12}^2 + 35 + 28\beta\right. \\ & + 3\beta^2 + 70y_{12}x_{12} + 84\beta y_{12}x_{12} + 18\beta^2y_{12}x_{12} + 14\beta y_{12}^2x_{12}^2 + 12\beta^2y_{12}^2x_{12}^2 \\ & \left. + +14\beta x_{12}^2 + 12\beta^2x_{12}^2 + 12\beta^2y_{12}x_{12}^3\right)/[105(1+y_{12}^2+2x_{12}y_{12})], \end{aligned} \tag{C21}$$

[7] Since for $\ell = 0$ there is only one possible m, we ignore this last parameter in the notation of the bispectrum monopole: $B^{(0)}_{(0)\,g} \equiv B_g^{(0)}$

$$\mathcal{D}^{(0)}_{\rm NLB} = \frac{(15+10\beta+\beta^2+2\beta^2x_{12}^2)}{15}, \tag{C22}$$

$$\begin{aligned}\mathcal{D}^{(0)}_{\rm FoG} = \beta\,\big(&210+210\beta+54\beta^2+6\beta^3+105y_{12}x+189\beta y_{12}x_{12}\\&+99\beta^2y_{12}x_{12}+15\beta^3y_{12}x_{12}+105y_{12}^{-1}x_{12}+189\beta y_{12}^{-1}x+99\beta^2y_{12}^{-1}x_{12}+15\beta^3y_{12}^{-1}x_{12}\\&+168\beta x_{12}^2+216\beta^2x_{12}^2+48\beta^3x_{12}^2+36\beta^2y_{12}x_{12}^3+20\beta^3y_{12}^{-1}x_{12}^3\\&+36\beta^2y_{12}^{-1}x_{12}^3+20\beta^3y_{12}x_{12}^3+16\beta^3x_{12}^4\big)/315,\end{aligned} \tag{C23}$$

where $\beta \equiv f/b_1$, $x_{ij} \equiv \boldsymbol{k}_i\cdot\boldsymbol{k}_j/(k_ik_j)$, $y_{ij}\equiv k_i/k_j$.

APPENDIX D: EXPLICIT EXPRESSIONS FOR EFFECTIVE KERNELS

The performance of the tree-level form of the matter bispectrum can be improved substantially at small scales by substituting the $\mathcal{F}_2^{\rm SPT}$ and $\mathcal{G}_2^{\rm SPT}$ kernels by effective analogues with free fitting parameters that can be calibrated using N-body simulations (Gil-Marín et al. 2012a, 2014b),

$$\mathcal{F}_2^{\rm eff}(\boldsymbol{k}_i,\boldsymbol{k}_j) = \frac{5}{7}a(n_i,k_i;\boldsymbol{a}^F)a(n_j,k_j;\boldsymbol{a}^F)+\frac{1}{2}\cos(\theta_{ij})\left(\frac{k_i}{k_j}+\frac{k_j}{k_i}\right)b(n_i,k_i;\boldsymbol{a}^F)b(n_j,k_j;\boldsymbol{a}^F) \tag{D1}$$

$$+\frac{2}{7}\cos^2(\theta_{ij})c(n_i,k_i;\boldsymbol{a}^F)c(n_j,k_j;\boldsymbol{a}^F), \tag{D2}$$

$$\mathcal{G}_2^{\rm eff}(\boldsymbol{k}_i,\boldsymbol{k}_j) = \frac{3}{7}a(n_i,k_i;\boldsymbol{a}^G)a(n_j,k_j;\boldsymbol{a}^G)+\frac{1}{2}\cos(\theta_{ij})\left(\frac{k_i}{k_j}+\frac{k_j}{k_i}\right)b(n_i,k_i;\boldsymbol{a}^G)b(n_j,k_j;\boldsymbol{a}^G) \tag{D3}$$

$$+\frac{4}{7}\cos^2(\theta_{ij})c(n_i,k_i;\boldsymbol{a}^G)c(n_j,k_j;\boldsymbol{a}^G), \tag{D4}$$

with the functions a, b and c defined as

$$\begin{aligned}a(n,k,\boldsymbol{a}) &= \frac{1+\sigma_8^{a_6}(z)[0.7Q_3(n)]^{1/2}(qa_1)^{n+a_2}}{1+(qa_1)^{n+a_2}},\\ b(n,k,\boldsymbol{a}) &= \frac{1+0.2a_3(n+3)(qa_7)^{n+3+a_8}}{1+(qa_7)^{n+3.5+a_8}},\\ c(n,k,\boldsymbol{a}) &= \frac{1+4.5a_4/[1.5+(n+3)^4](qa_5)^{n+3+a_9}}{1+(qa_5)^{n+3.5+a_9}},\end{aligned} \tag{D5}$$

where $q\equiv k/k_{\rm nl}$ with $k_{\rm nl}(z)$ a characteristic scale defined as

$$\frac{k_{\rm nl}(z)^3P^{\rm lin}(k_{\rm nl},z)}{2\pi^2}\equiv 1; \tag{D6}$$

n is the slope of the smoothed linear power spectrum,

$$n(k)\equiv\frac{{\rm d}\log P^{\rm lin}_{\rm nw}(k)}{{\rm d}\log k}, \tag{D7}$$

$Q_3(n)$ is defined as

$$Q_3(n)\equiv\frac{4-2^n}{1+2^{n+1}} \tag{D8}$$

and $\boldsymbol{a}=\{a_1,\ldots,a_9\}$, is a set of nine free parameters to be fit by comparison to N-body simulations. For the $\mathcal{F}_2^{\rm eff}$ these parameters are (Gil-Marín et al. 2012a)

$$\begin{aligned}a_1^{\mathcal{F}}&=0.484 \quad a_4^{\mathcal{F}}=0.392 \quad a_7^{\mathcal{F}}=0.128\\ a_2^{\mathcal{F}}&=3.740 \quad a_5^{\mathcal{F}}=1.013 \quad a_8^{\mathcal{F}}=-0.722\\ a_3^{\mathcal{F}}&=-0.849 \quad a_6^{\mathcal{F}}=-0.575 \quad a_9^{\mathcal{F}}=-0.926\end{aligned}$$

and for the $\mathcal{G}_2^{\rm eff}$ kernel are (Gil-Marín et al. 2014b)

$$\begin{aligned}a_1^{\mathcal{G}}&=3.599 \quad a_4^{\mathcal{G}}=-3.588 \quad a_7^{\mathcal{G}}=5.022\\ a_2^{\mathcal{G}}&=-3.879 \quad a_5^{\mathcal{G}}=0.336 \quad a_8^{\mathcal{G}}=-3.104\\ a_3^{\mathcal{G}}&=0.518 \quad a_6^{\mathcal{G}}=7.431 \quad a_9^{\mathcal{G}}=-0.484.\end{aligned}$$

These new kernels have been shown to improve the behaviour of bispectrum both in real and redshift space up to scales of $k \simeq 0.2$ for a wide range of redshifts, $z \leq 1.5$.

Both $\mathcal{F}_2^{\rm eff}$ and $\mathcal{G}_2^{\rm eff}$ have a similar dependence on a, b and c functions. However, the parameters on which these functions depend, namely $\boldsymbol{a}^{\mathcal{F}}$ and $\boldsymbol{a}^{\mathcal{G}}$, are different for $\mathcal{F}$ and $\mathcal{G}$.

This paper has been typeset from a TEX/LATEX file prepared by the author.